

Summer 7-2017

Numerical Study of Mixing of a Supercritical Jet in a Supercritical Environment

Neil Sullivan
Embry-Riddle Aeronautical University

Follow this and additional works at: <https://commons.erau.edu/edt>



Part of the [Aerospace Engineering Commons](#)

Scholarly Commons Citation

Sullivan, Neil, "Numerical Study of Mixing of a Supercritical Jet in a Supercritical Environment" (2017).
Doctoral Dissertations and Master's Theses. 376.
<https://commons.erau.edu/edt/376>

This Thesis - Open Access is brought to you for free and open access by Scholarly Commons. It has been accepted for inclusion in Doctoral Dissertations and Master's Theses by an authorized administrator of Scholarly Commons. For more information, please contact commons@erau.edu.

NUMERICAL STUDY OF MIXING OF A SUPERCRITICAL JET IN A
SUPERCRITICAL ENVIRONMENT

A Thesis

Submitted to the Faculty

of

Embry-Riddle Aeronautical University

by

Neil Sullivan

In Partial Fulfillment of the

Requirements for the Degree

of

Master of Science in Aerospace Engineering

July 2017

Embry-Riddle Aeronautical University

Daytona Beach, Florida



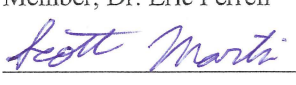

NUMERICAL STUDY OF MIXING OF A SUPERCRITICAL JET IN A
SUPERCRITICAL ENVIRONMENT

by

Neil Sullivan

A Thesis prepared under the direction of the candidate's committee chairman, Dr. Mark Ricklick, Department of Aerospace Engineering, and has been approved by the members of the thesis committee. It was submitted to the School of Graduate Studies and Research and was accepted in partial fulfillment of the requirements for the degree of Master of Science in Aerospace Engineering.

THESIS COMMITTEE


Chairman, Dr. Mark Ricklick
Member, Dr. Ebenezer Gnanamanickam
Member, Dr. Eric Perrell
Member, Dr. Scott Martin
Graduate Program Coordinator, Dr. Tasos Lyrintzis
Date
Dean of College of Engineering, Dr. Maj Mirmirani
Date
Vice Chancellor, Academic Support, Dr. Christopher Grant
Date

ACKNOWLEDGMENTS

I would like to first thank my thesis supervisor, Dr. Mark Ricklick for his guidance and patience, without which this work would not have been possible. Thanks are extended also to my thesis committee for taking the time to participate and also helping guide the work.

My new bride is an endless source of love and support. She may roll her eyes or lose interest when I talk at length or in detail about what I'm doing, but her faith in me is a large part of what keeps driving me to the finish line. Thanks Laura, and I love you.

I would not be where I am today, either as a student or a man, without the constant love, encouragement, and support of my late father. The debt owed to him could never be repaid and it leaves me only with the obligation to work hard, try my best and repeat his example of generosity and selflessness unto others. Thanks Dad, and I love you.

TABLE OF CONTENTS

LIST OF TABLES	vi
LIST OF FIGURES	vii
SYMBOLS	ix
ABBREVIATIONS	x
ABSTRACT	xi
1. Introduction	1
Turbulent Free Jet.....	2
Supercritical Fluids.....	4
Applications	7
Problem Statement	8
2. Literature Review	10
Experiments in Supercritical Jets	10
Approaches to Modeling Supercritical Jets	15
Applications of Supercritical Fluid Modeling	32
3. Model Setup	35
Code, Benchmark and Computational Grid	35
STAR-CCM+ Coupled Flow Solver	39
Reynolds-Averaged Navier-Stokes.....	41
k-Omega SST Turbulence Model	41
Large Eddy Simulation	43
NIST REFPROP Data.....	44
Boundary and Initial Conditions	44
Model settings: RANS	46
Model Settings: LES	46
Original Test Case Matrix.....	47
Challenges with LES and Lessons Learned	48
Revised Test Case Matrix	48
Grid Independence	49
4. Results and Discussion.....	54
Preliminaries: First Steps in Benchmarking	54
LES Results	61
RANS Results: Comparison with Previous Work	64
RANS Results: Comparison of Subcritical and Supercritical Results.....	76
Final Thoughts	79
5. Conclusions and Recommendations	81
Future Work.....	82
REFERENCES	84

A.	Model Convergence Data.....	93
----	-----------------------------	----

LIST OF TABLES

Table 3.1 Experiment Data (Branam, 2002).....	35
Table 3.2 2D Grid Quality	37
Table 3.3 3D Grid Quality	38
Table 3.4 Inlet Boundary Condition Parameters.....	45
Table 3.5 Physics Models Used in RANS Simulation.....	46
Table 3.6 Physics Models Included in LES Simulation	47
Table 3.7 Benchmarking Test Matrix	47
Table 3.8 Nominal Test Matrix.....	48
Table 3.9 Test Case Matrix: Supercritical Jet.....	49
Table 3.10 Test Case Matrix: Atmospheric Jet, User-Defined EoS	49
Table 3.11 Test Case Matrix: Atmospheric Jet, Ideal Gas EoS.....	49

LIST OF FIGURES

Figure 1.1 Turbulent Free Jet Streamwise-Direction Mixing Regions (Zong, 2004).....	3
Figure 1.2 Turbulent Free Jet Transverse-Direction Mixing Regions (Felouah, 2009)	4
Figure 1.3 P-T Diagram of Supercritical Region for N ₂	5
Figure 1.4 Variation in c_p with Temperature on a 3.4 MPa Isobar (NIST Chemistry WebBook).....	6
Figure 3.1 Experimental Setup (Branam, 2002)	36
Figure 3.2 Centerline Density: Unsteady RANS	50
Figure 3.3 Centerline Axial Velocity: Unsteady RANS	51
Figure 3.4 Axial Velocity Profiles: Unsteady RANS, Reference Mesh	52
Figure 3.5 Axial Velocity Profiles: Unsteady RANS, Mesh Level 2	52
Figure 3.6 Axial Velocity Profiles: Unsteady RANS, Mesh Level 3	53
Figure 4.1 Half-jet velocity contour, reference mesh	55
Figure 4.2 Centerline Density of a 1 atm jet using ideal gas EoS	55
Figure 4.3 Pressure contour of a steady-state jet	56
Figure 4.4 Density contour of a steady-state jet	56
Figure 4.5 N ₂ Density Calculation Using PR EoS Compared to NIST Data on a 3.5 MPa Isobar.....	57
Figure 4.6 N ₂ Density Calculation Using PR EoS Compared to NIST Data on a 130 K Isotherm	57
Figure 4.7 Percent Error of Density Calculation on an Isobar.....	58
Figure 4.8 Percent Error of Density Calculation on an Isotherm	58
Figure 4.9 Centerline Density of a supercritical jet using the PR EoS, constant properties	59
Figure 4.10 Centerline Density Comparison to CharLES results	60
Figure 4.11 Centerline Density Comparison to CharLES Results, User-Defined EoS	61
Figure 4.12 Nikurasde Fully Developed Turbulent Flow Velocity Profile	62
Figure 4.13 Velocity Magnitude Contour, CharLES Results (Hickey, 2013)	62
Figure 4.14 Velocity Magnitude Contour, LES Results, Current Work.....	62
Figure 4.15 Temperature Contour, CharLES Results, (Hickey, 2013).....	63
Figure 4.16 Temperature Contour, LES Results, Current Work	63
Figure 4.17 Centerline Density, LES Results, 680 ms Flowtime, Current Work.....	63
Figure 4.18 Velocity Magnitude Contour, CharLES Results, (Hickey, 2013)	64

Figure 4.19 Velocity Magnitude Contour, RANS Results, Current Work	64
Figure 4.20 Temperature Contour, CharLES Results, (Hickey 2013).....	65
Figure 4.21 Temperature Contour, RANS Results, Current Work.....	65
Figure 4.22 RANS Centerline Density Compared to CharLES Results.....	66
Figure 4.23 Centerline Density: Current Work Compared to Case 6 (3.9 MPa, 133 K, 5.4 m/s), (Branam, 2003)	67
Figure 4.24 Potential Core Penetration vs. Density Ratio (Branam, 2003).....	68
Figure 4.25 Axial Velocity Profiles, Unsteady RANS	69
Figure 4.26 Jet Half-Width Locations, Unsteady RANS.....	69
Figure 4.27 Tabular Jet Spreading Angle Data (Branam, 2003)	70
Figure 4.28 Shadowgraph Image: Case 3, 4 MPa, 4.9 m/s, 123 K Injected N ₂ Jet (Branam, 2002)	71
Figure 4.29 Density Contour (Snapshot) Unsteady RANS, Current Work	71
Figure 4.30 Streamwise Direction Turbulent Length Scales, Case 3 (Branam, 2002).....	72
Figure 4.31 Transverse Direction Turbulent Length Scales, Case 3 (Branam, 2002).....	72
Figure 4.32 Integral Length Scales at Various x/D Locations, Unsteady RANS	74
Figure 4.33 Taylor Microscales at Various x/D Locations, Unsteady RANS	74
Figure 4.34 Kolmogorov Microscales at Various x/D Locations, Unsteady RANS	75
Figure 4.35 Calculated Turbulent Length Scales.....	75
Figure 4.36 Normalized Centerline Density: Supercritical and two Subcritical Simulations, Unsteady RANS, Current Work	77
Figure 4.37 Centerline Axial Velocity: Supercritical and two Subcritical Simulations, Unsteady RANS, Current Work	78
Figure 4.38 Dynamic Viscosity Profiles at x/D = 10: Supercritical and two Subcritical Simulations, Unsteady RANS, Current Work	79
Figure 5.1 Residuals, Unsteady RANS, Supercritical	93
Figure 5.2 Monitor of Density at x/D = 10, Unsteady RANS, Supercritical.....	93
Figure 5.3 Monitor of Surface Average Density, Unsteady RANS, Supercritical	94
Figure 5.4 Residuals, Unsteady RANS, Subcritical	94
Figure 5.5 Surface Average of Density, Unsteady RANS, Subcritical	95
Figure 5.6 Monitor of Density at 10 Jet Diameters, Unsteady RANS, Subcritical	95
Figure 5.7 Residuals, LES	96
Figure 5.8 Monitor of Density at x/D = 10, LES	96
Figure 5.9 Monitor of Surface Average Density, LES	97

SYMBOLS

m	mass
u	streamwise velocity
c_p	specific heat at constant pressure [J/kg K]
ρ	density [kg/m ³]
k	thermal conductivity [W/m K]
μ	dynamic viscosity [Pa s]
h	specific enthalpy [J/kg]
s	specific entropy [J/K]
a	speed of sound [m/s]
c_v	specific heat at constant volume [J/kg K]
γ	ratio of specific heats, c_p/c_v
M	Mach number, eg. u/a

ABBREVIATIONS

SC	Supercritical
NIST	National Institute of Standards and Technology
RANS	Reynolds-Averaged Navier-Stokes
LES	Large Eddy Simulation
DLR	Deutsches Zentrum für Luft und Raumfahrt (German Aerospace Center)
SGS	Sub-Grid Scale
EoS	Equation of State
ENO	Essentially Non-Oscillatory
MUSCL	Monotonic Upstream-Centered Scheme for Conservation Laws
SST	Menter's Shear Stress Transport Model

ABSTRACT

Sullivan, Neil MSAE, Embry-Riddle Aeronautical University, July 2017. Mixing of a Supercritical Jet in a Supercritical Environment.

A numerical simulation campaign is conducted to better elucidate flow physics and modeling requirements of a supercritical (SC) nitrogen jet injected into a tank of quiescent SC nitrogen. The goals of this work are twofold: to inform the design of injectors and combustion chambers for use in the direct-fired supercritical CO₂ (s-CO₂) power generation cycle and cryogenic liquid propellant rockets, and to investigate the extent to which meaningful flow characterization can be achieved with computationally expedient methods, using commercial software. Reynolds-Averaged Navier-Stokes (RANS) and Large Eddy Simulation (LES) approaches are used in STAR-CCM+ versions 10.06.010 and 12.02.011. Jet disintegration is evaluated with velocity, density and temperature profiles, potential core penetration and identification of turbulent length scales. These data are compared with experimental data and evaluated against other modeling approaches. Mixing behavior is expected to mimic that of a single-phase jet, and be diffusion-driven, as there will be no droplet formation in the supercritical phase. Challenges are encountered in high computational requirements inherent to unsteady LES. Challenges are also encountered in simulation stability and convergence given large flow gradients near jet exit, large fluid property gradients near the critical point, and the small length scale of energetic flow features unique to this high-pressure thermodynamic regime. Simulation results over-predict core penetration compared to experiment and previous numerical efforts and show an overall slower transition to ambient conditions. It is shown however that commercial code can correctly synthesize the overall flow physics and trends of the

single-phase gas jet behavior expected in purely supercritical turbulent mixing flow.

1. Introduction

Effort in the study of supercritical fluid phenomena, specifically turbulent mixing and heat transfer, has become significant in the last 20 years. This owes in part to the evolution of certain thermo-fluid systems, as operating temperatures and pressures increase in the continuing quest for efficiency and performance. Important examples include compression-ignition (diesel) engines, liquid-propellant rocket engines and new-generation heat exchangers (Roy, 2010). This increase in research can also be attributed to the increase in worldwide computer power and advances in parallel computing, with the world's most powerful supercomputers now exceeding 100 PetaFlops (peak performance 125 PFlops, or 125×10^{15} floating-point operations/sec) (Fu, 2016). Numerical methods have also matured in this time to take greater advantage of new computing power (Zong, 2004; Barata, 2003; Cutrone, 2006; Kim, 2011). Large Eddy Simulation (LES) and even Direct Numerical Simulation (DNS) can be brought to bear on increasingly complex flows and flow phenomena, and Reynolds-Averaged Navier-Stokes simulations can be run by non-specialists on less expensive computing assets as an integral part of the product design cycle.

The present work was inspired by an applied design problem in an emerging, highly-efficient power generation technology. Sandia National Laboratories (SNL) is currently working on a 10 MW (electric) "s-CO₂ Brayton Power Conversion System" as a system identification prototype in which the working fluid is supercritical carbon dioxide in a Brayton thermodynamic cycle. It is intended to replace steam Rankine cycles in many applications and offers advantages in capital cost and thermal efficiency over the older cycle (Lewis, 2012). The turbulent mixing of a supercritical jet is more relevant to an

undertaking at Southwest Research Institute (SWRI), where a novel cycle is being developed in which combustion occurs inside the supercritical CO₂ medium (Brum 2014). The design of injectors and combustors for such a plant is the motivation for this paper. A thorough understanding of the flow physics and modeling requirements of a supercritical jet in a supercritical environment is first necessary, and this is the focus of current work; future work will involve co-axial fuel/oxidizer injectors and supercritical cross-flow domains. High-fidelity real-gas combustion modeling tailored to supercritical flows is also important in reducing development cost and design cycles. The following pages serve to introduce the reader to the geometry, thermodynamic regime and mixing phenomena of concern to current work.

Turbulent Free Jet

The round free jet is a canonical flow whose study dates to the beginning of fluid mechanics as a field of study. 3rd Baron Rayleigh made contributions to turbulent jet breakup in the late 19th century (Strutt, 1879). A jet is a flow ejected from a nozzle or orifice at a high speed relative to fluid surrounding it. Round jets and plane jets are well-studied viscous flow phenomena. A turbulent jet is defined as a jet that is considered turbulent (depending on normalization of the Reynolds number) at jet exit, and becomes more turbulent as flow evolves downstream. Figure 1 shows a typical turbulent free jet, which traditionally has three streamwise regions.

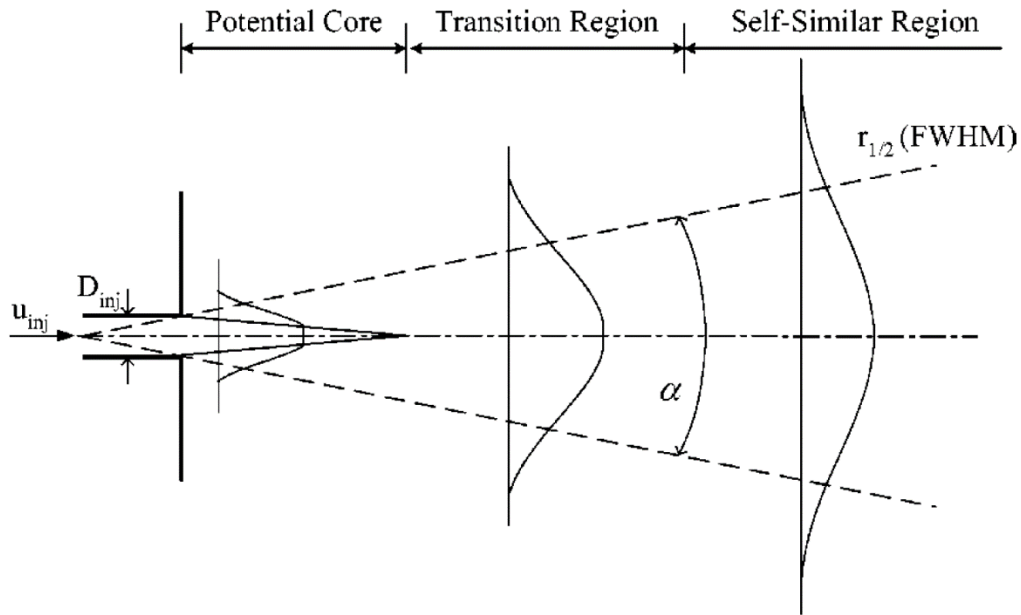


Figure 1.1 Turbulent Free Jet Streamwise-Direction Mixing Regions (Zong, 2004)

The region immediately after jet exit is relatively intact, not having begun the process of disintegration or atomization into surrounding flow. It contains the potential core, a relatively coherent region of high density that usually includes only injected fluid, as this is too early in the jet for significant entrainment to occur. Downstream of this is a transition region where instability and diffusion begin to break up the jet. Injected fluid mixes with the surrounding fluid and there is an exchange of momentum. Transverse velocity profiles, as seen above, begin to flatten as the jet spreads and energy is shared. Various mixing mechanisms can take place in this region including Plateau-Rayleigh instability (Strutt, 1879), (or Kelvin-Helmholtz instability (Roy, 2010) in the case of a laminar jet), atomization and molecular diffusion. The jet becomes relatively diffuse beyond this region and beyond a certain point is described as self-similar. Here, the non-dimensionalized streamwise velocity profiles no longer change shape in the streamwise

direction, and the life of the jet is in a meaningful sense over. Figure 1.2 indicates jet flow behavior in the transverse direction.

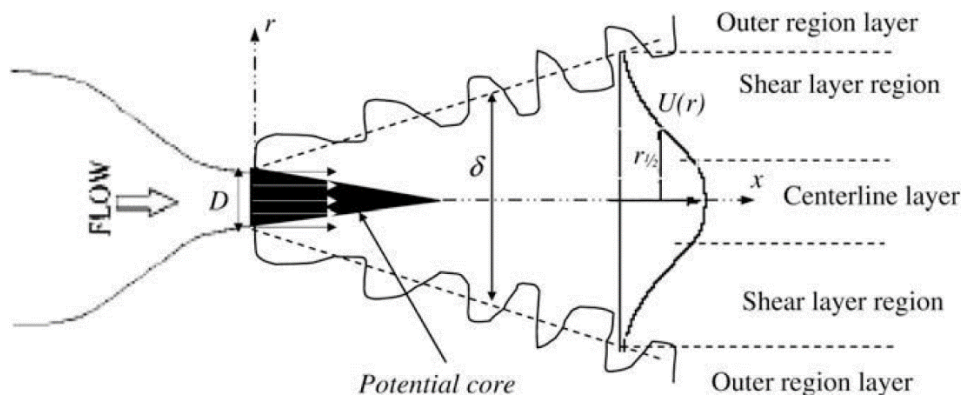


Figure 1.2 Turbulent Free Jet Transverse-Direction Mixing Regions (Felouah, 2009)

Flow in the shear layer and changes in fluid properties in this region are of particular interest to present work, as the flow features in this area have the greatest impact on jet disintegration and mixing.

Supercritical Fluids

A supercritical fluid is defined as a fluid at a temperature and pressure above its critical point. At this point, intermolecular forces become less dominant compared to the liquid phase, the densities of liquid and gas phases of the fluid are equal, and the two phases merge (Yang, 2000). Because there is no discrete phase change, there is no latent enthalpy above the critical point. Additionally, there is no interface between phases, no surface tension, and thus no droplet formation or spray behavior in turbulent jets. Figure 1.3 illustrates the thermodynamic location of this condition. The red star indicates ambient chamber conditions for current work (298 K, 4.0 MPa).

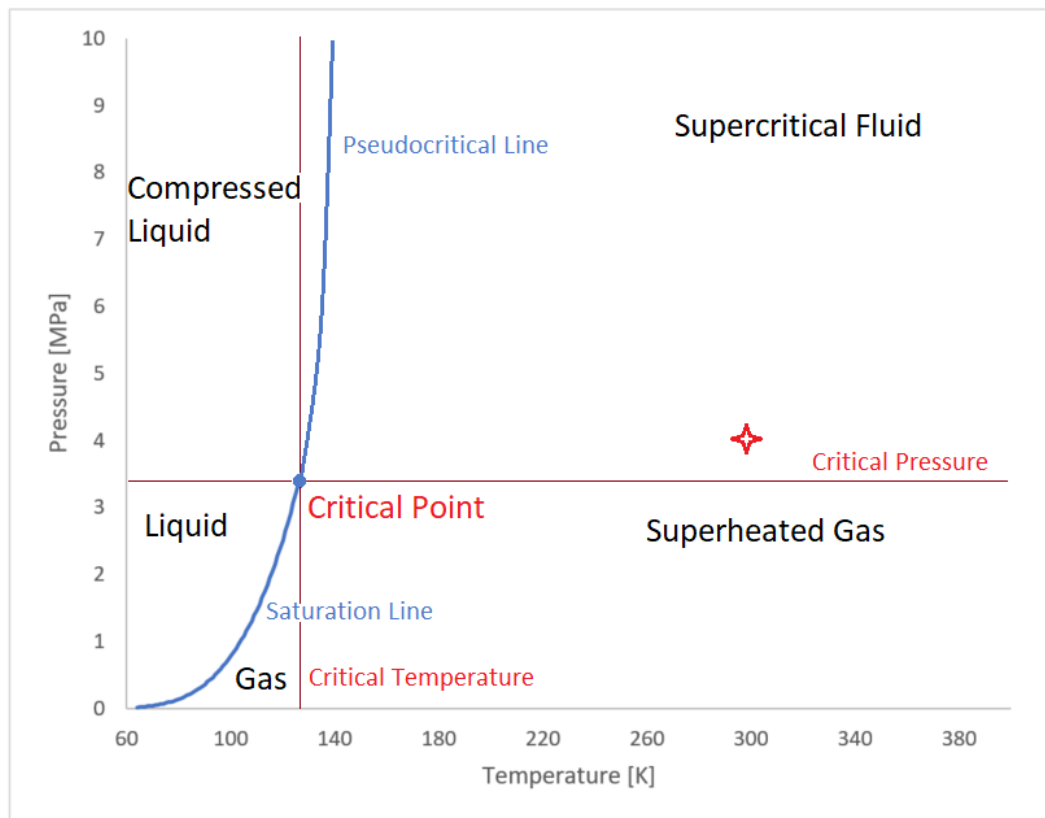


Figure 1.3 P-T Diagram of Supercritical Region for N₂

Because these temperatures and pressures do not exist at Earth's surface, the physics of supercritical fluids is not intuitive. SC fluids have liquid-like densities, gas-like diffusivities, and a litany of other thermodynamic and transport properties become weighted averages between corresponding saturated liquids and superheated gases (Bellan, 2000). The critical point is defined as a thermodynamic singularity. Here, latent enthalpy and surface tension approach zero, but specific heat (c_p), thermal conductivity (k), and isentropic compressibility (Z) tend to infinity. The pseudocritical line can be interpreted as an extension of the saturation line beyond the critical point. While there is no discrete phase change in the SC region, the pseudocritical line divides where the fluid will assume more liquid-like and more gas-like properties. For a given pressure, it is located at a temperature

where the fluid has maximum c_p , and this maximum decays with distance from the critical point. Thermodynamic and transport properties can vary wildly near the critical point and in the transcritical regions around the critical temperature and pressure. Figure 1.4 displays the significant variation in constant pressure specific heat near the critical point.

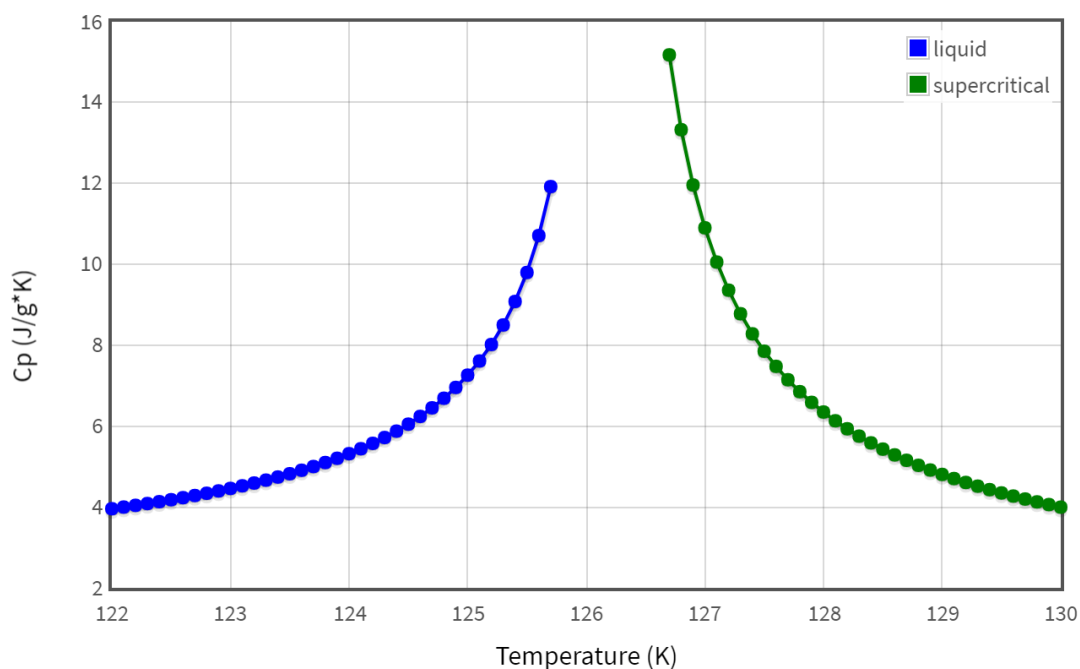


Figure 1.4 Variation in c_p with Temperature on a 3.4 MPa Isobar (NIST Chemistry WebBook)

This and other fluid properties can vary by orders of magnitude in this region. This behavior continues on the pseudocritical line, and while values no longer become arbitrarily large, there is a pronounced peak. This phenomenon is called “enhancement” and has a profound effect on the energy transport of SC fluids (Kim, 2011). These large property gradients are a major source of numerical instability (Bellan, 2000). In current work, the entire experiment and computational domain are at supercritical conditions. The ambient fluid is at a thermodynamic state inside the supercritical region indicated by a red star in Figure 1.3, and the injected jet condition is at a location essentially on top of the

pseudocritical line at approximately 40 MPa. The injected jet in this case is therefore subject to significant heat transfer enhancement, and this has a large impact on flow development, as described in later chapters.

Applications

While some properties of SC fluids create difficulties in experiment and modeling, fluids at this condition are integral to some thermo-fluid systems, and these same properties can make them advantageous. Sandia National Laboratories (SNL) propose using supercritical CO₂ (s-CO₂) in a Brayton cycle as a highly-efficient means of cooling nuclear reactors and as a power generation method for many sources (Lewis, 2012). This could reduce capital cost as compared to a steam Rankine cycle and achieve much higher thermal efficiency. Work at SWRI is ongoing on a s-CO₂ power generation cycle where combustion occurs inside the supercritical fluid (Brun, 2014). It is referred to as a direct-fire s-CO₂ power cycle, and presents many challenges, not the least of which is improving modeling of turbulent mixing and combustion in a supercritical fluid. As liquid-propellant rocket engines operate at ever-higher chamber pressures, it is often now the case that a cryogenic fuel is injected into conditions above the critical point for that fluid. A better understanding of the fuel-oxidizer mixing mechanisms at these pressures and temperatures is critical to improving rocket engine design cycle, which has heretofore relied too heavily on the test stand and trial and error experiments. This work could also contribute to mitigating combustion instability due to the coupling of flame-acoustics interaction, chemical kinetics and real fluid effects (Kim, 2011).

Problem Statement

With the eventual goal of informing the design of injectors and combustion chambers for the direct-fired s-CO₂ power cycle, the author seeks to identify numerical modeling requirements capturing all salient flow physics to the injection and turbulent mixing of a supercritical jet in a supercritical quiescent flow. This work also applies to improving injectors in liquid propellant rocket engines (Kim, 2011). Results will focus on jet breakup, potential core penetration and instabilities while attempting to match flow trends captured in higher-fidelity models. Supercritical results from current work are also compared to simulated jet behavior at subcritical conditions using the same code to highlight key differences and modeling challenges.

While high-fidelity and accurate simulation tools are essential in both first-principles research and product development, there is simultaneously value in low-cost methods giving representative or even qualitative results. Use of commercially available software wherever possible can simplify workflow while reducing a very steep learning curve for design engineers whose expertise in and experience with computational fluid dynamics may vary. A commercial CFD/Heat Transfer code STAR-CCM+ is used in conjunction with real-gas properties extracted from the NIST REFPROP library to evaluate the capability of the code and compare it to both experimental data and numerical results from sophisticated RANS and LES codes from literature, specifically tuned for simulation of trans- and supercritical fluids.

RANS simulations are expected to obscure some finer flow features in the shear layer due to a smearing effect from both Reynolds-averaging and the isotropy assumption inherent to the eddy-viscosity turbulence model. LES results are expected to provide much

flow detail missing in corresponding RANS results, however at significantly increased computational cost. To test this hypothesis, the following objectives are defined:

1. Compare fluid property modeling approaches for accuracy and cost.
2. Compare modeling approaches (steady RANS, unsteady RANS and LES) for accuracy and cost.
3. Identify shortcomings in lower-fidelity models.

2. Literature Review

A study of the fluid mechanics literature surrounding jets of supercritical fluids sheds light on an interesting dichotomy. One can apparently take such a canonical flow as the free round jet, with all its well-studied properties and behavior, and by the mere application of a few atmospheres of pressure render it scientifically obscure, intuitively specious, difficult to measure and laborious to simulate. Although crucial to the continued development of many high-technology applications, the understanding of turbulent mixing in near- and supercritical free jets is still in an early phase. The following comprises a well-rounded survey of experimental and numerical efforts to better understand the physics and behavior of these jets over the last 20 years.

Experiments in Supercritical Jets

Much effort has been undertaken in the last 20 years to study the flow physics of high-pressure jets. Branam and Mayer in a 2002 paper focus on identifying average length scales of turbulent flow features of the core flows in co-axial rocket engine injectors. A series of trans- and supercritical jets of cryogenic nitrogen were injected into a quiescent tank of room-temperature supercritical nitrogen. Fully turbulent pipe flow is described at jet exit, with Reynolds numbers ranging from 34,000 to 180,000, based on jet exit velocity and injector diameter. Jet exit diameter was 2.2 mm and the tank was of sufficient size that wall effects are neglected in the analysis and the outlet is deemed sufficiently downstream that it is considered decoupled from the flow field being considered. Walls were heated to permit a continuous adiabatic wall condition (Branam, 2002). This experimental apparatus is described in detail because this and other papers use similar or identical setups and/or data for other studies and to validate models. The shadowgraph technique was used here

with a digital camera on the optically-accessible container, after which an algorithm was used on individual greyscale pixels to obtain average length scale measurements. Turbulent eddies in the mixing layer are the principal transport mechanisms for mass and energy transfer, and previous and current work confirm their contribution (Branam, 2002). One of the most influential parameters on flow development in the jet is the ratio of injected jet velocity to surrounding fluid velocity, or, in the case of a quiescent environment, ratio of the density of fluid at jet exit to surrounding fluid density (Branam, 2002, Roy, 2010). Experimental data were compared with commercial code using k-epsilon turbulence closure and using real-gas properties. Comparison was then made to the integral length scale, Taylor microscale, and Kolmogorov microscale. These length scales are described in equations 1-3 (Branam, 2002).

$$L_{int} = \frac{k^{\frac{3}{2}}}{\varepsilon} \quad (1)$$

$$L_{Tay} = \left(\frac{15\nu\tilde{u}^2}{\varepsilon} \right)^{\frac{1}{2}}, \quad \tilde{u} = \left(\frac{u^2 + v^2 + w^2}{3} \right)^{\frac{1}{2}} \quad (2)$$

$$L_{Kol} = \left(\frac{\nu^3}{\varepsilon} \right)^{\frac{1}{4}} \quad (3)$$

Where k is turbulent kinetic energy, ε is the turbulent dissipation rate, ν is the kinematic viscosity, and u , v , and w are generalized basis vector velocities.

In general, observed turbulent flow features, when geometrically averaged, exhibited length scales with strong correspondence to calculated Taylor microscales, which are average length scales where the largest amount of energy is dissipated. These tend to be an order of magnitude larger than Kolmogorov microscales, and an order of magnitude

smaller than integral length scales (Branam, 2002).

Further work was done by Branam and Mayer to characterize the high-density core flow of oxidizer in a co-axial injector, using cryogenic nitrogen to simulate liquid oxygen. Density, length scales and jet spreading angles are compared for injected nitrogen jets at several temperatures and injection velocities to evaluate mass mixing and jet dissipation. Change in temperature of the injected fluid was found to have the largest impact on jet behavior, as this changes the density ratio between fluid at jet exit and the surroundings (Branam, 2003). Also of interest in characterizing the jet flow is the axial distance at which self-similarity is achieved, which is the region where flow properties can be considered functions of one variable only (axial distance). It is here noted that self-similarity can exist for one flow property, such as axial velocity, but not for others, such as density or turbulent kinetic energy (Branam, 2003). In this paper, the self-similar region shall be defined as the area where axial velocity has become sufficiently diffuse to be considered a function of axial distance only. Branam and Mayer here compare the same experimental data as before against a Favre-Averaged Navier-Stokes (FANS) commercial code with k-epsilon turbulence closure called CFD-ACE. Real gas models are invoked here, namely Lee-Kesler, Chung et al and a modified version of Benedict-Webb-Rubin equation of state. This code can resolve weak compressibility effects by virtue of real gas relationships for density, specific heat, viscosity and thermal conductivity which are derived from the above EoS (Branam, 2003). The result is an incompressible, yet variable-density code, suitable for low Mach numbers, and incorporating variable isentropic compressibility. Calculated Grashof, Froude and Reynolds numbers indicate that inertial forces are significant while body forces and buoyancy, as well as viscous forces can be neglected (Branam, 2003). This supports

the contention that supercritical jet mixing is primarily diffusion-driven, and will be similar qualitatively to single-phase gas-gas mixing. Several metrics including radial property profiles, centerline density, potential core length and jet divergence angle are compared to present work.

Polikhov, in a 2007 paper, presents an experiment using planar laser induced fluorescence (PLIF) to generate a section through the jet center, in hopes of eliminating some shortcomings inherent to shadowgraphy, used to produce most data in previous work on supercritical jet mixing (Polikhov, 2007). Principal issues with the shadowgraph technique are two-fold. It is an integrative observation technique, in that light entering the camera must pass through the entire jet, such that the measurement taken is an average. Secondly, the technique measures density gradient, and not an absolute density. This means low-density but highly turbulent regions can saturate the image. These regions of low-density mixed fluid can suggest highly-diffuse gas-gas like mixing, while potentially obscuring a high-density core at the jet center (Polikhov, 2007). A cryogenic fluid, FK-5-1-12, is injected into a chamber filled with nitrogen at varying conditions: subcritical, transcritical and supercritical, with respect to the injected fluid. A linear stability analysis is performed to develop a distortion relation for the viscous jet in inviscid gaseous surroundings. This is successful for the subcritical case, but fails as temperature and pressure are raised in the container. Large density gradient between injected and surrounding fluid is found to have a damping effect on turbulence, and decreases the mixing rate. This leads to a longer potential core length.

Studies of free jets of course date back to the origins of fluid mechanics, with notable efforts by Rayleigh and Prandtl when the field of turbulent mixing was in its

infancy (Roy, 2010). Many semi-empirical expressions exist for subcritical jet breakup length and droplet size distribution for two-phase flows, but these types of qualifications are lacking in the literature for trans- and supercritical flows (Roy, 2010). The author notes that Kelvin-Helmholtz instabilities (KHI) can describe the breakup of an initially laminar jet, but this theory does not apply to the breakup and atomization of an initially turbulent jet (Roy, 2010).

Roy and Segal employ a novel method of fluorescing Perfluoroketone, a 3M product, to detect detailed structures in a jet center plane, and study flow-field densities. This jet flow is important to drive design of future liquid-propellant rocket engines as well as pressure-ignition reciprocating engines, where liquid fuels are injected into supercritical conditions relative to the fuel. Density gradient profiles were generated and potential core lengths measured, which were then compared to previous flow visualization results. Three major cases were studied: a subcritical jet into a subcritical environment, a subcritical jet into a supercritical environment (relative to the injected fluid), and a supercritical jet injected into a supercritical environment. Chamber/injected fluid density ratios ranged from 0.01 to 0.04. In the trans- and supercritical regime, this pressure ratio is found to be a strong driver of flow development and potential core length, whereas this strong correspondence is not encountered in subcritical single-phase gas jets. Core lengths were evaluated by algorithms using the extracted optical data, and an eigenvalue approach was taken to determine the location of maximum density gradients. The literature does not contain a unique, precise definition of the potential core of supercritical jets, and here it is taken as an intact region of higher density than downstream areas. In the supercritical jet/supercritical chamber case, potential core length was shorter than in the either

subcritical case, and this is attributed to the aforementioned density ratio. As temperature and pressure in the chamber increase, jet mixing qualitatively approaches single-phase gas-gas, as the density ratio will decrease, and so will the stabilizing effect of a high radial density gradient. Shear layer instabilities were low, smoothing the jet at the supercritical condition, and this trend continued as density gradient values decreased downstream.

Mixing phenomena when injected fuel is supercritical but surrounding environment is subcritical relative to the fuel are less covered in the literature but are treated from the perspective of supersonic combustor (scramjet) design by Wu in a 1999 paper. Wu studies under-expanded supersonic supercritical ethylene jets entering a superheated combustion chamber, measuring the location and size of Mach discs (shock diamonds) and jet expansion angle. Schlieren photography and Raman scattering techniques are used in this experiment. Fuel is intended to act as a heat sink to modulate fuselage temperatures at hypersonic vehicle velocities, and may go beyond its critical point before it is injected into the combustor (Wu, 1999). Mixing was determined by fuel mole fraction and temperature distributions. As the injected jet initial condition approached the critical point, ethylene centerline mole fraction increased, as did the jet width at a location of stoichiometric mixture. Temperature deficit in the jet was also more pronounced at near-critical conditions. This suggests turbulent mixing was inhibited in the trans-critical regime. Mach disk location was unchanged in a supercritical jet, but expansion angle increased as injected jet temperature reached the critical temperature (Wu, 1999).

Approaches to Modeling Supercritical Jets

Zong identifies several phenomena compounding existing modeling difficulties surrounding high-pressure flow in his 2004 paper. Compressibility effects (pressure-

induced volumetric changes) and variable inertia effects (resulting from heat addition or variable composition in chemically reacting flows) can lead to instability. Additionally, as density increases, so does Reynolds number (Re increases approximately linearly with pressure) which tends to shrink Taylor and Kolmogorov microscales (Zong, 2004). This in turn requires mesh refinement to capture flow features carrying a large portion of the energy spectrum.

Zong conducts a LES study on subcritical liquid nitrogen injection into a supercritical environment using full conservation laws and real-fluid thermodynamics and transport phenomena. A modified form of the Soave-Redlick-Kwong (SRK) cubic equation of state (EoS) is used. The real-gas properties are calculated with departure functions, which constitute the sum of an ideal gas contribution with a real-gas effect near the critical point. The modified SRK and example internal energy departure function are presented as equations 4 and 5.

$$P = \frac{\rho R_u T}{W - b\rho} - \frac{a\alpha}{W} \frac{\rho^2}{(W + b\rho)} \quad (4)$$

$$e(T, \rho) = e_0(T) + \int_{\rho_0}^{\rho} \left[\frac{P}{\rho^2} - \frac{T}{\rho^2} \left(\frac{\partial P}{\partial T} \right)_{\rho} \right] \partial \rho \quad (5)$$

Where P is pressure; ρ is density; R_u is the universal gas constant; T is temperature; W is a model parameter arising from SRK modification; a and b are other model parameters; and α is a parameter containing an approximated critical compressibility factor and the acentric factor, a molecular property.

A preconditioning scheme is employed here to offset the stiff matrix problem inherent to modeling supercritical fluids (Zong, 2004; Weiss, 1995). This code's solver is 4th-order centered in space and 2nd-order backward-difference in time, with a 3rd-order

Runge-Kutta scheme used in the pseudo-time preconditioning inner loop. The domain is a modest 225x90 point structured grid, with a fully-developed turbulent pipe flow inlet. Zong states that a single-phase jet shear layer has KH instabilities (for a certain Reynolds number range) and vortex rolling, pairing, and breakup. A cryogenic supercritical jet has these features and adds additional mechanisms due to baroclinic torque (a moment resulting from misalignment of a density gradient and a pressure gradient) and the volumetric changes described above. Zong's contention that a strong pressure gradient at the injector has a stabilizing effect on flow development is in keeping with the literature. The spatial growth rate of surface instability waves increases with increasing ambient pressure, or decreasing pressure ratios (which couple to density ratios). An increase in ambient pressure also leads to an earlier transition to self-similarity (Zong, 2004). Characteristic times did not change at supercritical conditions. Drastic changes in jet surface phenomena are noted across the critical pressure, and above the critical point, the jet surface topology mirrors a submerged gaseous jet, with spatial growth rate mimicking an incompressible but variable-density gas jet. At high pressure ratios, high density gradient regions develop around the jet surface due to intensive property variations. This acts as a solid wall which amplifies axial flow oscillations but damps radial oscillations. In this way instability in the shear layer is reduced. This damping effect decreases with decreasing pressure ratio, causing the jet to expand more rapidly at higher ambient pressure.

In a 2000 critical review, Bellan focuses on differentiating subcritical and supercritical flow turbulent mixing behavior and establishes a more accurate generalized nomenclature appropriate for all thermodynamic states. She characterizes the SC state by the "impossibility of a two-phase region" (Bellan, 2000). The high solubility of SC fluids

becomes important to mixing, both with other supercritical fluids and other solutes, as does the heat of solvation. These properties will vary near the critical point given their sensitivity to density and in turn the sensitivity of density to temperature and pressure. Heat of solvation becomes an important thermodynamic quantity indicative of fluid interpenetration (Bellan, 2000). Complexity arises in the mixing of several near-critical or SC fluids, as the critical locus, the averaged critical point for the mixture based on participating species' mole fractions and thermodynamic state, is not straightforward. It can be non-monotonic and convoluted depending on mixture species, which is an additional modeling concern as well as a concern during experiment. As species concentrations evolve downstream, either by diffusion or chemistry, SC regions may become subcritical and vice-versa (Bellan, 2000). It is difficult, except in a broad qualitative sense, to predetermine this mixture behavior.

It has been reasonably established in literature that spreading angle is affected by chamber/jet density ratio, and the resulting change in fluid entrainment will impact shear layer evolution. Atomization theories based on Rayleigh-Taylor instabilities (RTI) do not apply in the SC regime as there is no surface tension. Fluid mixing is instead due to high turbulence and is molecular diffusion-driven (Bellan, 2000). In a subcritical two-phase flow, waves form at the surface of the jet (KHI or other instability, depending on Reynolds number) due to the relative velocity of liquid jet and gas surroundings. The liquid sheet breaks up and atomizes. However, as ambient conditions approach supercritical relative to the jet fluid, optical data show “wispy threads” of fluid emerging from the jet wall and dissolving into the surrounding fluid (Bellan, 2000).

Although it is well-understood that liquid drops (or indeed a full two-phase spray)

cannot exist in a thoroughly supercritical flow, owing to the absence of any fluid interface, jets will still disintegrate. These fluid “chunks” will often travel in the midst of a large density gradient over their residence time, giving the appearance of an interface in optical data, obscuring their true nature. Foreknowledge of properties like this is essential to the experimentalist and modeler. Furthermore, Bellan stresses the importance of consistent terminology in describing the mixing of SC jets to avoid confusion between researchers and the readership. Evaporation refers to a strictly subcritical phenomenon where heat is added to a liquid droplet and mass is transferred across a tangible phase boundary into a surrounding gas. This is not possible at the SC condition, so rather the process of a “chunk” of high density SC fluid diffusing into a surrounding region is termed emission. Similarly, as sprays are also a subcritical phenomenon, a purely SC jet cannot undergo atomization. Such jets are said to disintegrate into chunks of SC fluid, after which further diffusion can occur (Bellan, 2000).

Bellan comments on two late 20th century experiments. An Army Research Laboratory (ARL) study measured a cryogenic jet injected into a supercritical chamber. The potential core of the methyl iodine jet was not well-defined by established density/coherence measurements and instead was defined only as a region with high concentration of injected fluid (Birk, 1995). Increased core penetration was found with increasing chamber pressure, consistent with results from literature. Here, this was speculatively attributed to injected fluid reaching critical temperature close to jet exit, inhibiting jet disintegration and lengthening the core. A study performed at the Air Force Research Laboratory (AFRL) investigated visual characteristics of round jets of nitrogen, helium and oxygen in subcritical and supercritical environments. A correlation was found

again between chamber/jet density ratio and jet disintegration and spatial evolution. In this experiment, however, the potential core was shown to become shorter and thinner with increasing chamber pressure, in contradiction to Birk et al. and many other observations from literature (Chehrودي, 1999). Bellan offers that this can be explained by a large temperature difference and therefore overall density difference between the ARL and AFRL experiments.

Commentary is also offered on numerical modeling efforts. Oefelein and Yang performed a LES study of LOX and H₂ shear layer combustion which employed a correlation for mass diffusivity between the liquid and gas states to come to a suitable SC value, however their method did not ensure this value reaches the proper zero value (another example of the thermodynamic singularity) at the critical point (Oefelein, 1998). Miller et al., in a DNS study developed a new sub-grid scale (SGS) turbulence model particularly suited to supercritical flows for future LES. This is important work as existing SGS models and RANS turbulence transport models were developed with subcritical fluids in mind (Miller, 2001). A steady-state, 2-D RANS simulation using k-epsilon closure and real-gas EoS and fluid properties was conducted by Ivancic et al., on combustion of a LOX jet into hydrogen at 6 MPa. The simulation predicted incorrect thickness and location of the OH species region, and Bellan attributes this to the significant simplifying assumptions in the model (steady and 2-dimensional in particular). SC fluids models must be transient, as the literature shows SC flow behavior is inherently unsteady (Bellan, 2000). A proper model is time-domain, has a real-gas EoS, and accounts for mixture non-ideality, increased solubility and Soret and Dufour effects. Numerical codes and models typically used to simulate jets and shear flows contain turbulence models, which were developed and tuned

for subcritical (and in many cases ideal) flows. Numerical tools remain lacking in this regard. Further, there is need for species-specific thermal diffusion factors (capturing Soret effect), multi-component mass diffusivities (capturing Dufour effect) and custom supercritically-based turbulence models (Bellan, 2000).

Vigor Yang contributes a review of modeling aspects in SC vaporization, mixing and combustion in liquid rockets. He immediately points out that in this regime, the already difficult problem of determining physical and chemical mechanisms in multiphase, chemically reacting flows is exacerbated by the inherent increase of Reynolds number accompanying very high operating pressure. Challenges also arise near the mixture critical point, as reported elsewhere in literature. Flow behavior in rocket engines is affected by two phenomena driving volumetric non-idealities: compressibility effects from pressure changes near the critical point and variable inertia effects from changes in chemical composition and heat addition, the latter effect being a product of the chemistry in the combustion chamber. Physical and chemical processes that result from the coupling of fluid dynamics, heat transfer, chemical kinetics, and thermodynamic and transport non-idealities have a wide range of time and length scales. Some of these scales are smaller than can be reasonably resolved numerically (Yang, 2000). The increased Reynolds number due to high pressure shrinks the scales of SGS phenomena.

Support is shown in this paper for a version of the Benedict-Webb-Rubin (BWR) cubic EoS modified by Jacobsen and Stewart, and its superior accuracy is compared to the conventional cubic real-gas equations (Benedict, 1940; Jacobsen, 1973; Yang, 2000). One drawback of using this high-fidelity equation is that model constants are only available for a small number of pure substances. An Extended-Corresponding-State (ECS) principle

developed by Ely and Hanley can be used to obtain transport properties, using BWR, of other single-phase fluids by conformal mapping temperature and density to that of a known reference fluid (Ely, 1981). This means constants are only required for the reference fluid. The BWR EoS is applied to the reference fluid in equation 6.

$$P_0(T, \rho) = \sum_{n=1}^9 a_n(T)\rho^n + \sum_{n=10}^{15} a_n(T)\rho^{2n-17}e^{-\gamma\rho^2} \quad (6)$$

Where P_0 is pressure of the reference fluid; T is temperature; ρ is density; γ is 0.04; and temperature coefficients $a_n(T)$ depend on the reference fluid. There are 15 temperature coefficients in this case.

Viscosity and thermal conductivity of mixtures can be obtained using ECS, as shown in equation 7.

$$\mu_m(\rho, T) = \mu_0(\rho_0, T_0)F_\mu \quad (7)$$

Where μ_m is dynamic viscosity of the mixture; the subscript 0 indicates properties of a reference fluid, and F_μ is the mapping function. It is worth noting that the ECS method cannot account for the contribution of molecular internal degrees of freedom in the calculation of thermal conductivity, and this term must be provided by a semi-empirical rule.

Yang demonstrates calculation of the thermodynamic properties with departure functions, as described by Branam, above. This method can potentially mitigate some of the complexity in modeling supercritical mixtures, by treating them in some respects as homogeneous “pseudo-pure” substances. Yang compares density calculations of several cubic EoS to experimental data from 70 to 430 K and 1-400 atmospheres. Peng-Robinson

gave a maximum relative error of 17%, SRK gave a maximum error of 13%, and the modified BWR gave a maximum error of 1.5% in this region. The BWR EoS must be solved iteratively for density at given pressure and temperature, increasing computational cost when used in density-based solvers. However, given its applicability to a large range of thermodynamic states and improved accuracy relative to other real-gas EoS, it remains valuable (Yang, 2000).

Barata also comments on a trend of increasing operating pressure in liquid-fueled rocket combustion chambers. In many engines, the fuel is injected into a chamber above the fuel's critical point, presenting design and analysis challenges that arise from a dearth of knowledge of supercritical turbulent jet mixing. The solubility of the gas phase in the liquid phase increases as chamber pressure approaches the critical value, while simultaneously, mixture effects need to be considered in calculating a mixture's critical point (Barata, 2003). According to Barata et al., Raman scattering studies demonstrate the biggest driver of jet growth is the thermodynamic state of the injected fluid, rather than jet speed. Jets in supercritical media have the same appearance as a gas jet, with a growth rate mirroring that of an incompressible, variable-density (low Mach numbers) jet.

A 2-D axisymmetric, steady, Favre-Averaged Navier-Stokes (FANS) study using k-epsilon closure was conducted on a cryogenic liquid jet injected into a chamber at supercritical temperature relative to the injected fluid. Favre averaging was used to obtain mass-averaged quantities in the conservation equations. This prevents the inclusion of terms involving density fluctuations, and reduces the number of models needed to solve the flow. Equation 8 shows a mass-averaged quantity obtained using Favre averaging, and momentum and continuity equations are presented in cylindrical polar coordinates for this

example, in equations 8-11.

$$\tilde{\phi} = \frac{\overline{\rho\phi}}{\bar{\rho}} \quad (8)$$

Where the overbar indicates an average given by the Reynolds decomposition.

$$\frac{\partial \bar{\rho} \widetilde{U} \widetilde{U}}{\partial x} + \frac{1}{r} \frac{\partial r \bar{\rho} \widetilde{U} \widetilde{V}}{\partial r} = -\frac{\partial \bar{P}}{\partial x} - \frac{1}{r} \frac{\partial r \bar{\rho} \overline{u'' v''}}{\partial r} \quad (9)$$

$$\frac{\partial \bar{\rho} \widetilde{U} \widetilde{V}}{\partial x} + \frac{1}{r} \frac{\partial r \bar{\rho} \widetilde{V} \widetilde{V}}{\partial r} = -\frac{\partial \bar{\rho}}{\partial x} - \frac{1}{r} \frac{\partial r \bar{\rho} \overline{v'' v''}}{\partial r} + \bar{\rho} \frac{\overline{w'' w''}}{r} \quad (10)$$

$$\frac{\partial \bar{\rho} \widetilde{U}}{\partial x} + \frac{1}{r} \frac{\partial r \bar{\rho} \widetilde{V}}{\partial r} = 0 \quad (11)$$

Where the tilde (\sim) overbar indicates a Favre decomposition, a straight overbar indicates a Reynolds decomposition, and a double overbar indicates a Favre decomposition of a Reynolds decomposition.

The authors note the code used was not written specifically for supercritical fluids, and care was taken to avoid numerical oscillations and divergence due to large density gradients. Several grids were tested, and high under-relaxation was used for the momentum equations (up to 90%). To best approximate the experimental conditions, a free-boundary was used for the wall on either side of the jet exit by setting constant pressure and obtaining velocity components from the continuity and momentum equations. This also required high under-relaxation to avoid divergence (Barata, 2003). Uniform axial velocity and zero radial velocity was set at jet exit, with 0.1% turbulence intensity and turbulent length scale equal to the initial jet diameter. Variation of turbulence parameters did not significantly impact flow development due to the uniform inlet velocity profile. Grid independence was evaluated by axial velocity decay.

Barata et al. compare results from this simulation to data from the Chehroudi 1999

paper suggesting gas jet-like behavior, as the code in this case was originally written for gaseous variable-density flows, and not supercritical flows (Barata, 2003). Potential core penetration was shown to decrease with increasing chamber pressure, matching Chehroudi's observations, and contradicting many others. Self-similarity is achieved between 8 and 12 jet diameters downstream, and otherwise the model reproduces most observations referenced previously, including growth rate and similarity in appearance to gaseous variable-density jets. These results give the authors confidence that a supercritical jet that looks like a gaseous jet can be modeled as one.

This paper takes a robust approach to modeling near-critical mixing and combustion, developing a holistic treatment of salient flow physics uniquely suited to SC flow. This is an unsteady RANS study using k-omega closure. Equations 12 and 13 represent the governing equations in conserved form.

$$\frac{\partial Q}{\partial t} + \frac{\partial E - E_v}{\partial x} + \frac{\partial F - F_v}{\partial y} = S \quad (12)$$

$$Q = (\bar{\rho}, \bar{\rho}\tilde{u}, \bar{\rho}\tilde{v}, \bar{\rho}\tilde{H}, \bar{\rho}k, \bar{\rho}\omega, \bar{\rho}\tilde{Y}_i) \quad (13)$$

Where Q is the vector of conserved variables; $\bar{\rho}$ is density; \tilde{u} and \tilde{v} are velocities; \tilde{H} is total enthalpy; k is turbulent kinetic energy and ω is its specific dissipation rate; and \tilde{Y}_i is the mass fraction of species i. E, E_v , F, and F_v are the inviscid and viscous flux vectors.

A modified version of the Peng-Robinson (PR) EoS is used for its wide range of applicability. The PR EoS is shown in equations 14-19 and is used later in this paper.

$$P = \frac{R_u T}{V_m - b} - \frac{a\alpha}{(V_m^2 + 2V_m b - b^2)} \quad (14)$$

$$a = \frac{0.45724R_u^2T_c^2}{P_c} \quad (15)$$

$$b = \frac{0.07780RT_c}{P_c} \quad (16)$$

$$\alpha = \{1 + \kappa(1 - T_r^{0.5})\}^2 \quad (17)$$

$$\kappa = 0.37464 + 1.54226\omega - 0.26992\omega^2 \quad (18)$$

$$T_r = \frac{T}{T_c} \quad (19)$$

Where P is pressure; R_u is the universal gas constant; V_m is molar volume; ω is the acentric factor, a property of molecule geometry; and T_c is the critical temperature and T_r temperature non-dimensionalized with respect to critical temperature, and referred to as reduced temperature.

The EoS is presented in polynomial (cubic) form in equations 20-22.

$$A = \frac{a\alpha P}{R_u^2 T^2} \quad (20)$$

$$B = \frac{bP}{R_u T} \quad (21)$$

$$Z^3 - (1 - B)Z^2 + (A - 2B - 3B^2)Z - (AB - B^2 - B^3) = 0 \quad (22)$$

Where Z is isentropic compressibility (Peng, 1975). A mixing rule proposed in (Miller, 2001) extends the above original form of the PR EoS to treat mixtures. This modified EoS is used to derive analytical expressions of thermodynamic quantities. Dynamic viscosity is computed by a two-equation method proposed by (Chung, 1984) and the ECS method of Ely and Hanley covered above was used to calculate thermal conductivity, using methane as the reference fluid (Cutrone, 2006). The authors discuss

two problems affecting convergence of time-marching schemes used in low speed flows. The first is machine round-off can cause floating point errors during calculation of the pressure gradient in the momentum equation. This can be solved by decomposing pressure into a constant and varying component, as with other variables. The second is the numerical stiffness of the governing partial differential equations. This can be improved by using a preconditioning matrix on the RANS equations in pseudotime, improving both convergence and stability (Cutrone, 2006). Cases are run on a 30,000 point grid, with a calculated y^+ of 1 at the walls.

This robust numerical treatment is first compared against the cold-flow case presented in (Branam, 2002) and compared well, using radial density profiles at 5 and 25 jet diameters. Such a mono-phase modeling approach is deemed suitable for a wide range of pressures and temperatures in the near- and supercritical regimes.

As chamber pressure exceeds its critical value, atomization no longer occurs, and as the fluid in the jet shear layer exceeds its critical temperature, inter-molecular forces reduce significantly. Diffusion-driven mixing mechanisms are promoted before atomization can take place, and the jet diffuses in a gas-like manner into the surrounding fluid. The result is a continuous fluid featuring no interface, but regardless possessing a very steep gradient of fluid properties in the radial direction (Cutrone, 2006). The injected cryogenic jet behaves optically like a single-phase gas jet rather than a liquid spray.

A transient RANS code is developed to study the turbulent mixing and combustion of cryogenic liquid nitrogen jets injected in a supercritical nitrogen chamber. Turbulence is captured by a modified k-epsilon model, and two real-gas EoS are used and compared. Real-gas thermodynamic properties are calculated using a dense fluid correction to an ideal

gas solution, similar to the departure functions mentioned previously. The method proposed in (Chung, 1984) is used to calculate dynamic viscosity and thermal conductivity. As this code is intended to model combustion as well as mixing, binary mass diffusion coefficients are first estimated for the low-pressure condition per a standard empirically correlated model in (Fuller, 1966) and high-pressure correction terms are added per (Takahashi, 1974). Although this added step will contribute to real-gas fidelity, modeling of the mass diffusion coefficients is still difficult for lack experimental data (Kim, 2011). Combustion is not treated in present work, and no further detail is provided on the combustion model. The extended k-epsilon turbulence model is seen in equations 23-25.

$$\frac{\partial}{\partial t}(\bar{\rho}\tilde{k}) + \frac{\partial}{\partial x_j}(\bar{\rho}\tilde{u}_j\tilde{k}) = \frac{\partial}{\partial x_j}\left(\frac{\mu_{eff}}{\sigma_k}\frac{\partial\tilde{k}}{\partial x_j}\right) + P_k - \bar{\rho}\tilde{\varepsilon} \quad (23)$$

$$\frac{\partial}{\partial t}(\bar{\rho}\tilde{\varepsilon}) + \frac{\partial}{\partial x_j}(\bar{\rho}\tilde{u}_j\tilde{\varepsilon}) = \frac{\partial}{\partial x_j}\left(\frac{\mu_{eff}}{\sigma_\varepsilon}\frac{\partial\tilde{\varepsilon}}{\partial x_j}\right) + \frac{\tilde{\varepsilon}}{\tilde{k}}(C_{\varepsilon 1}P_k - C_{\varepsilon 2}\bar{\rho}\tilde{\varepsilon}) \quad (24)$$

$$P_k = -\bar{\rho}\overline{u_i' u_j'} \frac{\partial \tilde{u}_i}{\partial x_j} \quad (25)$$

Where k is turbulent kinetic energy; ε is dissipation rate of turbulent energy; μ_{eff} is effective dynamic viscosity; σ_k , σ_ε , $C_{\varepsilon 1}$ and $C_{\varepsilon 2}$ are model constants; and P_k is the production rate of turbulent energy (Kim, 2011). This varies from the standard k-epsilon model in use of effective viscosity in place of turbulent viscosity, and use of a unique pre-calculation method, described below. Turbulent Prandtl number is 0.7 for this model.

A novel approach to decomposition is taken by Kim et al. in the use of a conserved scalar in concert with a presumed probability density function (PDF). Because the cold-flow case being tested here is chemically homogeneous and Mach number is low, the conserved scalar function is normalized static enthalpy. Every Favre-averaged scalar in the

solution vector is calculated by integrating the pre-calculation solution in conserved scalar domain, while weighted with a presumed beta PDF. These elements are shown in equations 26 and 27.

$$Z = \frac{h - h_{inj}}{h_{max} - h_{inj}} \quad (26)$$

$$\tilde{\phi}(\vec{x}) = \int_0^1 \tilde{P}(Z; \vec{x}) \phi(Z) dZ \quad (27)$$

Where Z is the conserved scalar; h_{max} is the maximum constant static enthalpy, in this case at an isothermally heated wall; h_{inj} is the minimum value of enthalpy at jet exit; ϕ is a thermodynamic or transport property contained in the governing equations; and \tilde{P} is a beta PDF. This method is used to represent scalar fluctuation effects on the real fluids in turbulent mixing near the critical point (Kim, 2011). PR and SRK model predictions are compared with NIST data for c_p and density. PR is found more accurate at predicting jet density profiles. These models were chosen for their accuracy for low-carbon fuels.

Supercritical fluids have thermodynamic and transport properties in between those of a liquid at the same pressure and a gas at the same temperature. The solubility is gas-like, and a strong function of pressure. Density and thermal diffusivity, however, are liquid-like, and strong functions of temperature (Kim, 2011). The supercritical combustion of cryogenic liquid propellants is tied to turbulent diffusion. Kim et al. identify the (many) important physical processes at play in high-pressure liquid propellant combustion: injection, real fluid effects, turbulent mixing, chemical kinetics, turbulence-chemistry interaction, flame-acoustics interaction and heat transfer (Kim, 2011). All are highly complex and all are in some way coupled with one another. Pseudoboiling was observed in model results. This occurs as heat is added to the inject SC fluid while near the

pseudocritical point. It is a point of heat transfer enhancement, as it is the temperature at which c_p and Z (isentropic compressibility) are maximum for a given pressure. Heat addition at this point will promote a relatively small increase in temperature, but a relatively large increase in specific volume (Kim, 2011). The test matrix transited the critical and pseudocritical points, and were therefore well-suited to validate the model. The pseudo-boiling phenomena had significant impact on flow development, and it was shown that strong pseudo-boiling increases the core penetration length and slows axial velocity decay.

The paper identifies a need for a comprehensive modeling approach to reduce the design-cycle cost for liquid-propellant rocket engines, as the industry's significant reliance on trial-and-error methods is expensive and time-consuming.

In a 2013 paper, Hickey and Ihme evaluate the capabilities of CharLES^x, a cleverly-named LES solver developed at Stanford University's Center for Turbulence Research and now sold by Cascade Technologies, a spin-off of the CTR. Motivation for this work is to test real-fluid extensions to the code, and a desire to model mixing and combustion in liquid rocket engines where injected fuel and oxidizer become supercritical during combustion. It is believed better modeling tools are key to predicting combustion instability (Hickey, 2003).

CharLES^x is an unstructured LES code, using a 3rd-order Runge-Kutta explicit solver in time and a hybrid 4th-order centered solver in space. The space-domain solver uses a density gradient trigger to switch to a 1st- or 2nd-order Essentially Non-Oscillatory (ENO) solver if gradient passes through a preset threshold. This mitigates numerical dissipation and convergence issues for flow solutions that may contain large gradients, shocks or other discontinuities. The SGS model is an eddy-viscosity model developed for

turbulent shear flow, per (Vreman, 2004). The PR cubic EoS is used for density calculations, but as this equation was developed for pure fluid, mixing rules for applicability to mixtures are added from (Miller, 2001) and the critical properties of these mixtures are calculated with mixing rules from (Harstad, 1997). Departure functions derived from the PR EoS, also per (Miller, 2001), compute thermodynamic properties and transport properties are per (Chung, 1984). A full description of the combustion model is available in (Hickey, 2013). The Navier-Stokes equations are solved in fully conservative form. For non-reacting flows (which will be compared to current work), pressure and temperature are calculated iteratively with a Newton-Raphson method from transported quantities internal energy and density.

The pertinent simulation run by Hickey and Ihme is compared to the 2002 experiment by Branam & Mayer of a cryogenic nitrogen jet injected into a chamber of supercritical nitrogen. A 2D grid was constructed consisting of a total 225,000 control volumes. Results from this cold-flow simulation give good overall agreement with experiment, and the trend of a centerline density plot matches the Branam & Mayer data quite well. This will be shown below. Jet breakup is however predicted approximately one jet diameter early. Even in this relatively simple simulation case, the authors note that local pressure oscillations caused by a highly non-linear EoS and large density gradients forced them to add numerical viscosity to the model. This promotes artificial dissipation, enhancing stability. This is achieved by switching the low-order spatial solver between 2nd-order ENO and a 1st-order scheme, suppressing oscillations. While this helps with convergence, this added dissipation modifies the solution, particularly in flows transitioning to turbulence. The authors believe more work is necessary to eliminate this

apparent tradeoff between accuracy and stability (Hickey, 2003).

Applications of Supercritical Fluid Modeling

One of the motivations for the study of this type of turbulent mixing is its application to thermodynamic cycles featuring supercritical CO₂. Suo-Anttila and Wright write on modeling a s-CO₂ cycle with C3D, a commercial CFD package, and adding real fluid capability by importing a library of fluid property data. REFPROP is a library made available by the National Institute of Standards and Technology (NIST) containing thermodynamic and transport data for a variety of pure substances and mixtures over a wide range of thermodynamic states. By using real fluid data in table format in the solver, the user can avoid much model complexity, but at the cost of “look-up” time (added computational expense). This technique can be quite advantageous for certain modeling needs, but currently the library does not contain data for many species at combustion temperatures. C3D is often used to model fires and other combustion, and as such has demonstrated its ability to handle large property gradients. Flow properties can vary by factors of 4 or 5 over short distances during the simulation of a fire (Suo-Anttila, 2011). The energy equation in the solver was changed from internal energy (based on specific heats, which vary by a large margin near the critical point) to enthalpy to avoid computational instability.

The code was used to model natural circulation of s-CO₂ in a nuclear reactor cooling circuit produced by pipe temperature gradients. The data compared well with experiment in (Milone, 2009), indicating that this commercial code, with real fluid functionality, is a useful tool in predicting both natural and forced convection of

supercritical fluid in pipes (Suo-Anttila, 2011).

Yoonhan et al. provide an overview of the advantages of the s-CO₂ Brayton cycle for power generation. Gen 4 nuclear reactors will operate at temperatures between 500-900° C, higher than the 300° C typical of current water-cooled reactors (Yoonhan, 2015). By increasing the turbine inlet temperature (TIT), a larger exchange of energy between working fluid and turbine is possible, and an increase in thermal efficiency is achieved. Many of today's reactors use a large volume of cooling water, and concerns surrounding their environmental impact remain very real. A closed cycle s-CO₂ cooling circuit could reduce the ecological footprint of new reactors. Currently, at high TIT (> 550° C) an ultra-supercritical (USC) steam cycle is required. Gains in thermal efficiency are unfortunately mitigated by the increase in material degradation from high temperature and pressure steam (Yoonhan, 2015).

The s-CO₂ Brayton cycle combines the advantages of the steam Rankine and air Brayton (gas turbine) cycles. In this new cycle, fluid is compressed at a thermodynamic state of low isentropic compressibility (Z), requiring less compressor work compared to a steam Rankine cycle. At the same time, TIT is higher than the steam cycle, and comparable with the air Brayton cycle, but without the blade and seal degradation issues inherent to steam (Yoonhan, 2015). The minimum pressure in the cycle is higher than any steam Rankine cycle, which means fluid is dense throughout the cycle. This translates to a lower volumetric flow rate, making the required turbomachinery potentially 10 times smaller than in an equivalent steam cycle.

While the working pressure is higher here than the steam Rankine cycle, pressure ratio is smaller across the turbine, which increases the turbine outlet temperature. Heat

recuperation downstream of the turbine therefore has a large influence on the efficiency of the cycle (Yoonhan, 2015). Owing to the heat transfer enhancement unique to supercritical fluids, specific heat of cold-side flow is 2-3 times higher than hot side flow in recuperators, enabling a “recompressing layout” to enjoy high efficiency while reducing waste heat to the environment.

A high heat exchanger effectiveness is required to realize the gains outlined in this paper. This cycle presents a substantial motivation for the application and development of printed circuit and microtube heat exchangers.

Key advantages of the s-CO₂ cycle are: a 5% increase in thermal efficiency over the steam Rankine cycle, a four-fold reduction in overall system size, a reduction in purification system requirements owing to higher minimum operating pressure above the CO₂ critical point, and its wide range of applicability to energy sources e.g. nuclear, indirect fossil, direct-fire fossil, geothermal, solar-thermal (Yoonhan, 2015).

3. Model Setup

The current work is the evaluation of modeling requirements and identification of salient flow physics in the turbulent mixing of a cryogenic nitrogen jet injected into a chamber at supercritical temperature and pressure relative to the injected fluid. The settings and configuration of the numerical models used are detailed sufficiently here to enable reproduction of this work and results presented in the following chapter.

Code, Benchmark and Computational Grid

STAR-CCM+ is a commercial computational fluid dynamics code marketed by Siemens Product Lifecycle Management Software Inc. Versions 10.06.010 and 12.02.011 of the code are used in this paper. Simulation efforts necessarily begin by attempting to reproduce the results of others (Branam, 2003; Hickey, 2013). The author has elected to attempt replication of the turbulent mixing of a cryogenic nitrogen jet injected into a large chamber of quiescent supercritical nitrogen. Relevant experiment setup data are presented in Table 3.1.

Table 3.1 Experiment Data (Branam, 2002)

Nitrogen Critical Temperature	126.19 K
Nitrogen Critical Pressure	3.398 MPa
Chamber Pressure	4.0 MPa
Chamber Temperature	298 K
Jet Initial Temperature	126.9 K
Injector Diameter	2.2 mm
Jet Speed	5.04 m/s
Reynolds Number (Re)	165,859

The Reynolds number is calculated using equation 1.

$$Re = \frac{\rho u D}{\mu} \quad (1)$$

Where ρ is the density, u is the streamwise velocity, D is a characteristic length here taken as the injector diameter, and μ is the dynamic viscosity. Velocity is given, and density and dynamic viscosity are obtained from the NIST Chemistry WebBook using chamber pressure and injected jet temperature (NIST, 2017). This is a necessary step given the real gas effects in this thermodynamic region (Bellan, 2000). Figure 4.1 is an illustration of the DLR experimental setup.

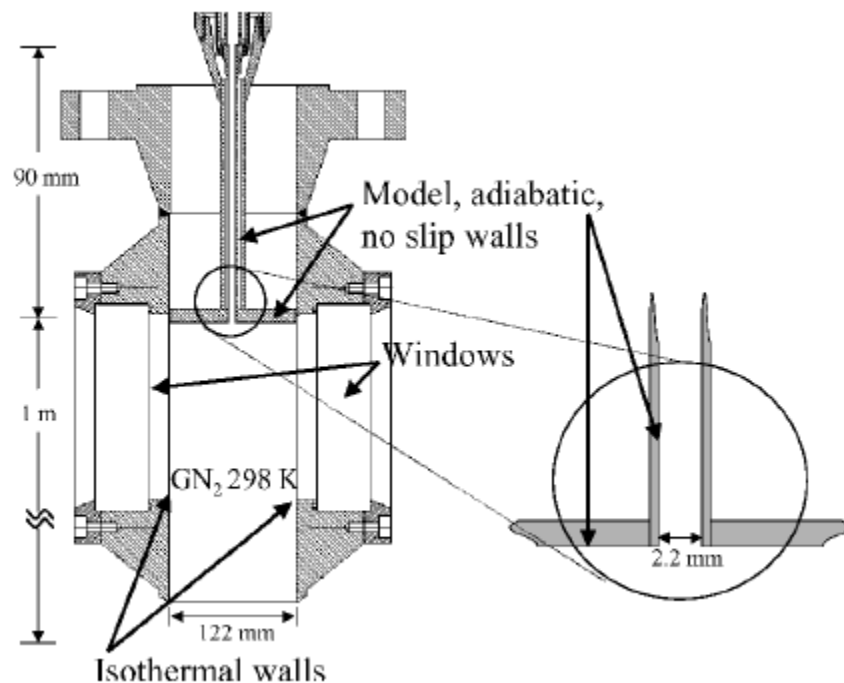


Figure 3.1 Experimental Setup (Branam, 2002)

The size of the chamber is deemed large compared to the injector area and the flow field to be studied. Wall effects are neglected, and the far wall is sufficiently far from jet exit that it is effectively decoupled from the flow (Hickey, 2013). Several numerical models were validated against this simple non-reacting experiment, and several were included for the literature search for this work. A sophisticated LES study was published by Hickey and Ihme in 2013 to evaluate new real fluid capabilities of the code, and has been selected as a

i-direction						
Smoothness, j-direction	1.000	1.000	1.000	1.000	1.000	1.000
Minimum Included Angle	89.988	86.655	89.989	86.084	89.990	85.514
Maximum Included Angle	93.345	90.012	93.916	90.011	94.486	90.010
Skewness	0.037	0.000	0.044	0.000	0.050	0.000

Quarter jet mesh quality data is presented in Table 3.3.

Table 3.3 3D Grid Quality

	Maximum	Minimum
Cells	11,496,060	
Volume Ratio	3.000	1.000
Length Ratio, i-direction	1.020	1.000
Length Ratio, j-direction	1.029	1.000
Length Ratio, k-direction	1.000	0.000
Aspect Ratio	497.1637	1.43419
Smoothness, i-direction	1.000	1.000
Smoothness, j-direction	1.000	1.000
Smoothness, k-direction	1.000	0.500
Minimum Included Angle	88.5	3
Maximum Included Angle	99.392	90.040
Equiangle Skewness	0.95	0.017
Centroid Skewness	0.266	0.000

Structured meshes were selected based on the precedent set in the literature in similar modeling studies, and in particular with the selected benchmark case. Current work is expected to require a finer mesh size, as much of the literature modeling relies on 4th or even 6th order solvers, and STAR-CCM+ only includes 2nd-order time and space solvers for RANS simulations. STAR-CCM+ is an unstructured solver with a built-in unstructured mesh builder, but accepts structured imported grids as well. Originally a much coarser

quarter-jet mesh was built, but simulations did not converge and data did not represent realistic flow behavior. The grid was refined to a cell count at the upper limit of reasonable computational expense, but unfortunately the author could not find grids in the literature with which to compare. A one-cell-thick 3D mesh was created based on the existing 2D meshes to circumvent the code's 3D requirement, but unfortunately this also failed to converge. Large maximum volume ratio, aspect ratio and skewness in the quarter-jet LES mesh are likely contributors to error. A new mesh will be generated in future work.

STAR-CCM+ Coupled Flow Solver

The coupled flow solver computes the conservative form of the mass, momentum and energy conservation equations simultaneously as a vector. Velocity is obtained from the momentum equation, pressure is obtained from the continuity equation, and density is obtained from the equation of state. This is the suitable method for non-smooth flows, or flows with variable density. The governing equations are presented in vector form in equations 2 - 5.

$$\frac{\partial}{\partial t} \int \mathbf{W} dV + \oint [\mathbf{F} - \mathbf{G}] \cdot d\mathbf{a} = \int \mathbf{H} dV \quad (2)$$

$$\mathbf{W} = \begin{bmatrix} \rho \\ \rho \mathbf{v} \\ \rho E \end{bmatrix} \quad (3)$$

$$\mathbf{F} = \begin{bmatrix} \rho \mathbf{v} \\ \rho \mathbf{v} \mathbf{v} + P \mathbf{I} \\ \rho \mathbf{v} H + P \mathbf{v} \end{bmatrix} \quad (4)$$

$$\mathbf{G} = \begin{bmatrix} 0 \\ \mathbf{T} \\ \mathbf{T} \cdot \mathbf{v} + \dot{q}'' \end{bmatrix} \quad (5)$$

Where \mathbf{W} is the vector of conserved variables, \mathbf{F} is the vector of convective terms, \mathbf{G} is the vector of diffusion terms, ρ is density, \mathbf{v} is velocity, E is total energy per unit mass, P is pressure, \mathbf{I} is the identity tensor, \mathbf{T} is the tensor of viscous stresses, H is total enthalpy, \dot{q}'' is the heat flux vector, and \mathbf{H} is a vector of body forces.

At low Mach numbers, as discussed in the literature, this system of equations tends to become numerically stiff, introducing stability and convergence issues. A preconditioning matrix, typically denoted as uppercase gamma, is applied to the unsteady term in equation 4.2 to improve the convergence rate, as shown in equations 6 and 7 (Weiss, 1995).

$$\Gamma \frac{\partial}{\partial t} \int \mathbf{Q} dV + \oint [\mathbf{F} - \mathbf{G}] \cdot d\mathbf{a} = \int \mathbf{H} dV \quad (6)$$

With,

$$\Gamma = \begin{bmatrix} \frac{1}{U_r^2} - \frac{\rho_T}{\rho c_p} & 0 & \rho_T \\ \left(\frac{1}{U_r^2} - \frac{\rho_T}{\rho c_p} \right) \mathbf{v} & \rho \mathbf{I} & \rho_T \mathbf{v} \\ \left(\frac{1}{U_r^2} - \frac{\rho_T}{\rho c_p} \right) H - \delta & \rho \mathbf{v} & \rho_T H + \rho c_p \end{bmatrix} \quad (7)$$

Where ρ_T is the time derivative of density at constant pressure, c_p is specific heat at constant pressure, δ is a model parameter (1 for ideal gases, 0 for incompressible fluids), and U_r is a reference velocity designed to help the system of equations cope with disparate convective and diffusive time scales. In an unsteady model, necessary to properly simulate a supercritical jet (Bellan, 2000), the preconditioning solution is stepped in pseudo-time, in an inner loop between physical time steps (Weiss, 1995).

Reynolds-Averaged Navier-Stokes

The full Navier-Stokes equations are not solved numerically in STAR-CCM+. Instead, they are subjected to a Reynolds decomposition, resulting in the Reynolds-Averaged Navier Stokes (RANS) equations. The Reynolds decomposition consists of breaking a solution variable into parts, as shown in equation 8.

$$\phi = \bar{\phi} + \phi' \quad (8)$$

Where ϕ is a primitive variable such as pressure, or a velocity component, $\bar{\phi}$ is an averaged value, and ϕ' is its fluctuating component. For a steady solution, this averaging is analogous to time-averaging, and for unsteady solutions, it is an average of inner iterations. The mean-value momentum conservation equation now contains an extra term, as shown in equations 9 and 10.

$$\frac{\partial}{\partial t}(\rho\bar{\mathbf{v}}) + \nabla \cdot (\rho\bar{\mathbf{v}}\times\bar{\mathbf{v}}) = -\nabla \cdot \bar{P}\mathbf{I} + \nabla \cdot (\mathbf{T} + \mathbf{T}_t) + \mathbf{f}_b \quad (9)$$

Where \mathbf{T}_t is the Reynolds stress tensor,

$$\mathbf{T}_t = -\rho \begin{bmatrix} \overline{u'u'} & \overline{u'v'} & \overline{u'w'} \\ \overline{u'v'} & \overline{v'v'} & \overline{v'w'} \\ \overline{u'w'} & \overline{v'w'} & \overline{w'w'} \end{bmatrix} \quad (10)$$

Closure to the RANS equations is achieved by modeling this tensor in terms of the averaged value of primitive variables (Reynolds, 1895). This is most commonly performed by an eddy-viscosity model.

k-Omega SST Turbulence Model

All eddy viscosity turbulence models are based on the Boussinesq hypothesis, which states that the momentum transfer associated with turbulent eddies can be

approximated with an eddy viscosity term, μ_t (Boussinesq, 1877). Equation 11 shows how the Reynolds stress tensor can now be made proportional to the mean strain rate tensor.

$$\mathbf{T}_t = 2\mu_t \mathbf{S} - \frac{2}{3}(\mu_t \nabla \cdot \bar{\mathbf{v}}) \mathbf{I} \quad (11)$$

This relationship assumes isotropy in turbulence, and for most flows and ideal gases this does not present a significant problem. However, in near- and supercritical media, where flow variables, thermodynamic properties and transport properties can all have large spatial and temporal gradients, the Boussinesq assumption is probably not appropriate. Additionally, the fluctuating component of the Reynolds decomposition described above assumes constant fluid properties. These effects can effectively “smear-out” real-fluid phenomena during model run-time and currently represent a fundamental limitation to RANS models with respect to SC fluids.

k-omega SST is a two-equation turbulence model noted for its superior performance in calculating boundary layers with adverse pressure gradients, jets and shear flows, and its versatility in simultaneously handling wall-bounded flows and the freestream without modification (Menter, 1994). It is less sensitive to inlet boundary conditions than the also widely-used k-epsilon two-equation model. It uses two new transport properties, a turbulent kinetic energy term, k , and a specific turbulent dissipation rate, ω . SST is presented in equations 12 and 13.

$$\frac{\partial}{\partial t}(\rho k) + \nabla \cdot (\rho k \bar{\mathbf{v}}) = \nabla \cdot [(\mu + \sigma_k \mu_t) \nabla k] + P_k - \rho \beta^* f_{b^*} (\omega k - \omega_0 k_0) \quad (12)$$

$$\frac{\partial}{\partial t}(\rho \omega) + \nabla \cdot (\rho \omega \bar{\mathbf{v}}) = \nabla \cdot [(\mu + \sigma_\omega \mu_t) \nabla \omega] + P_\omega - \rho \beta f_\beta (\omega^2 - \omega_0^2) \quad (13)$$

Where σ_k and σ_ω are model coefficients, P_k and P_ω are production terms, f_{b^*} is the

free-shear modification factor, and f_β is the vortex stretching modification factor.

Large Eddy Simulation

STAR-CCM+ also features an LES solver. Large eddy simulation is seen as a compromise between the computationally expedient but lower-fidelity RANS and computationally prohibitive but highly realistic Direct Numerical Simulation (DNS) approaches to modeling. A decomposition of flow variables still takes place, but instead of Reynolds averaging, the variables are split spatially according to the size of the computational grid, as shown in equation 14.

$$\phi = \tilde{\phi} + \phi' \quad (14)$$

Where the tilde overbar represents the filtered value, and the prime represents the sub-grid value. The filtered values are used in governing equations of the same form seen above in the RANS model. The added turbulent stress tensor term \mathbf{T}_t , however, now represents stresses on the subgrid scale, as shown in equation 15.

$$\mathbf{T}_t = 2\mu_t \mathbf{S} - \frac{2}{3}(\mu_t \nabla \cdot \tilde{\mathbf{v}} + \rho k) \mathbf{I} \quad (15)$$

Where $\tilde{\mathbf{v}}$ is the large-scale filtered velocity and k is SGS turbulent kinetic energy. This still constitutes a Boussinesq assumption, but on a much smaller scale than with turbulence closure methods used with Reynolds averaging. With LES, flow is fully resolved (no turbulence model required) on scales larger than the grid size, and a sub-grid scale (SGS) model achieves turbulence closure on the smallest scales. STAR-CCM+ offers three choices of SGS model. The default model, Wall-Adapting Local-Eddy Viscosity (WALE) is similar to the older Smagorinsky SGS model, with the advantages of less

sensitivity to model coefficient choices no requirement of near-wall damping, similar to Menter's SST contribution to the k-omega model (Nicoud, 1999).

NIST REFPROP Data

Thermodynamic and transport properties of nitrogen were extracted from REFPROP, a software package released by NIST, using an open-source MATLAB script and compiled into .csv files. These files contain pressure-temperature tabulated fluid properties and partial derivatives, and were imported into each STAR-CCM+ simulation file. The code linearly interpolates these tables at each iteration, assigning a realistic fluid property for each thermodynamic state. Properties were sampled from the library from 64 K to 1000 K and from 0 MPa to 5 MPa, at 500 temperature levels and 500 pressure levels. Speed of sound, specific heats, enthalpy, thermal conductivity, dynamic viscosity, density and entropy were included in the model.

Boundary and Initial Conditions

The 2D computational domain has five boundaries: two walls bounding the flow in the transverse direction, an outlet, a wall bounding the inlet, and the inlet itself. A pressure outlet set to ambient pressure was selected at the outlet boundary, as this is the recommended boundary type for this flow regime and solver type, and is typical of the literature. No additional settings were changed at the outlet. No-slip, adiabatic walls were selected for all three wall locations. No additional settings were changed for the wall boundaries.

The experiment specified an operating pressure, inlet temperature and injected jet velocity, so a velocity inlet was selected to the injector boundary. For the first several

simulations, only injection velocity and temperature were changed on the inlet. All other properties and values were left at default. Attempting to better match results, inlet conditions were adjusted to represent the fully-developed turbulent pipe flow at jet exit described in the experiment (Bellan, 2002). Velocity inlet settings are shown in Table 3.4.

Table 3.4 Inlet Boundary Condition Parameters

	Initial Runs	Matching Experiment
Static Temperature	126.9 K	126.9 K
Turbulence Intensity	0.01	0.0356
Turbulent Length Scale	0.01 m	8.36 E-5 m
Velocity Magnitude	5.04 m/s (constant)	Nikuradse Profile, Mean Velocity 5.04 m/s

Turbulence intensity and length scale were calculated based on mean flow velocity and injector diameter according to equations 16 and 17 (Siemens PLM).

$$I = 0.16Re^{-\frac{1}{8}} \quad (16)$$

$$L_0 = 0.038D_h \quad (17)$$

Where D_h is the hydraulic diameter of the channel.

The Nikuradse velocity profile, shown in equation 18, is a relatively flat function of pipe radius (y-distance) representative of fully-developed turbulent flow (Tuoc, 2009).

$$\frac{u}{\bar{u}} = \left(\frac{y}{R}\right)^{\frac{1}{n}} \quad (18)$$

Where \bar{u} is a time averaged velocity at pipe centerline, R is pipe radius, and n is a parameter depending on Reynolds number. Here, $n=7$ for $Re \approx 10^5$.

The 3D quarter-jet boundary conditions are similar, with the inclusion of periodic interfaces on the bottom and left symmetry planes (matching the flow solution on these surfaces) and modeling the inlet velocity profile as a function of radius rather than height.

First cases were run with an initially flat solution space at chamber temperature and pressure. The STAR-CCM+ Coupled Solver's Expert Initialization feature was used to produce an approximate inviscid flow solution. This feature initializes the pressure, velocity and temperature fields and reduces overall computation time.

Model settings: RANS

Physics models included in RANS simulations are presented in Table 3.5.

Table 3.5 Physics Models Used in RANS Simulation

Implicit Unsteady	User Defined EOS*	Two Dimensional
All $y +$ Wall Treatment	SST (Menter) K-Omega	K-Omega Turbulence
Reynolds-Averaged Navier-Stokes	Coupled Energy	Exact Wall Distance
Turbulent	Gradients	Coupled Flow
Gas		

* A number of initial runs were made using the Ideal Gas and Peng-Robinson Real Gas equations of state but this configuration represents the bulk of results presented below.

Most of the models described in the literature use very high order solvers. In STAR-CCM+ RANS, the highest available solvers were selected: 2nd-order implicit in space and 2nd order implicit in time. The Expert Driver feature was enabled in the Coupled Solver to help balance stability and convergence rate. It includes an algorithm to automatically throttle the Courant-Friedrichs-Lewy (CFL) number. Reasonable residual convergence was achieved using a time step of 5E-6 s and 10 iterations per time step.

Model Settings: LES

Physics models included in LES cases are presented in table 4.6.

Table 3.6 Physics Models Included in LES Simulation

Coupled Energy	All $y +$ Wall Treatment	Exact Wall Distance
WALE Subgrid Scale	Large Eddy Simulation	Turbulent
User Defined EOS	Gradients	Coupled Flow
Gas	Implicit Unsteady	Three Dimensional

Using LES in STAR-CCM+ gives the user access to higher order solvers. The MUSCL 3rd-order/CD solver was selected in space and 2nd-order implicit solver selected in time. The MUSCL solver is intended for highly-accurate simulations of aeroacoustics and aerodynamics and has a built in gradient threshold trigger that switches to a lower-order solver to maintain stability. Nominally it is a blended 3rd-order upwind/3rd-order centered-difference solver, and switches to a 1st-order ENO solver when high gradients are encountered. Time stepping was not refined for this model to the extent of the RANS case, as the computation time LES demands required focus to be returned to RANS simulation. Time step here was 3E-4 s, with 15 iterations per time step. A coarse time step is a likely source of error in LES results.

Original Test Case Matrix

Table 3.7 outlines the original benchmarking test matrix

Table 3.7 Benchmarking Test Matrix

RANS	Subcritical Jet, Ideal Gas EoS	SC Jet, PR EoS	SC Jet, REFPROP data
LES	Control case	Tune Inlet Conditions	Grid/Time Step Independence

The LES model was initially found more sensitive to inlet conditions than the RANS model, and an incremental approach to benchmarking was desired. As the original intent was an applied study of mixing for injector design, this was to be followed by an

aggressive campaign of simultaneous RANS simulations on local computing assets and LES simulations on a parallel cluster. Results would then be compared to evaluate the fidelity of the less computationally-expensive method. Table 3.8 outlines the intended path.

Table 3.8 Nominal Test Matrix

RANS	LES
Introduce Crossflow to Single Jet	Introduce Crossflow to Single Jet
Introduce Coaxial Shell Flow (Oxidizer), Quiescent Chamber	Introduce Coaxial Shell Flow (Oxidizer), Quiescent Chamber
Multispecies Coaxial Flow	Multispecies Coaxial Flow
Multispecies Co-Axial Flow into Crossflow	Multispecies Co-Axial Flow into Crossflow
Combustion Case, Tabular Combustion Method	Combustion Case, Tabular Combustion Method

Challenges with LES and Lessons Learned

Simply stated, a gross underestimation was made of the processor-hours required to perform a thorough LES treatment of a domain of this size. Flow times on the order of 0.1 s take approximately 24 hours using 72 processors with the current grid, and a large number of runs are necessary to tune and debug a LES simulation. Achieving a benchmark and generating a new grid with more complicated flow and geometry (and wall effects) and troubleshooting the new grid in the required time was, in hindsight, unrealistic. The work necessary for an unsteady combustion simulation campaign in a poorly-understood thermodynamic regime is also likely beyond the scope of a Master's thesis. There remains, however, much to be learned from results that were obtained.

Revised Test Case Matrix

Qualitative LES results were achieved for one case, but mesh independence was

not established, and there are notable differences to previous work. Effort was refocused on 2D RANS modeling to ensure that some meaningful results were obtained in the time permitted, and to enable some qualitative conclusions to be drawn. The final test matrices are presented in Table 3.9, Table 3.10, and Table 3.11.

Table 3.9 Test Case Matrix: Supercritical Jet

Supercritical Jet – User-Defined EoS			
Steady		Unsteady	
1 st -Order Solvers	2 nd -Order Solvers	1 st -Order Solvers	2 nd -Order Solvers
Reference Mesh	Reference Mesh	Reference Mesh	Reference Mesh
Mesh Level 2	Mesh Level 2	Mesh Level 2	Mesh Level 2
Mesh Level 3	Mesh Level 3	Mesh Level 3	Mesh Level 3

Table 3.10 Test Case Matrix: Atmospheric Jet, User-Defined EoS

Atmospheric Jet – User-Defined EoS			
Steady		Unsteady	
1 st -Order Solvers	2 nd -Order Solvers	1 st -Order Solvers	2 nd -Order Solvers
Reference Mesh	Reference Mesh	Reference Mesh	Reference Mesh
Mesh Level 2	Mesh Level 2	Mesh Level 2	Mesh Level 2
Mesh Level 3	Mesh Level 3	Mesh Level 3	Mesh Level 3

Table 3.11 Test Case Matrix: Atmospheric Jet, Ideal Gas EoS

Atmospheric Jet – Ideal Gas EoS			
Steady		Unsteady	
1 st -Order Solvers	2 nd -Order Solvers	1 st -Order Solvers	2 nd -Order Solvers
Reference Mesh	Reference Mesh	Reference Mesh	Reference Mesh
Mesh Level 2	Mesh Level 2	Mesh Level 2	Mesh Level 2
Mesh Level 3	Mesh Level 3	Mesh Level 3	Mesh Level 3

Grid Independence

Grid independence was evaluated by comparing density and axial velocity plots

along the jet centerline and axial velocity profiles at several streamwise locations. Comparisons are made using time-averaged data on unsteady solutions. Independence is established at mesh level 2. The Reynolds number independence was not considered, as SC jet mixing behavior is seen in the literature to depend chiefly on the thermodynamic state of the injected fluid rather than injection speed (Zong, 2004). Centerline density for all three grid levels is presented in Figure 3.2.

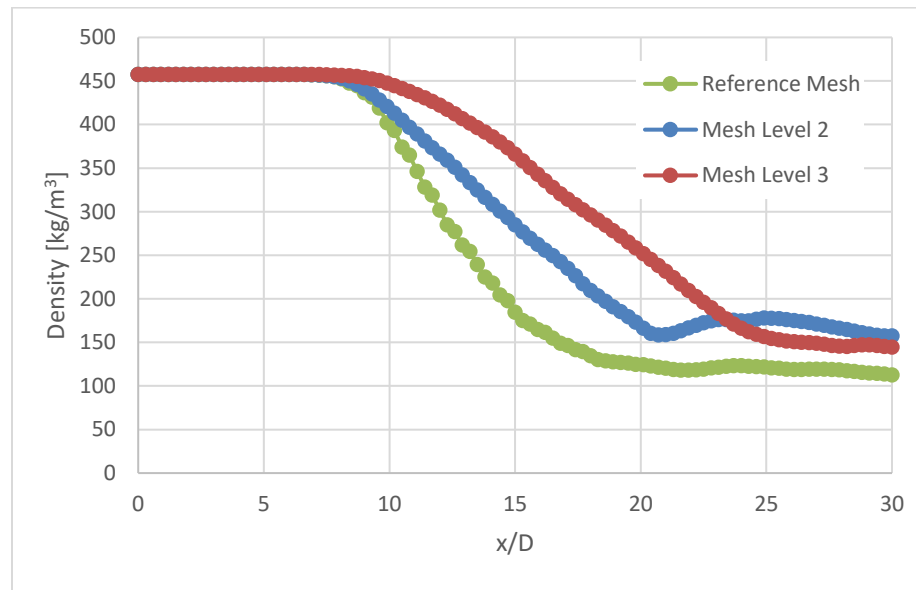


Figure 3.2 Centerline Density: Unsteady RANS

Three important features are very similar between these three plots. Core penetration is approximately 8-10 jet diameters for all cases. Centerline density appears to approach 150 kg/m^3 at 30 jet diameters in all cases. The slope of density decay in the transition zone matches closely between grid levels 2 and 3, and grid independence is declared for mesh level 2 for this criterion. Centerline axial velocity is compared in Figure 3.3.

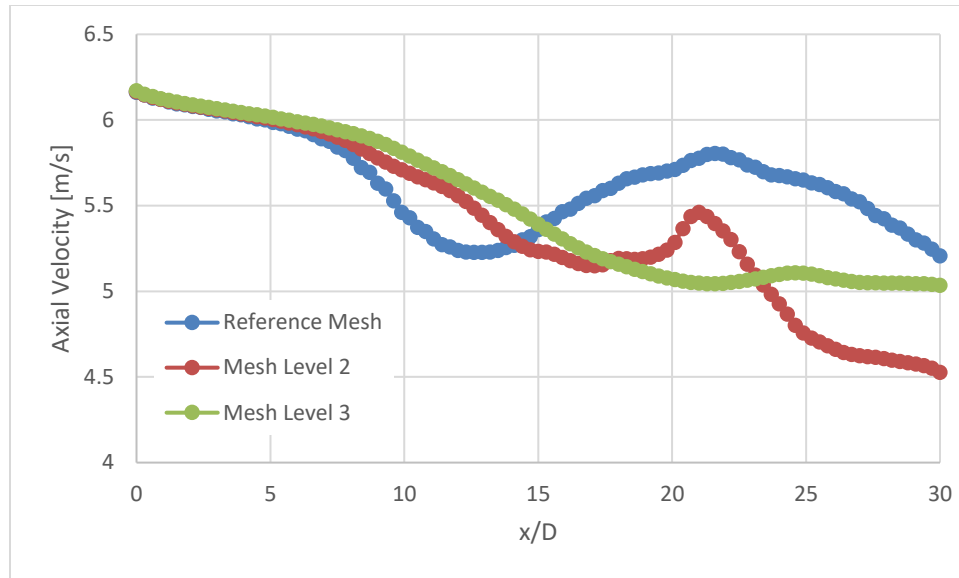


Figure 3.3 Centerline Axial Velocity: Unsteady RANS

These time-averaged plots are more susceptible to noise due to vortex-induced motion, but, with the exception of a peak near 20 jet diameters in the second plot, the decay trend is captured by grid levels 2 and 3 here. Grid independence is declared for mesh level 2 for this criterion. Normalized axial velocity profiles at 10, 20, 30 and 50 jet diameters are presented in Figure 3.4, Figure 3.5, and Figure 3.6.

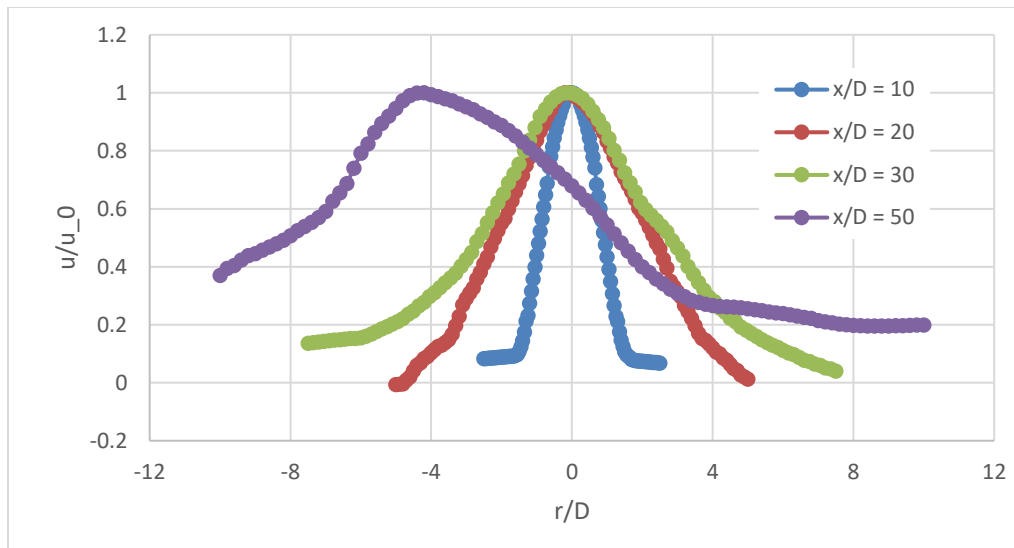


Figure 3.4 Axial Velocity Profiles: Unsteady RANS, Reference Mesh

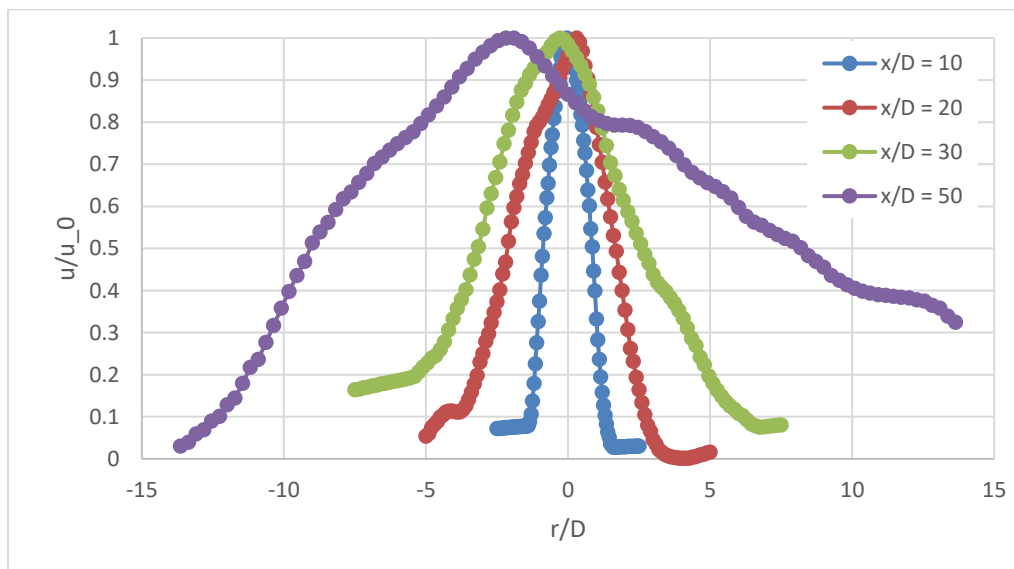


Figure 3.5 Axial Velocity Profiles: Unsteady RANS, Mesh Level 2

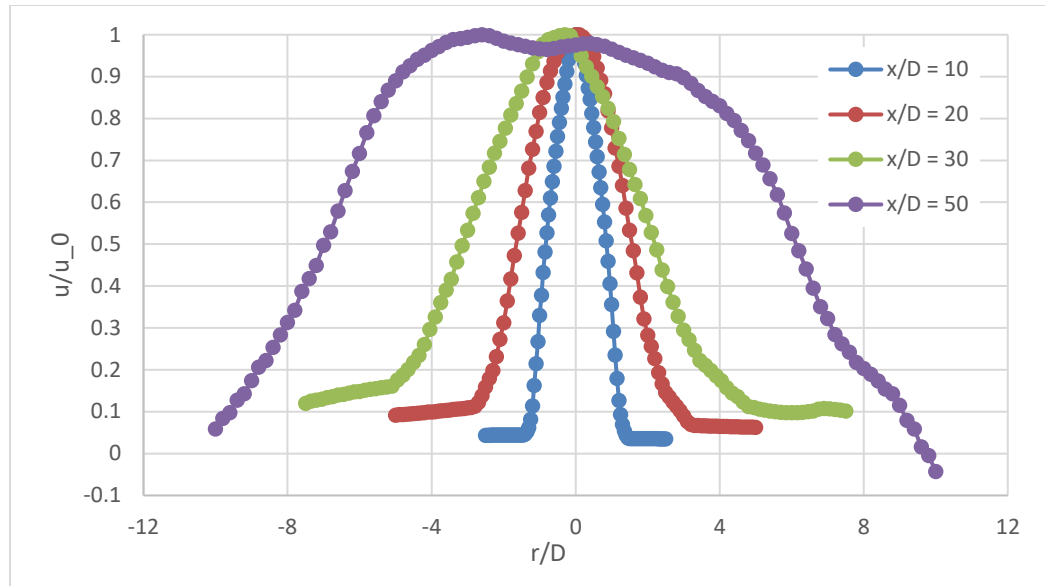


Figure 3.6 Axial Velocity Profiles: Unsteady RANS, Mesh Level 3

With the exception of the axial velocity distribution at 50 jet diameters, this data matches quite well in all three cases. Grid independence from this perspective is achieved at the reference grid level. Overall, grid independence is declared at grid level 2, and that data is used for unsteady RANS results in the following section.

4. Results and Discussion

The following chapter presents and discusses data gathered from several RANS simulations and one LES simulation of a test case from a 2002 Branam and Mayer experiment (Branam, 2002). Current data is compared to the original experimental data as well as results from an LES simulation conducted by Hickey and Ihme using Stanford's CharLES^x solver. First is a walkthrough of initial incremental RANS benchmarking efforts. This is followed by the author's attempt to harness the power and accuracy of LES, and finally an extensive comparison of RANS results using NIST REFPROP data.

Preliminaries: First Steps in Benchmarking

An incremental approach to modeling supercritical fluids was taken to ensure the best possible matching of previous results. Elements of added complexity were added one at a time, beginning with a subcritical case using software default settings. If the reader prefers to proceed directly to results, they are discussed for unsteady RANS and LES using real fluid properties and inlet conditions are presented in the next section.

An atmospheric jet using the ideal gas EoS is first simulated for illustrative purposes, and for comparison to supercritical cases using the same code. Several initial steady-state runs were based on half-jet grids with a symmetry plane along the jet centerline. This grid is equivalent to the top half of the reference grid described in the previous section and an example is shown in Figure 4.1.

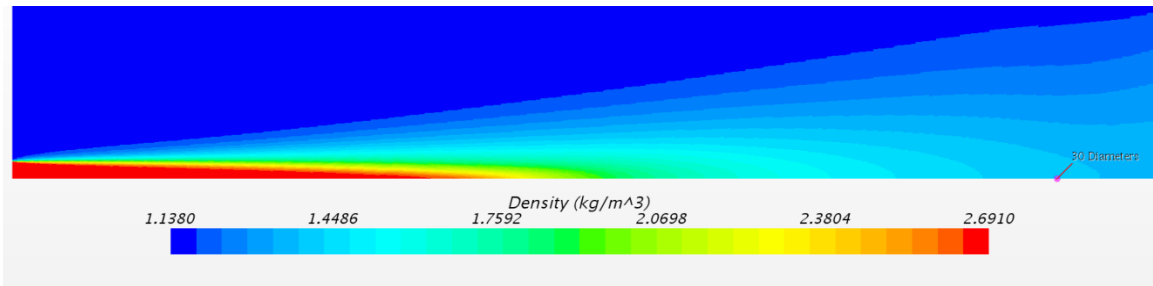


Figure 4.1 Half-jet velocity contour, reference mesh

Density is plotted along the jet centerline for a subcritical jet in Figure 4.2.

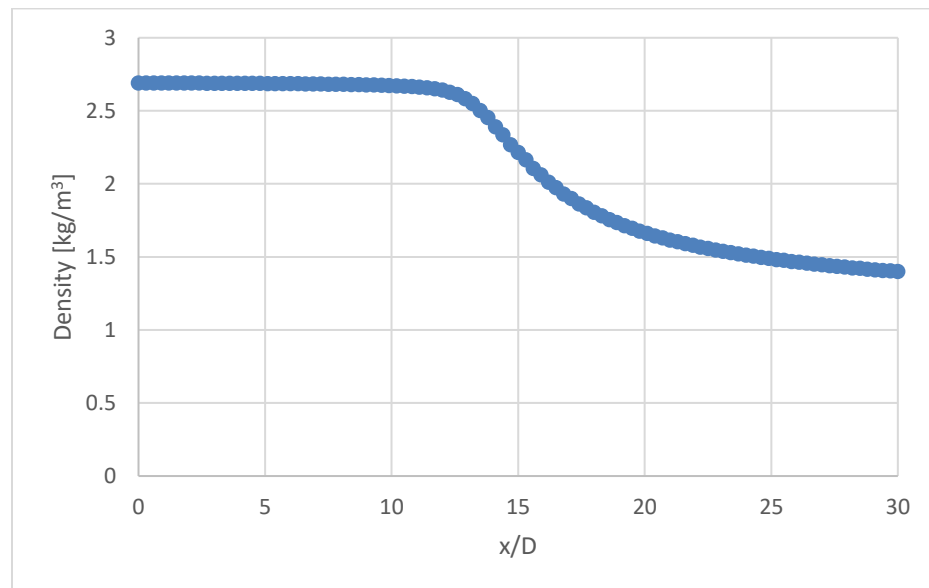


Figure 4.2 Centerline Density of a 1 atm jet using ideal gas EoS

This illustrates typical single-phase gas jet behavior. A relatively intact potential core is seen penetrating to approximately 12 jet diameters, a transition region follows as jet density decays between 12 and 25 jet diameters, and self-similarity is achieved in the vicinity of 30-40 jet diameters. The half-jet grid is used because of a jet curving tendency tentatively attributed to baroclinic torque, as discussed in (Zong, 2004). This is examined in Figure 4.3 and Figure 4.4.

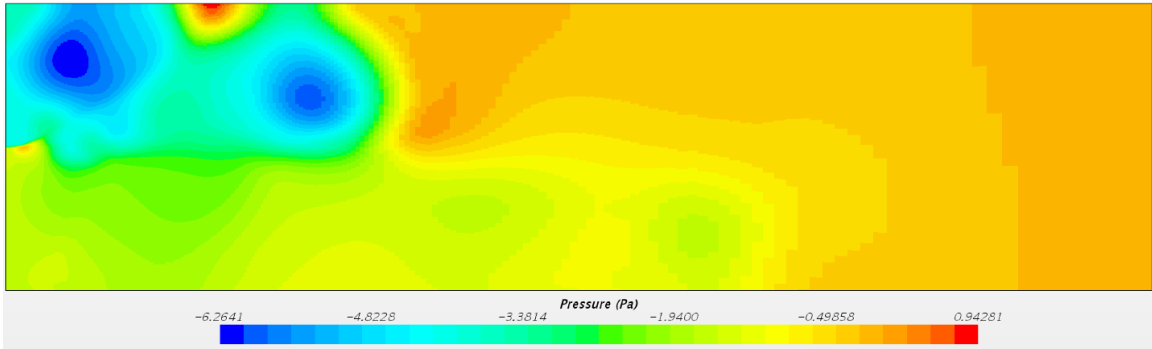


Figure 4.3 Pressure contour of a steady-state jet

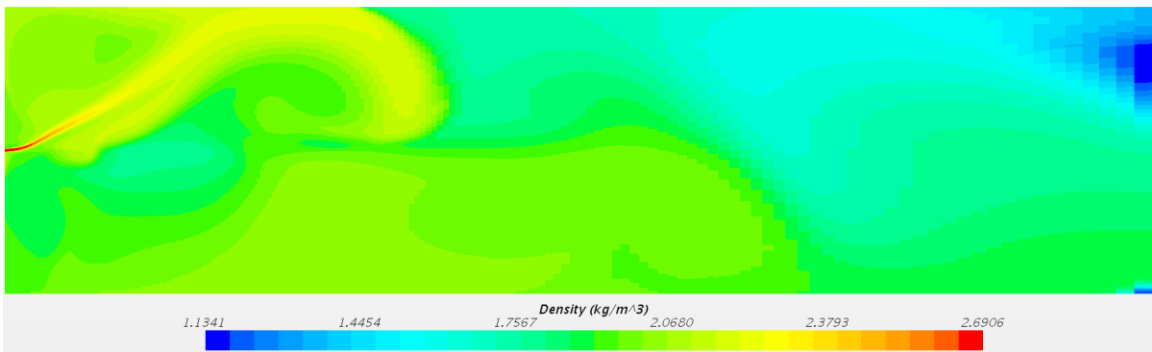


Figure 4.4 Density contour of a steady-state jet

This causes curvature in the jet, complicating analysis of velocity profiles and properties along the centerline. For this reason, all data for steady jets is taken from half-jet grids. This does not significantly impact results, as the flow physics of the jets of interest is inherently unsteady, and is analyzed as such (Bellan, 2000).

It is obvious that the ideal gas EoS is not suitable for a simulation at supercritical temperature and pressure. At 4 MPa and 298 K, the chamber conditions of Bellan's 2002 experiment, the ideal gas law under-predicts density by approximately 50%. The Peng-Robinson real gas EoS is substituted into the model. A brief error analysis is performed to ascertain its accuracy relative to the ideal gas EoS, as shown in Figure 4.5, Figure 4.6, Figure 4.7 and Figure 4.9.

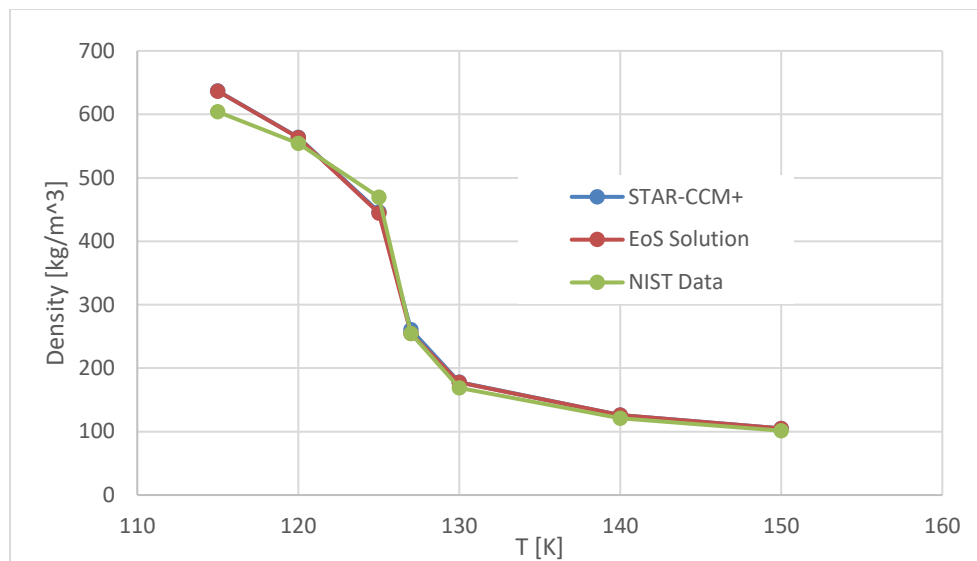


Figure 4.5 N2 Density Calculation Using PR EoS Compared to NIST Data on a 3.5 MPa Isobar

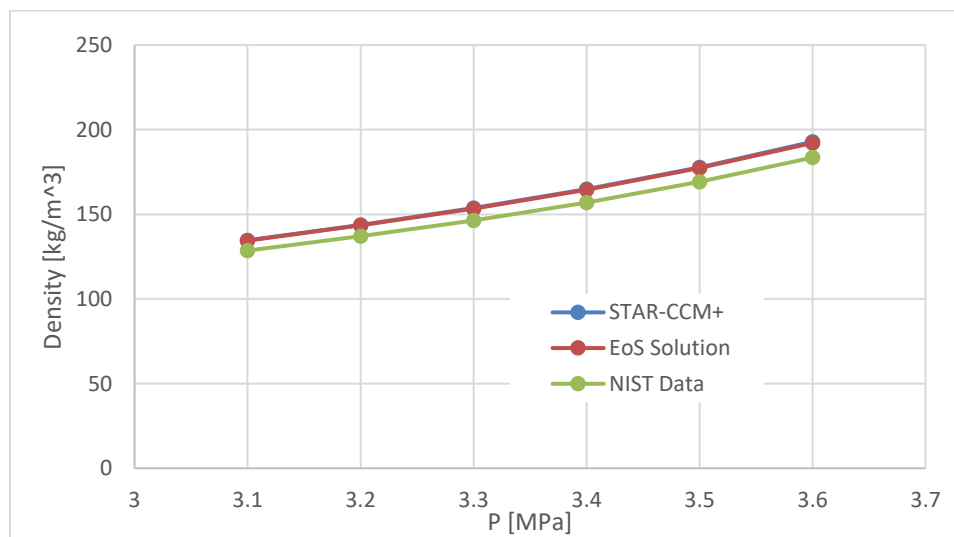


Figure 4.6 N2 Density Calculation Using PR EoS Compared to NIST Data on a 130 K Isotherm

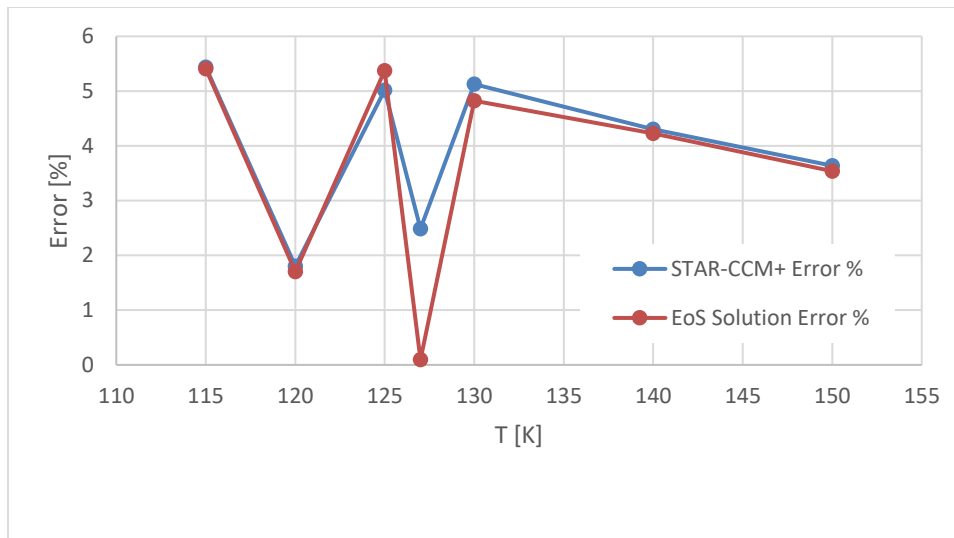


Figure 4.7 Percent Error of Density Calculation on an Isobar

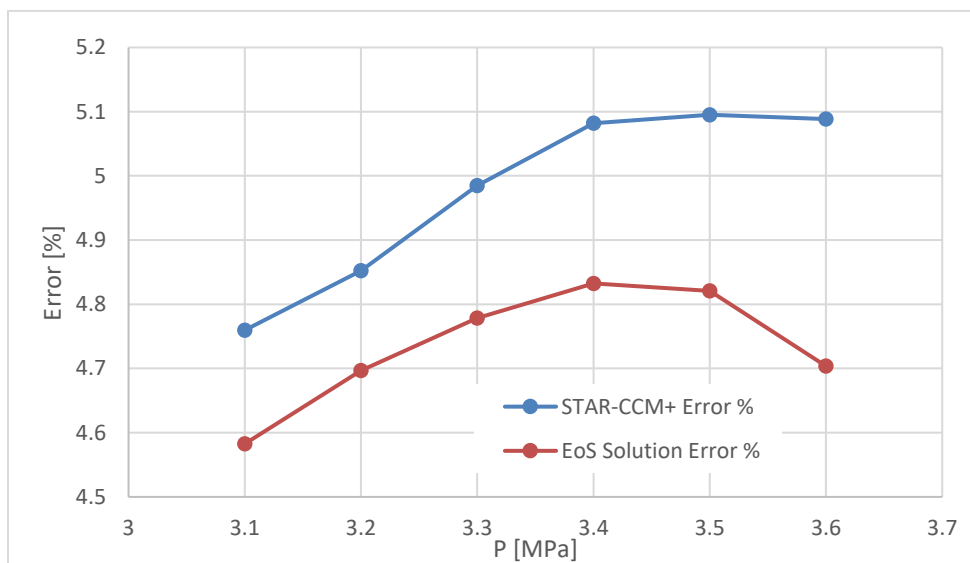


Figure 4.8 Percent Error of Density Calculation on an Isotherm

This compares well with the EoS errors cited in the literature for density calculations, and errors of approximately 5% are generally considered acceptable in this region. A centerline density plot for a STAR-CCM+ steady supercritical jet, using the PR EoS, is shown in Figure 4.9.

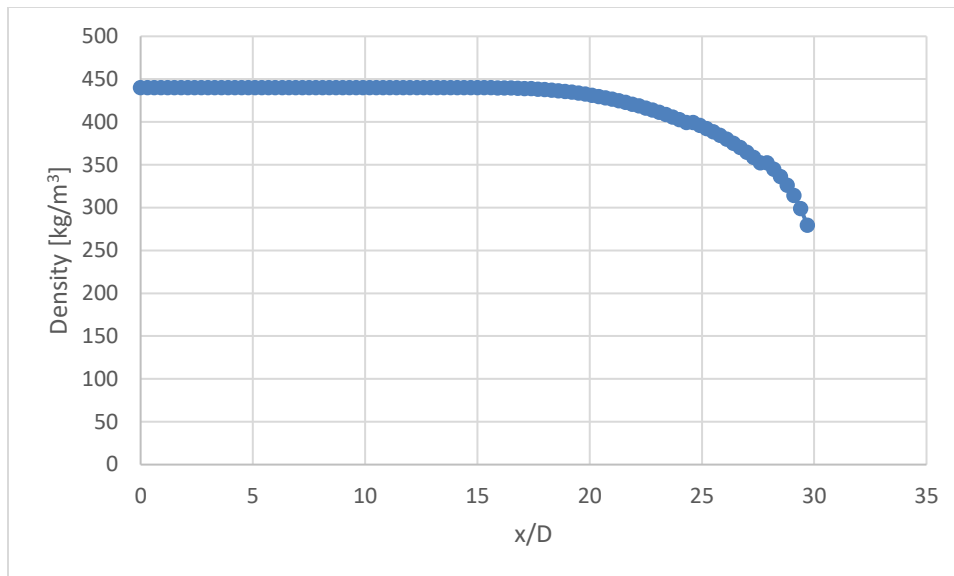


Figure 4.9 Centerline Density of a supercritical jet using the PR EoS, constant properties

The proper density ranges at experiment operating conditions are now represented. The density profile is compared to published CharLES results from Hickey and Ihme, matching experimental data from Branam and Mayer's much cited 2002 experiment (Hickey, 2013) in Figure 4.10.

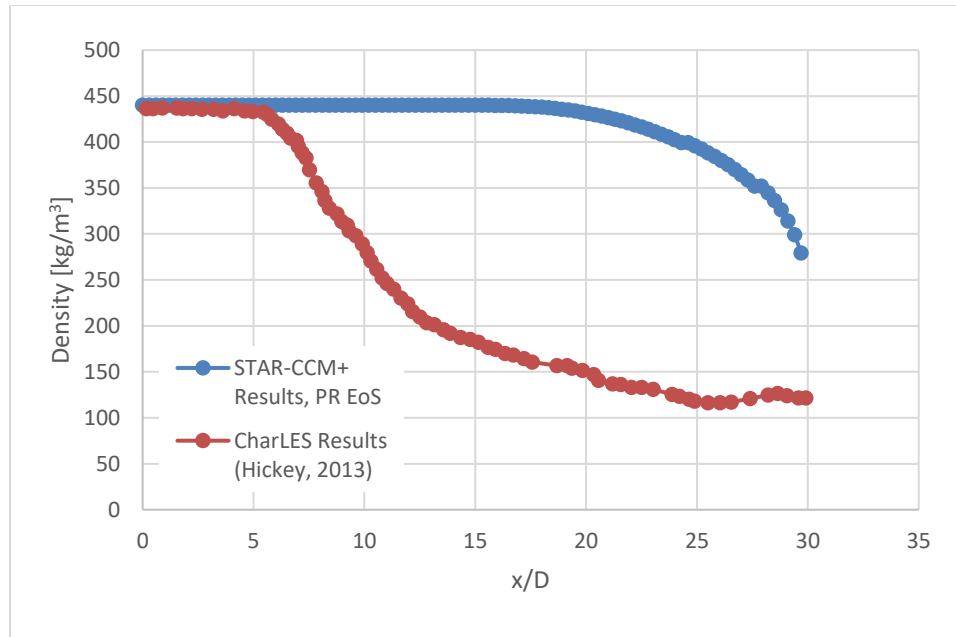


Figure 4.10 Centerline Density Comparison to CharLES results

The current model captures centerline density decay, but does not contain the characteristic sharp inflection at the end of the potential core and overpredicts the core penetration. To this point, simulations have been run assuming constant fluid properties, including viscosity, specific heat, and thermal conductivity. The literature makes it quite clear that this is an unrealistic assumption, given the degree to which fluid properties vary in this thermodynamic regime. Going forward, a user-defined EoS is used, consisting of complete nitrogen property data stored in pressure-temperature lookup tables which are extracted from the NIST code REFPROP, and imported into the STAR-CCM+ simulation files. Figure 4.11 shows the effect of this change on the density profile.

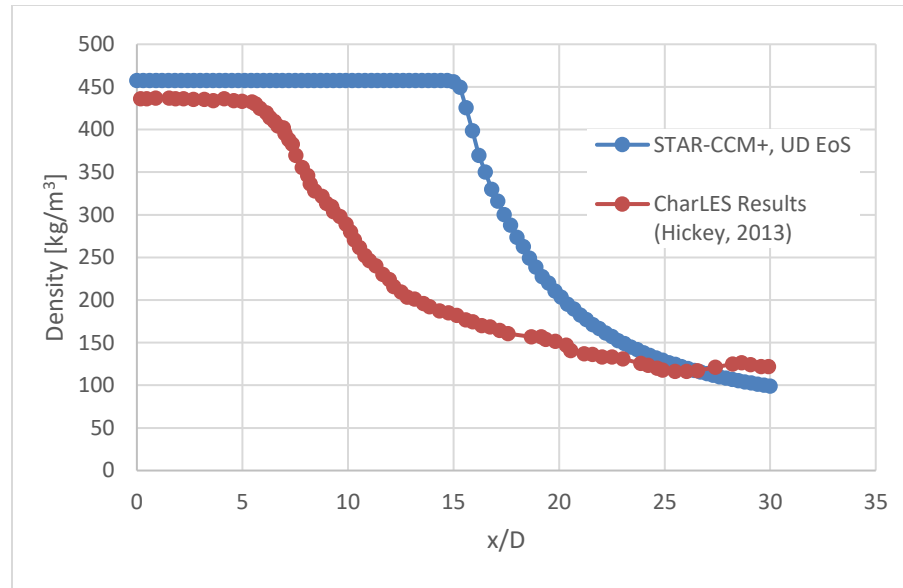


Figure 4.11 Centerline Density Comparison to CharLES Results, User-Defined EoS

Potential core penetration is significantly reduced, and self-similar region density approaches previous results. This is good evidence that use of real fluid properties adds fidelity to the simulation. The LES case is presented next in some detail.

LES Results

Large eddy simulation was run for 680 ms of flowtime (sufficient for more than 3 flow-throughs) in a symmetrical quarter jet, in a grid of approximately 11.5 million control volumes. Jet exit velocity profile, turbulence intensity and turbulent length scales are configured to represent fully developed turbulent pipe flow. Axial velocity profile giving a mean flow velocity of 5.04 m/s at jet exit is presented in Figure 4.12.

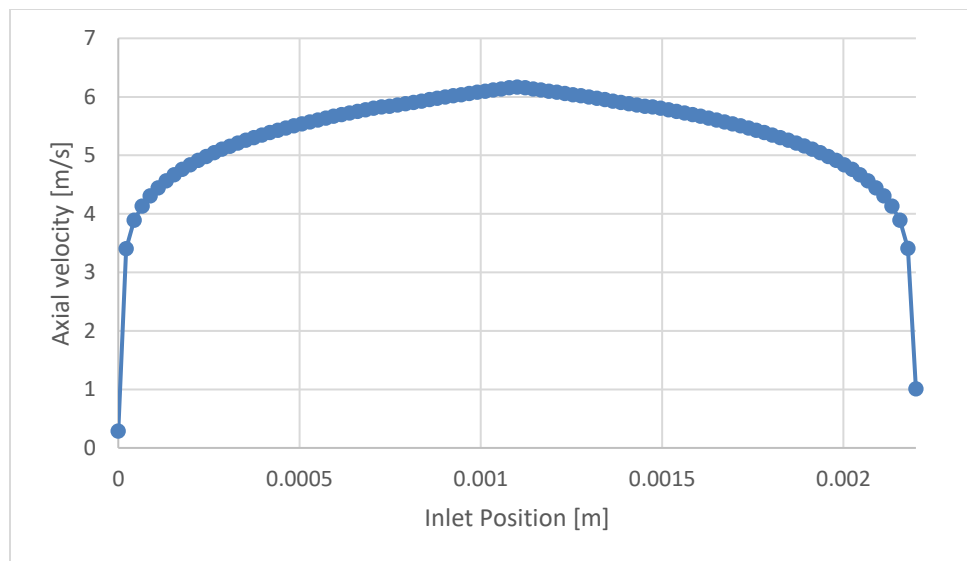


Figure 4.12 Nikurasde Fully Developed Turbulent Flow Velocity Profile

Figure 4.13, Figure 4.14, Figure 4.15 and Figure 4.16 compare velocity magnitude and temperature contours to CharLES results from (Hickey, 2013). CharLES contours are white-hot, with velocity range of 0-5.6 m/s, and temperature range of 125.6 to 306.7 K.



Figure 4.13 Velocity Magnitude Contour, CharLES Results (Hickey, 2013)

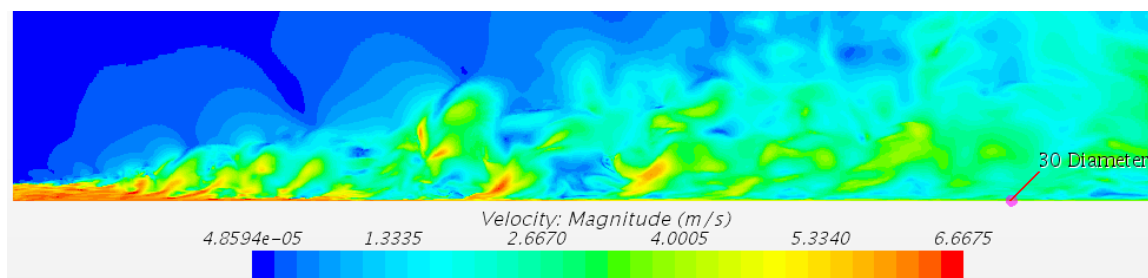


Figure 4.14 Velocity Magnitude Contour, LES Results, Current Work



Figure 4.15 Temperature Contour, CharLES Results, (Hickey, 2013)

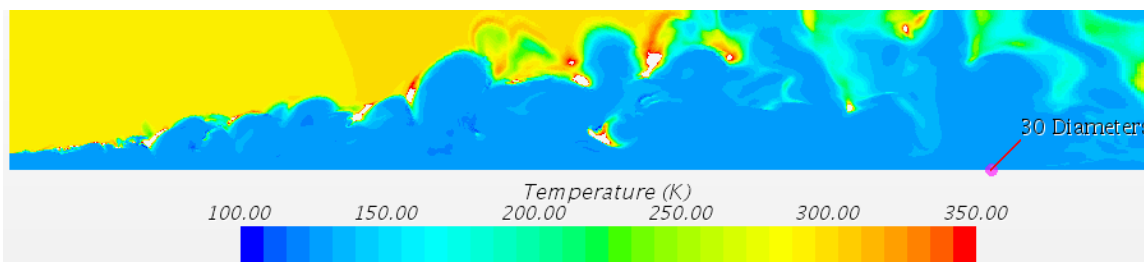


Figure 4.16 Temperature Contour, LES Results, Current Work

These snapshot contours indicate that similar flow feature scales are being captured in both simulations, but diffusion of jet velocity and temperature is slower in current work.

Jet centerline density for the current simulation is shown in Figure 4.17.

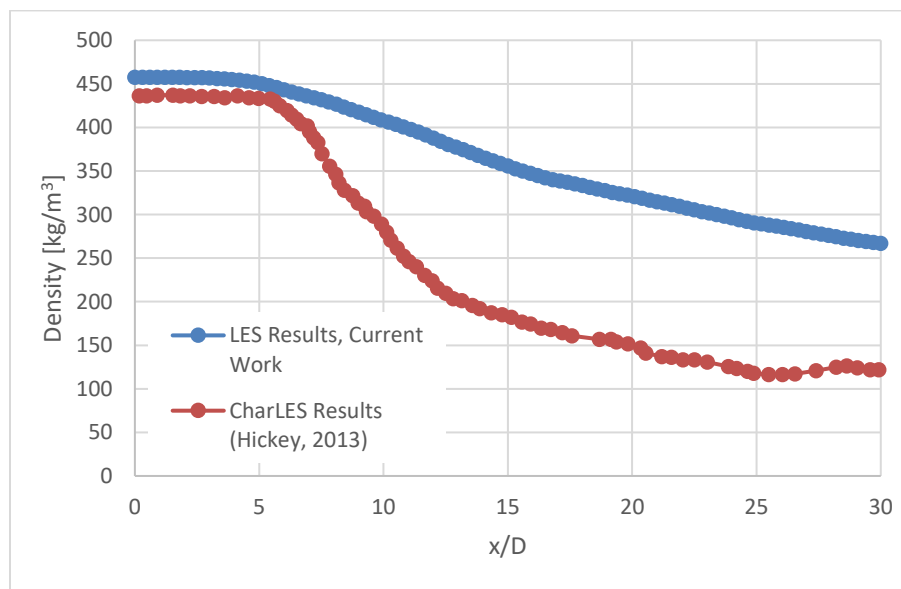


Figure 4.17 Centerline Density, LES Results, 680 ms Flowtime, Current Work

The trend of decay is captured, but potential core penetration again does not exactly

match previous results. The penetration length is however closer to previous work, but STAR-CCM+ LES here under-predicts the penetration by approximately 2 jet diameters.

RANS Results: Comparison with Previous Work

Velocity magnitude and temperature (snapshot) contours are compared to CharLES results in Figure 4.18, Figure 4.19, Figure 4.20, and Figure 4.21.

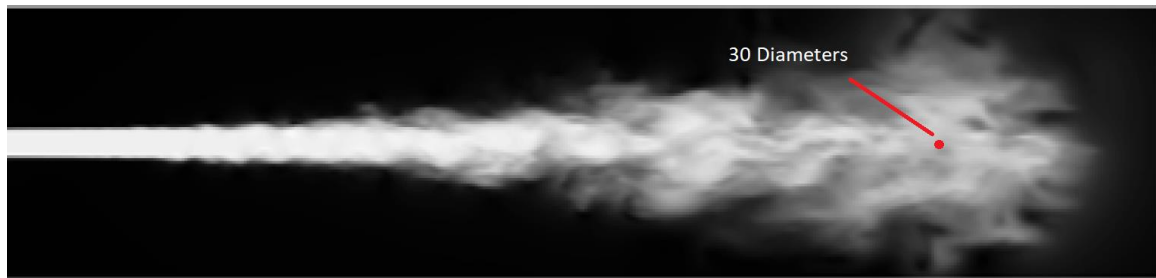


Figure 4.18 Velocity Magnitude Contour, CharLES Results, (Hickey, 2013)

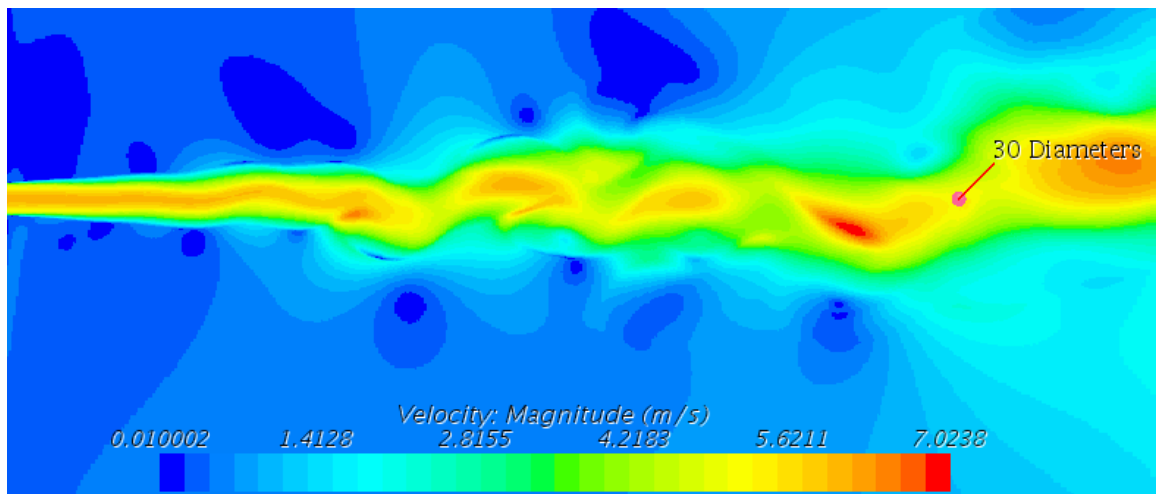


Figure 4.19 Velocity Magnitude Contour, RANS Results, Current Work



Figure 4.20 Temperature Contour, CharLES Results, (Hickey 2013)

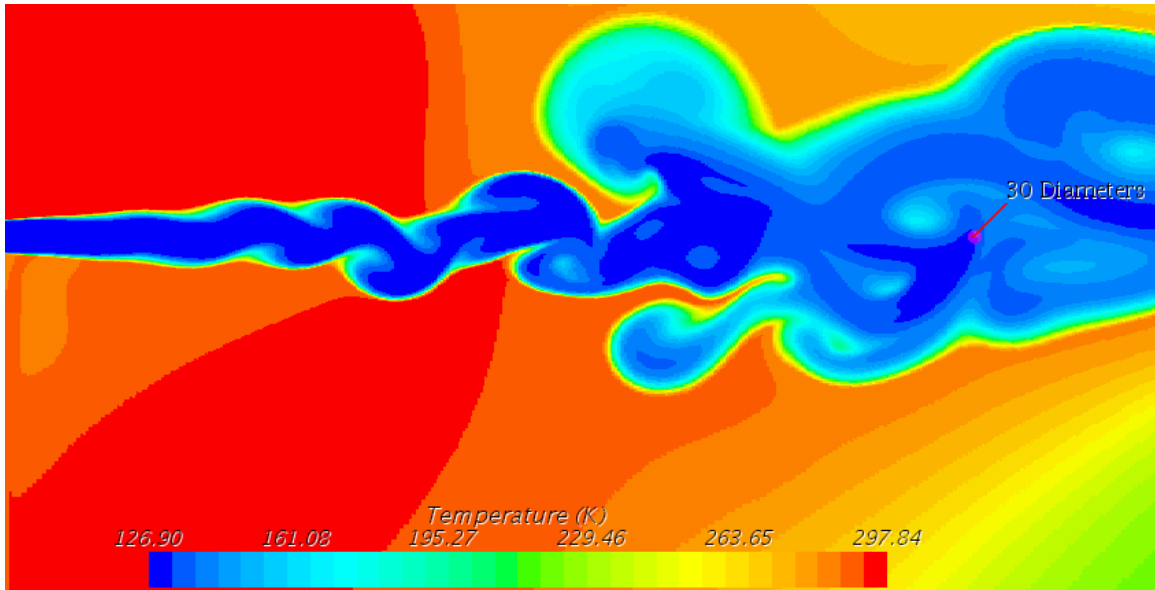


Figure 4.21 Temperature Contour, RANS Results, Current Work

Again, velocity magnitude and temperature are diffused much more quickly in CharLES results, and flow feature scale is coarser in this RANS simulation. Centerline density decay is better predicted compared with CharLES, however, as shown in Figure Figure 4.22.

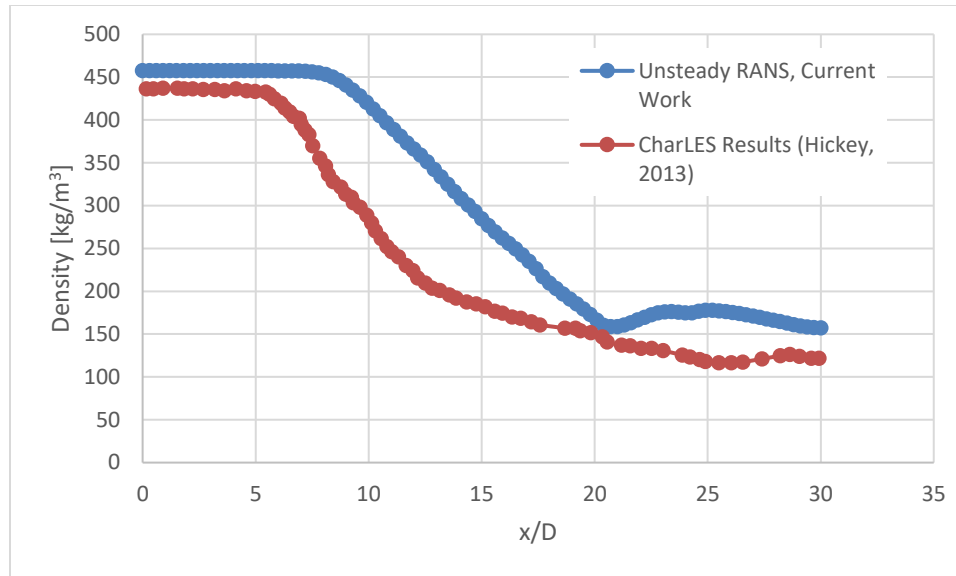


Figure 4.22 RANS Centerline Density Compared to CharLES Results

This is the best density decay agreement seen so far, although a slight overprediction of potential core penetration persists. Figure 4.23 shows centerline density experimental data and RANS model results for a similar but not identical case from (Branam, 2003), normalized with respect to density at jet exit. It is compared to current results.

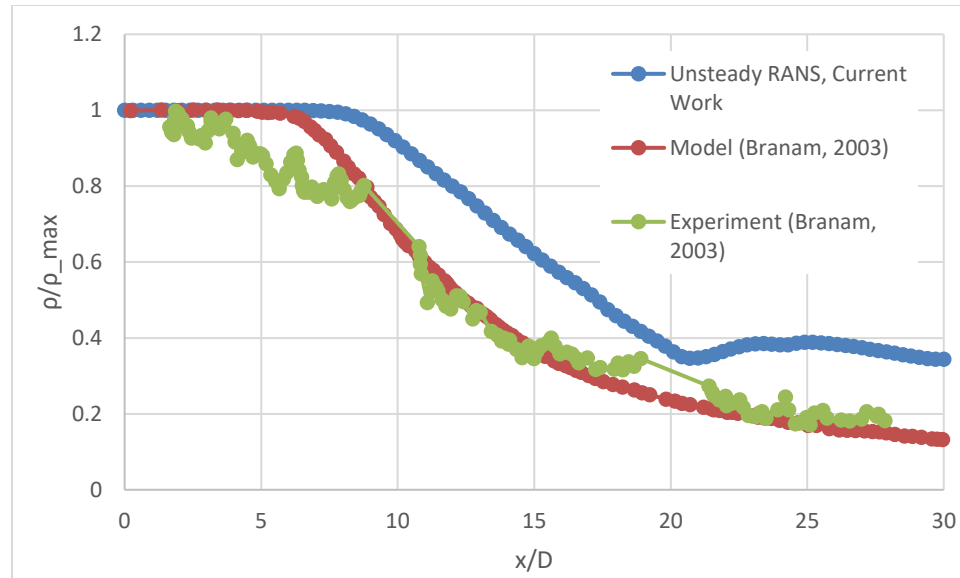


Figure 4.23 Centerline Density: Current Work Compared to Case 6 (3.9 MPa, 133 K, 5.4 m/s), (Branam, 2003)

Branam and Mayer find this is a short core penetration relative to their entire test matrix. They suggest this may be due to the heat transfer phenomenon characteristic to supercritical fluid; this case in particular features a jet injected above the temperature range for enhancement, and the jet needs to absorb less energy to achieve ambient temperature. The jet thus dissipates more smoothly, resulting in a shorter core. This case in particular speaks well of current modeling efforts, as the jet with which current work is compared is injected at a higher temperature, its temperature reaches the ambient condition more quickly, and density decays faster (6-7 jet diameters vs. the current 8-9). Core penetration is compared with overall experimental results in (Branam, 2003) as they plot this characteristic with respect to ratio of injected jet density to ambient density in Figure 4.24. Calculated density ratio of current work is approximately 10.07.

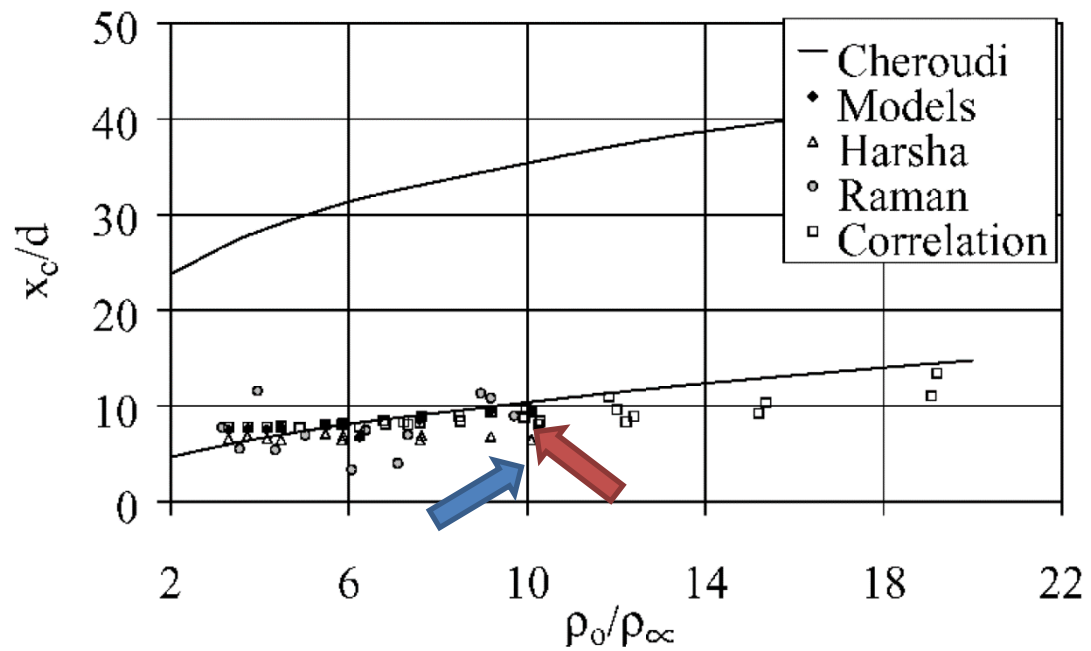


Figure 4.24 Potential Core Penetration vs. Density Ratio (Branam, 2003)

Current unsteady RANS results, suggesting a penetration of 8-9 jet diameters (indicated by the red arrow), agree well with the majority of data represented on this plot for an injected/ambient density ratio of 10. Current RANS results indicate an under-prediction of penetration, about 4 jet diameters, indicated by the blue arrow.

Axial velocity profiles normalized with respect to individual profile maximum velocities are presented in Figure 4.25.

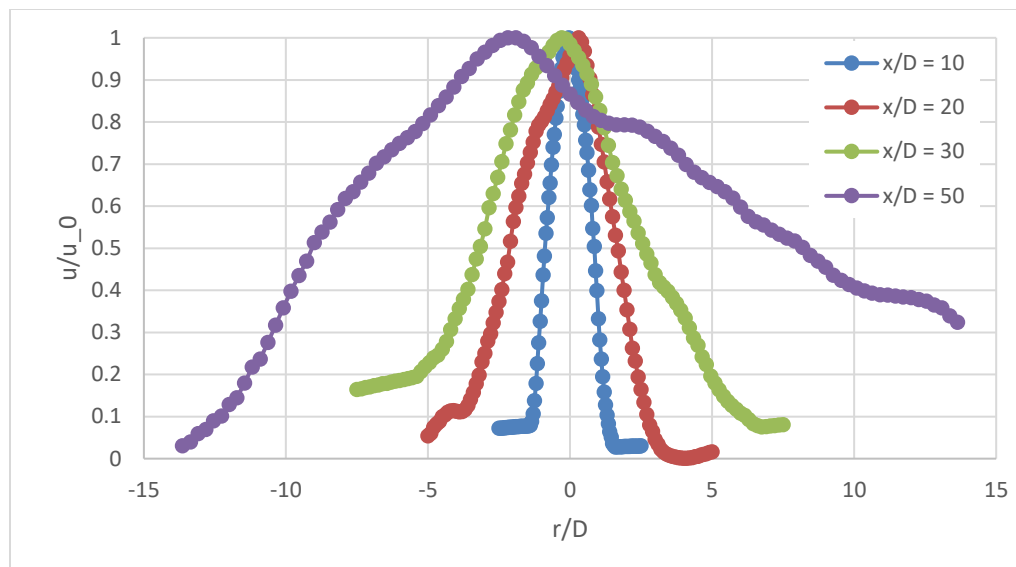


Figure 4.25 Axial Velocity Profiles, Unsteady RANS

Resulting jet half-width locations are presented in Figure 5.25.

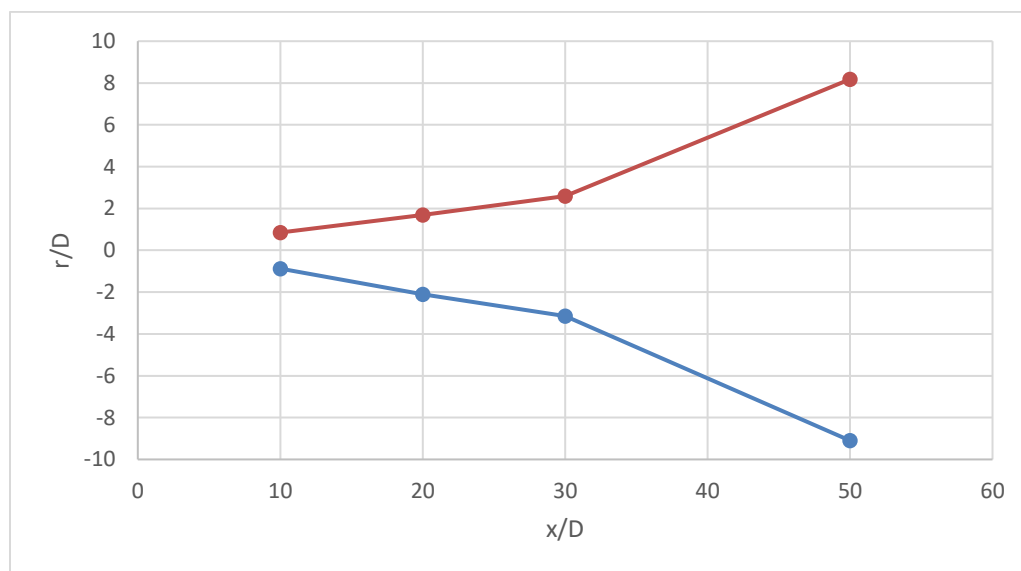


Figure 4.26 Jet Half-Width Locations, Unsteady RANS

The half-angle of jet divergence is calculated as $\alpha = \tan^{-1}\left(\frac{r/D}{x/D}\right)$ using axial velocity data for the first 30 jet diameters. The spreading angle (twice the half-angle) from current work is approximately 10.94° . This is compared to tabulated data from (Branam,

2003) in Figure 4.27.

Case	ρ_{∞}/ρ_0	50% u	50% T	50% ρ	99% u	99% T	99% ρ	Raman	Shadow
1	0.0658	9.2	11.6	6.2	11.2	15.3	11.9	—	8.4
2	0.0832	8.8	12.1	8.0	12.0	14.3	13.5	8.4	13.0
3	0.2046	9.4	9.6	7.4	12.6	13.1	12.8	10.8	10.9
4	0.0651	8.8	11.6	5.8	10.3	14.1	11.1	—	10.0
5	0.0845	8.2	9.5	5.2	11.1	11.4	10.6	6.9	14.8
6	0.2233	9.5	9.4	7.5	12.7	13.1	12.9	17.0	13.3
7	0.0818	9.2	10.9	5.9	11.9	13.8	11.7	—	11.8
8	0.1006	8.8	9.9	6.2	11.7	12.3	11.7	14.0	12.0
9	0.1364	9.0	9.6	7.0	12.1	12.7	12.3	12.5	11.6
10	0.0807	9.2	10.7	6.0	12.1	15.4	12.4	—	9.9
11	0.1003	8.6	9.5	5.9	11.3	11.4	10.9	9.1	13.5
12	0.1383	8.8	9.5	6.7	11.9	12.4	11.8	9.6	13.8
13	0.0975	9.8	11.1	6.9	12.5	16.2	13.2	—	11.9
14	0.1177	9.2	10.1	6.4	12.0	12.7	11.9	7.4	16.2
15	0.1467	9.2	9.7	6.8	12.3	12.8	12.2	6.2	12.7
16	0.0971	9.7	10.9	6.9	12.4	16.0	13.3	—	5.3
17	0.1180	9.1	9.9	6.3	12.0	12.4	11.8	7.0	16.5
18	0.1475	9.0	9.6	6.6	12.1	12.5	11.9	2.7	14.3

Figure 4.27 Tabular Jet Spreading Angle Data (Branam, 2003)

Case 5, to which we compare, shows a slightly lower density ratio, and a smaller calculated spreading angle with respect to axial velocity. The calculated angle from current work however falls evenly between Raman and shadowgraph technique measurements.

A density contour from current work is compared against a shadowgraph image from (Branam, 2002) for a similar case injected jet in Figure 4.28, and Figure 4.29.

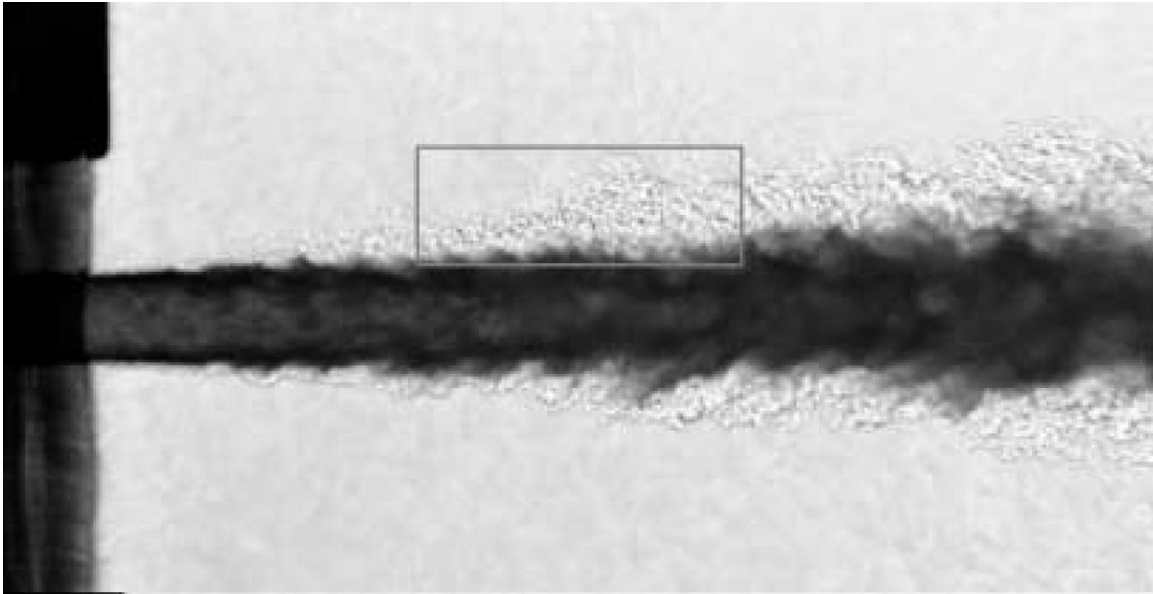


Figure 4.28 Shadowgraph Image: Case 3, 4 MPa, 4.9 m/s, 123 K Injected N₂ Jet (Branam, 2002)

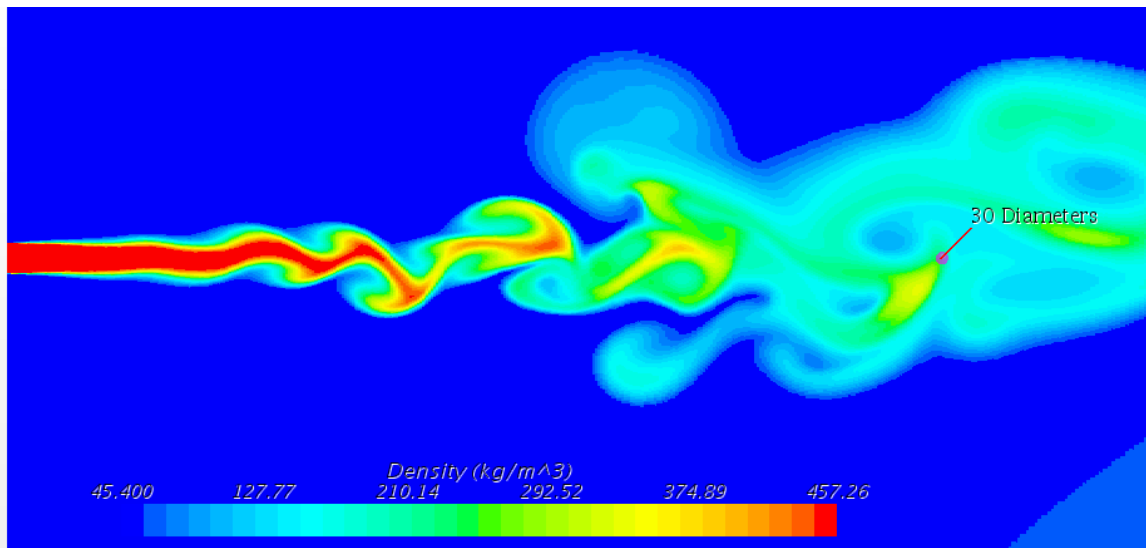


Figure 4.29 Density Contour (Snapshot) Unsteady RANS, Current Work

The current model shows a greater propensity for the jet to cast off large eddies asymmetrically, and does not capture the small, sub-millimeter scale density fluctuations of the experiment. This shadowgraph image, however, captures approximately only the first 13 jet diameters, and would be mostly composed of potential core. All contours

representing current work capture up to 30 jet diameters. A shadowgraph of the same flow case from Branam & Mayer's 2002 paper is presented overlaid with contours corresponding to measured streamwise turbulent length scales in Figure 4.30 and transverse length scales in Figure 4.31.

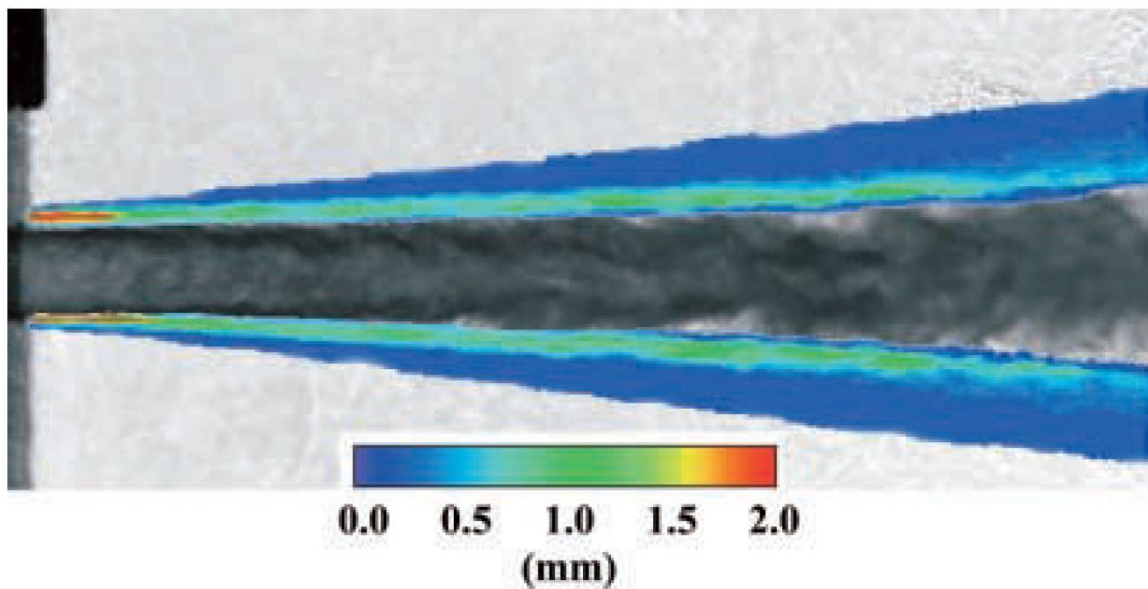


Figure 4.30 Streamwise Direction Turbulent Length Scales, Case 3 (Branam, 2002)

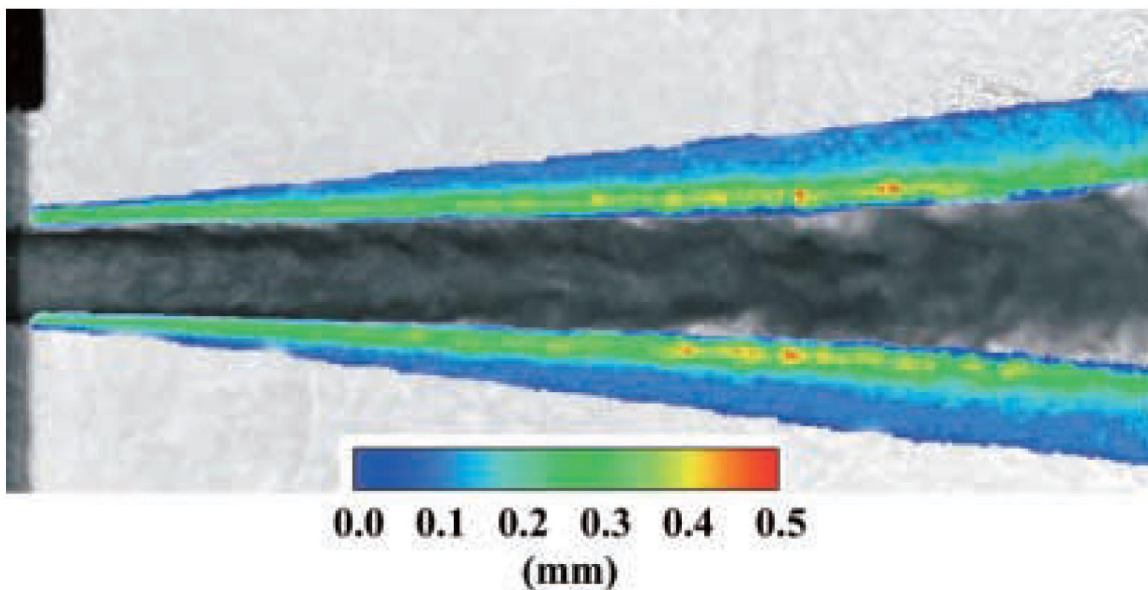


Figure 4.31 Transverse Direction Turbulent Length Scales, Case 3 (Branam, 2002)

The length scales observed in this 2002 experiment, as seen below, match well with calculated Taylor microscales, which are generally within one order of magnitude of jet exit diameter in this case. Turbulent length scales for current work are estimated based on model transport quantities. Integral, Taylor and Kolmogorov microscales are calculated according to equations 1-4, per (Branam, 2002).

$$L_{int} = \frac{k^{\frac{3}{2}}}{\varepsilon} \quad (1)$$

$$L_{Tay} = \left(\frac{15\nu\tilde{u}^2}{\varepsilon} \right)^{\frac{1}{2}} \quad (2)$$

Where,

$$\tilde{u} = \left(\frac{u^2 + v^2 + w^2}{3} \right)^{\frac{1}{2}} \quad (3)$$

$$L_{Kol} = \left(\frac{\nu^3}{\varepsilon} \right)^{\frac{1}{4}} \quad (4)$$

Using a k-omega model, the definition of specific turbulent dissipation is used and shown in equations 5 and 6:

$$\omega = \frac{\varepsilon}{k\beta^*} \quad (5)$$

$$\varepsilon = \omega k\beta^* \quad (6)$$

Where k is turbulent kinetic energy, ε is turbulent dissipation rate, ν is kinematic viscosity, u and v are velocities, ω is specific turbulence dissipation, and β^* is a k-omega turbulence model constant, usually 0.09, which is used in this case.

Estimated integral length scales are presented in Figure 4.32, Taylor microscales are presented in Figure 4.33, and Kolmogorov microscales are presented in Figure 4.34.

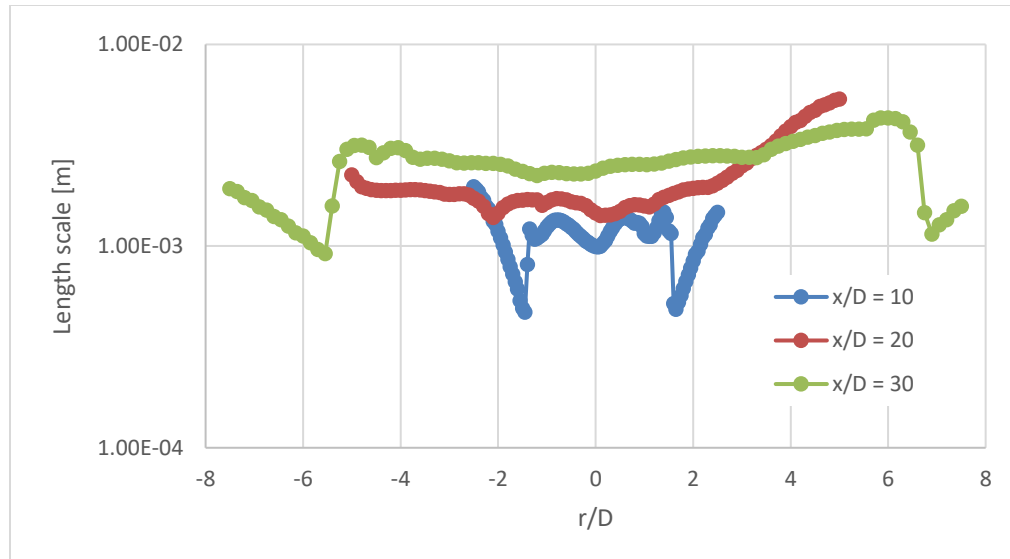


Figure 4.32 Integral Length Scales at Various x/D Locations, Unsteady RANS

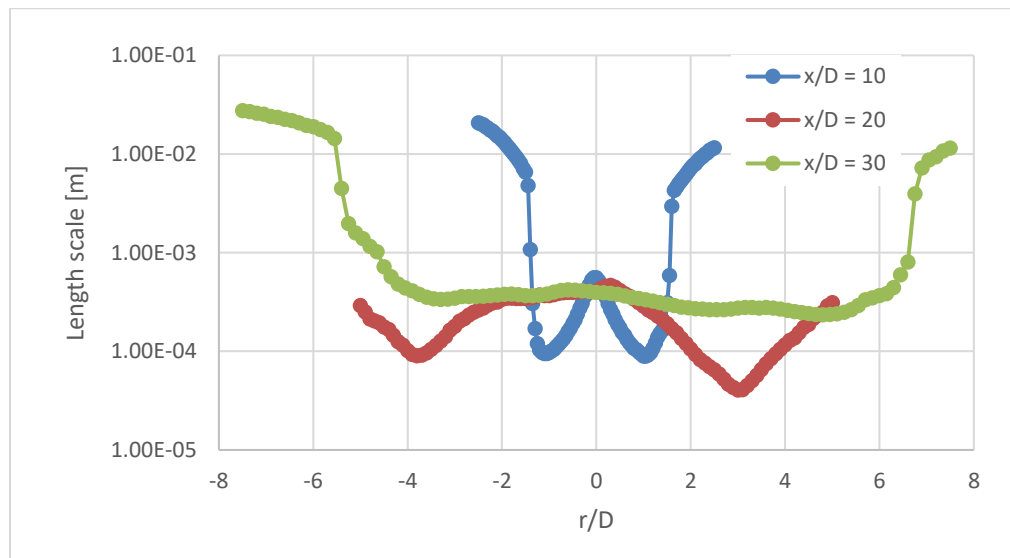


Figure 4.33 Taylor Microscales at Various x/D Locations, Unsteady RANS

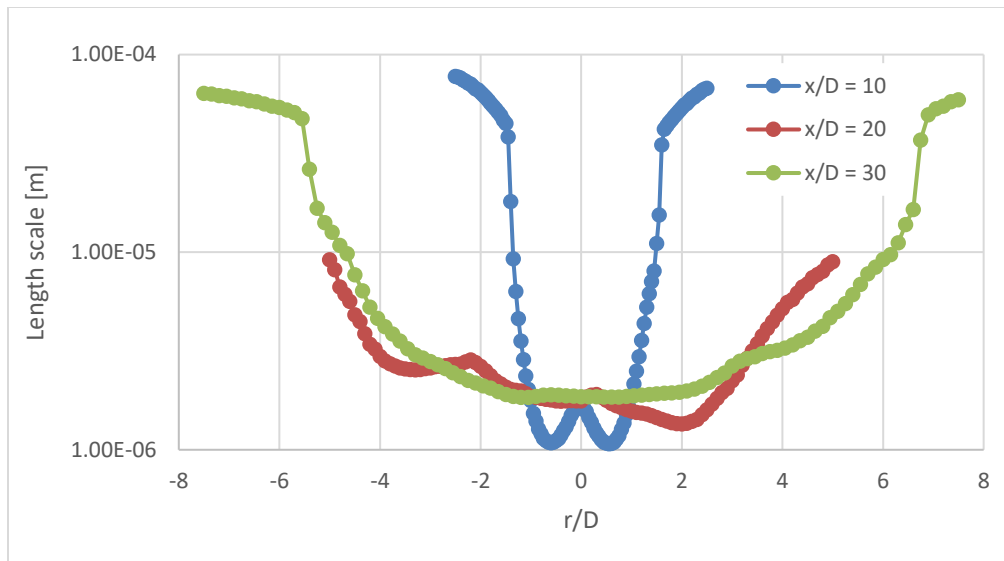


Figure 4.34 Kolmogorov Microscales at Various x/D Locations, Unsteady RANS

Length scales are compared to those calculated for Branam’s 2003 experiment, normalized with respect to jet diameter. Calculated length scales are compared in Figure 4.35.

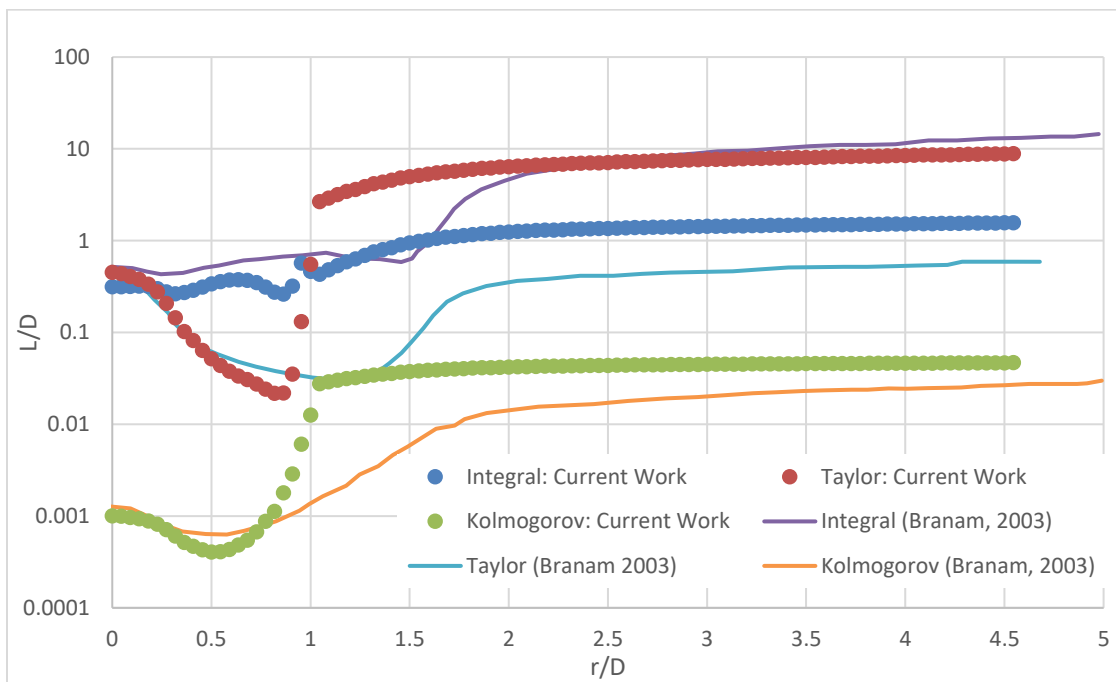


Figure 4.35 Calculated Turbulent Length Scales

There is a difference in magnitude between calculated values at this location between the two simulations, as the relative size of integral and Taylor microscales seem to reverse in current work. This can partially be attributed to Branam's use of a different commercial code with k-epsilon closure vs the current use of a k-omega closure. This also highlights the need for tuning of the turbulence model parameters of current work. Although the magnitude of these length scales differ, the trend is the same, and the Kolmogorov scale matches well. Other properties and settings of Branam's code are unknown at this time.

RANS Results: Comparison of Subcritical and Supercritical Results

Results from unsteady RANS modeling of a supercritical jet are here compared with single-phase gas jet mixing simulations run at subcritical pressures to demonstrate the ability of the current code to represent key differences (and similarities) in flow physics, and to highlight the importance of modeling real gas effects in the supercritical regime. Centerline density profiles are shown in figure Figure 4.36, normalized with respect to jet exit density.

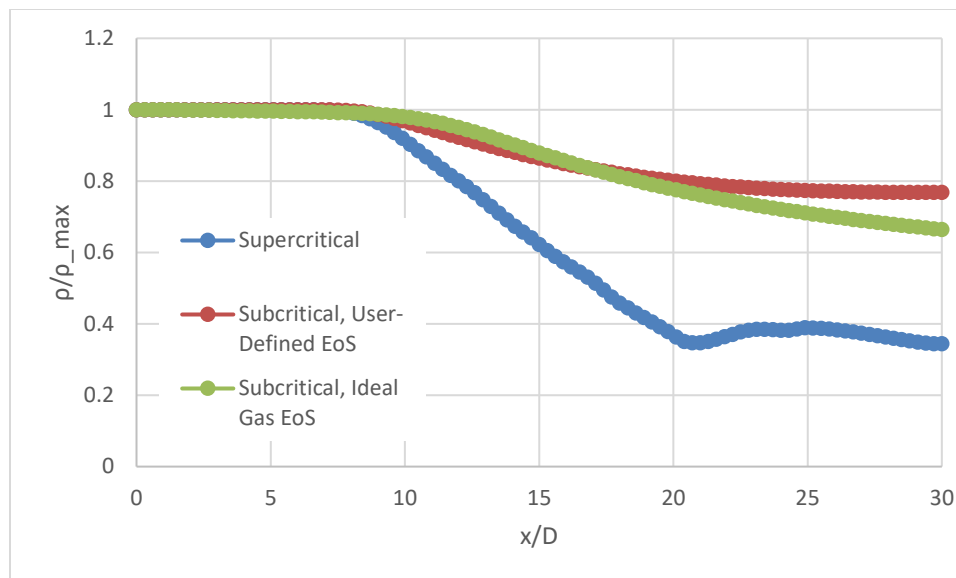


Figure 4.36 Normalized Centerline Density: Supercritical and two Subcritical Simulations, Unsteady RANS, Current Work

This figure serves to illustrate the effect of modeling real gas effects even at atmospheric conditions, as the subcritical case described above was run with ambient conditions of 298 K and 1 atm. The supercritical case has a shorter core penetration, and the density decay in the transition region is more aggressive, given the much stronger density gradient. Centerline axial velocity decay is compared for these cases in Figure 4.37.

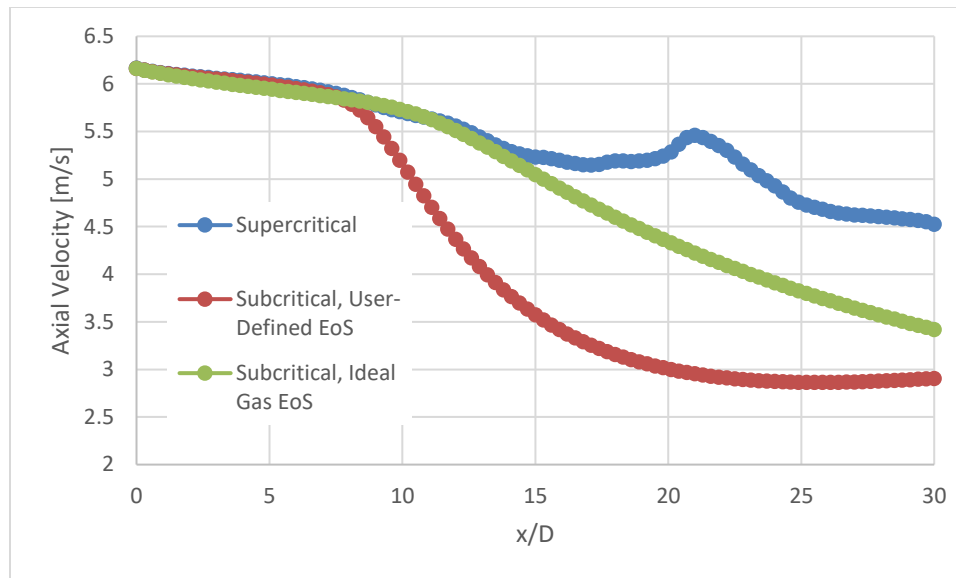


Figure 4.37 Centerline Axial Velocity: Supercritical and two Subcritical Simulations, Unsteady RANS, Current Work

Unsurprisingly, the supercritical case shows a slower decay of axial velocity at the centerline, as fluid speed is matched but density and therefore kinetic energy of the jet is much higher in that case. Interestingly, using real fluid properties has a large impact on the dissipation of energy from the jet, and this is likely due to variation in dynamic viscosity in the transverse direction, as this transport quantity is what will regulate the exchange of momentum across the shear layer of the jet. This difference is examined in Figure 4.38.

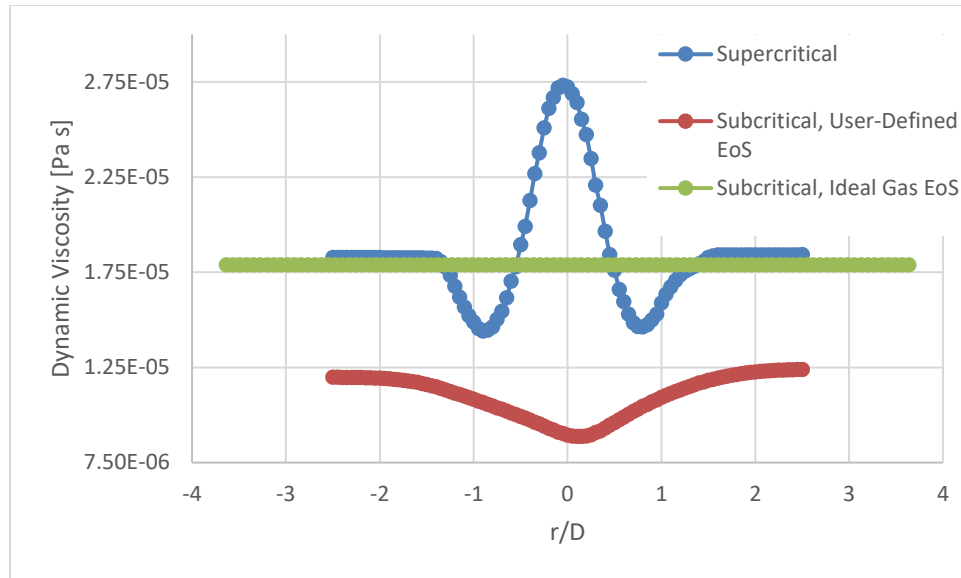


Figure 4.38 Dynamic Viscosity Profiles at $x/D = 10$: Supercritical and two Subcritical Simulations, Unsteady RANS, Current Work

This confirms the above assumption, with supercritical case viscosity being several times that of the real gas subcritical case. The assumption of constant fluid properties in the ideal gas case (specifically $\mu=1.79E-5$ Pa-s here) explains the similarity in velocity decay between this case and the supercritical case in Figure 4.37. Note in particular how the dynamic viscosity varies across the jet in the supercritical case (more than a factor of two) and the sharpness of the viscosity gradient in the transverse direction. There are similarly large gradients in specific heat, thermal conductivity and isentropic compressibility in the shear layer.

Final Thoughts

The STAR-CCM+ RANS simulations described above capture the expected single-phase gas jet mixing behavior expected in the literature. A strong tendency for asymmetric vortex shedding is observed, indicating why unsteady simulation is preferred. Additionally,

no atomization or droplet formation is produced. In a qualitative manner, a commercial code, when fed real gas properties, reproduces the proper flow physics. However, the results presented above indicate that the margin for error in specific measurements is high, and much further fine-tuning of the commercial code is required to match experimental data and previous numerical results. Although the accurate reproduction of supercritical mixing phenomena absolutely requires real fluid thermodynamic and transport properties, there is a computational cost associated with this, and in particular with the use of tabular data. Based on the work performed here on a parallel cluster, the use of tables introduces a 27.2% increase in CPU-hours compared with use of standard equations of state. It should be noted the majority of simulations were performed on a single cluster node, and this additional cost is not expected to scale linearly as cell counts grow and additional nodes are added.

Plots of simulation residuals and important monitor quantities can be found in the Appendix.

5. Conclusions and Recommendations

The commercial code STAR-CCM+ was demonstrated to reproduce the relevant flow physics when using imported tabular real fluid data. The author remains confident that a code such as this can be fine-tuned to more accurately represent mixing parameters such as density decay, axial velocity profiles and species concentrations in a multi-species flow. The code can then be applied to a cross-flow, and eventually inform a combustion model. The goal of this work remains design-oriented, and will apply to injectors in direct-fire s-CO₂ power cycles and liquid-propellant rockets. The following observations were made:

1. Of the model configurations examined, unsteady RANS simulation using k-omega SST turbulence closure provided the closest match of core penetration length to previous results. Still, there remains an over-prediction of potential core penetration of approximately 30% (Hickey, 2013).
2. There is a strong tendency in current unsteady RANS simulation for the jet to shed large vortices asymmetrically. This echoes previous assertions in the literature that turbulent mixing of a supercritical jet is an inherently unsteady phenomenon, and is why unsteady RANS simulation was necessary (Bellan, 2000).
3. Results from velocity magnitude and temperature contours of current unsteady RANS show a slower velocity decay and slower transition to ambient temperature than LES results in the literature (Hickey, 2013).
4. Small turbulent structures from LES in literature were not captured in current unsteady RANS simulation, despite grid refinement. This is due to Reynolds

averaging of the flow and modeling of small turbulent eddies as eddy viscosity. LES may be necessary to correctly predict penetration length, but further tuning of the turbulence model parameters could reproduce previous work at less computational expense. Current LES work needs model refinement but shows flow features of similar scale to previous work.

Future Work

The constant properties assumption inherent to the Reynolds decomposition is a necessary feature of all RANS simulation. This can, however, be mitigated by the future development of turbulence models custom to the supercritical regime (Bellan, 2000). Developing these models will likely require a certain amount of LES work, just as sub-grid scale models for LES required research using DNS (Miller, 2001). Additional work is also required in fine-tuning model and solver parameters to more closely capture the experimental data.

Having determined the suitability for commercial code to tackle supercritical mixing problems, important next steps toward the goals of improved injector design in liquid rockets and s-CO₂ cycles are:

1. Refine model constants and turbulent inlet conditions of unsteady RANS simulation to better match Case 5 from (Branam, 2003).
2. Introduce a passive scalar into unsteady RANS simulations to better quantify the mixing process. This is the numerical equivalent of injecting a dye into an experiment, and will identify the path of injected fluid as the jet evolves.
3. Create 3D unsteady RANS domain (quarter-jet) for comparison to experiment.
4. Complete grid independence study in LES model, refine time step for better

residual convergence.

5. Refine model constants and turbulent inlet conditions of LES model to better match Case 5 from (Branam, 2003) and CharLES results from (Hickey, 2013).
6. Compare unsteady RANS and LES results with the addition of a multispecies crossflow.
7. Compare unsteady RANS and LES results with a multispecies crossflow and co-axial injection of a fuel and oxidizer.

REFERENCES

About Us. Retrieved June 26, 2017 from <http://www.cascadetechnologies.com/about-us/>

Artham, S. K. (2016). An Experimental Study of Momentum-Driven Unsteady Jets.

Master of Science Thesis, Embry-Riddle Aeronautical University.

Barata, J., Gökalp, I., and Silva, A. (2003). Numerical Study of Cryogenic Jets Under Supercritical Conditions. *Journal of Propulsion and Power*, 19(1), 142-147.

Bellan, J. (2000). Supercritical (and subcritical) fluid behavior and modeling: drops, streams, shear and mixing layers, jets and sprays. *Progress in Energy and Combustion Science*, 26, 329-366.

Benedict, M., Webb, G. B., and Rubin, L. C. (1940). An Empirical Equation for Thermodynamic Properties of Light Hydrocarbons and Their Mixtures I. Methane, Ethane, Propane and n-Butane. *The Journal of Chemical Physics*, 8(334).

Birk, A., McQuaid, M., and Gross, M. (1995). Liquid Core Structure of Evaporating Sprays at High Pressures – Flash X-Ray Studies. Army Research Laboratory.

Boussinesq, J. (1877). *Essai sur la théorie des eaux courantes*. Paris, France : Imprimerie Nationale.

- Branam, R., and Mayer, W. (2002). Length scales in cryogenic injection at supercritical pressure. *Experiments in Fluids*, 33, 422-428.
- Branam, R., and Mayer, W. (2003). Characterization of Cryogenic Injection at Supercritical Pressure. *Journal of Propulsion and Power*, 19(3), 342-355.
- Brun, K., McClung, A., and Davis, J. (2014). Novel Supercritical Carbon Dioxide Power Cycle Utilizing Pressurized Oxy-combustion in Conjunction with Cryogenic Compression. Southwest Research Institute report.
- Chehroudi, B., Talley, D., and Coy, E. (1999). Initial Growth Rate and Visual Characteristics of a Round Jet into a Sub- to Supercritical Environment of Relevance to Rocket, Gas Turbine, and Diesel Engines. 37th AIAA Aerospace Sciences Meeting and Exhibit. 11-14 January, 1999, Reno, NV.
- Chen, Y.-S., and Kim, S.-W. (1987) Computation of turbulent flows using an extended k-epsilon turbulence model. NASA Technical Report, Marshall Space Flight Center, Huntsville, AL.
- Chung, T.-H., Lee, L. L., and Starling, K. E. (1984). Applications of Kinetic Gas Theories and Multiparameter Correlation for Prediction of Dilute Gas Viscosity and Thermal Conductivity. *Industrial & Engineering Chemistry Fundamentals*,

23(1), 8-13.

Cutrone, L., Ihme, M., and Herrmann, M. (2006). Modeling of high-pressure mixing and combustion in liquid rocket injectors. Proceedings of the Summer Program, Center for Turbulence Research, 2006, 269-281.

Ely, J. F., and Hanley, H. J. M. (1981). A Computer Program for the Prediction of Viscosity and Thermal Conductivity in Hydrocarbon Mixtures. National Bureau of Standards, Boulder, Colorado.

Fellouah, H., Ball, C. G., and Pollard, A. (2009). Reynolds number effects within the development region of a turbulent round free jet. International Journal of Heat and Mass Transfer, 52, 3943-3954.

Fu, H., et al. (2016). The Sunway TaihuLight supercomputer: system and applications. Science China Information Sciences, 59.

Fuller, E. N., Schettler, P. D., and Giddings, J. C. (1966). New method for prediction of binary gas-phase diffusion coefficients. Industrial & Engineering Chemistry, 58(5), 18-27.

Harstad, K. G., Miller, R. S., and Bellan, J. (1997). Efficient High-Pressure State Equations. American Institute of Chemical Engineers Journal, 43(6), 1605-1610.

- Hickey, J.-P., and Ihme, M. (2013). Supercritical mixing and combustion in rocket propulsion. Annual Research Briefs, Center for Turbulence Research, 21-36.
- Ivancic, B., Mayer, W., Krülle, G., and Brüggemann, D. (1999). Experimental and numerical investigation of time and length scales in LOX/GH2-Rocket combustors. 35th AIAA/ASME/SAE/ASEE Joint Propulsion Conference and Exhibit. June 20-23, 1999, Los Angeles, CA.
- Jacobsen, R. T., and Stewart, R. B. (1973). Thermodynamic Properties of Nitrogen Including Liquid and Vapor Phases from 63 K to 2000 K with Pressures to 10,000 Bar. The Journal of Physical and Chemical Reference Data, 2(4), 757-922.
- Kim, T., Kim, Y., Kim, S.-Y. (2011). Numerical study of cryogenic liquid nitrogen jets at supercritical pressures. The Journal of Supercritical Fluids, 56, 152-163.
- Lemmon, E.W., Huber, M.L., McLinden, M.O. NIST Standard Reference Database 23: Reference Fluid Thermodynamic and Transport Properties-REFPROP, Version 9.1, National Institute of Standards and Technology, Standard Reference Data Program, Gaithersburg, 2013.
- Lewis, T., and Rochau, G. E. (2012). Developments with Sandia's Supercritical Carbon Dioxide Brayton Cycle and Advance Energy Technologies. 2012 Power Sources

Conference, June 11-14, 2012.

Menter, F. R. (1994). Two-Equation Eddy-Viscosity Turbulence Models for Engineering Applications. *AIAA Journal*, 32 (8), 1598-1605.

Miller, R. S., Harstad, K. G., and Bellan, J. (2001). Direct numerical simulations of supercritical fluid mixing layers applied to heptane-nitrogen. *Journal of Fluid Mechanics*, 436, 1-39.

Milone, D. V. (2009). Computational Model and Experimental Data on the Natural Circulation of Supercritical Carbon Dioxide. *Proceedings of S-CO₂ Power Cycle Symposium 2009*. April 29-30, 2009, Troy, NY.

Nicoud, F., and Ducros, F. (1999). Subgrid-Scale Stress Modeling Based on the Square of the Velocity Gradient Tensor. *Flow, Turbulence and Combustion*, 62, 183-200.

Oefelein, J. C., and Yang, V. (1998). Modeling High-Pressure Mixing and Combustion Processes in Liquid Rocket Engines. *Journal of Propulsion and Power*, 14(5), 843-857.

Peng, D.-Y., and Robinson, D. B. (1975). A New Two-Constant Equation of State. *Industrial & Engineering Chemistry Fundamentals*, 15(1), 59-64.

Polikhov, S., and Segal, C. (2007). Experimental Study of Subcritical to Supercritical Jet Mixing. 45th AIAA Aerospace Sciences Meeting and Exhibit. 8-11 January 2007, Reno, Nevada.

Pointwise, Inc., Pre-Processing and Computational Grid Generation Application, Pointwise, [Computer Software], Ver. 17.5 Release 5, Fort Worth, TX. Retrieved July 19, 2016.

Pope, S. (2000). Turbulent Flows (1st ed.) Cambridge, United Kingdom: Cambridge University Press.

Reynolds, O. (1895). On the Dynamical Theory of Incompressible Viscous Fluids and the Determination of the Criterion. Philosophical Transactions of the Royal Society of London, 186, 123-164.

Roy, A., and Segal, C. (2010). Experimental Study of Fluid Jet Mixing at Supercritical Conditions. Journal of Propulsion and Power, 26(6), 1205-1211.

Siemens AG Product Management. Spotlight On... Turbulence. Retrieved July 2, 2017, from https://thesteveportal.plm.automation.siemens.com/articles/en_US/FAQ/Spotlight-on-Turbulence

Siemens Product Lifecycle Management Software Inc. (n.d.). The Steve Portal. Retrieved July 2, 2017, from <https://thesteveportal.plm.automation.siemens.com>.

Siemens Product Lifecycle Management Software Inc. (n.d.). STAR-CCM+ User Guide. Retrieved June 13, 2017, from https://stevedocs.cd-adapco.com/starccmplus_latest_en/.

Siemens Product Lifecycle Management Software Inc., Computational Dynamics Analysis & Design Application, STAR-CCM+, [Computer Software], Ver. 10.06.010, Orlando, FL. Retrieved April 11, 2017.

Siemens Product Lifecycle Management Software Inc., Computational Dynamics Analysis & Design Application, STAR-CCM+, [Computer Software], Ver. 12.02.011, Orlando FL. Retrieved April 17, 2017.

Strutt, J. W. (1879). On the instability of jets. Proceedings of the London Mathematical Society, 4-13.

Suo-Anttila, A., and Wright, S. (2011). Computational Fluid Dynamics Code for Supercritical Fluids. SCO2 Power Cycle Symposium. May 24-25, 2011, Boulder, Colorado.

- Takahashi, S. (1974). Preparation of a generalized chart for the diffusion coefficients of gases at high pressures. *Journal Of Chemical Engineering Of Japan*, 7(6), 417-420.
- The Mathworks, Inc., Mathematics Application, MATLAB, [Computer Software], Ver. R2016b (9.1.0.441655), Natick, MA. Retrieved September 7, 2016.
- Thermophysical Properties of Fluid Systems. National Institute of Standards and Technology. Retrieved July 2, 2017 from <http://webbook.nist.gov/chemistry/fluid/>.
- Tuoc, T. K. (2009). A theory of turbulence. Part 1: Towards solutions of the Navier-Stokes equations. Retrieved July 4, 2017 from https://www.researchgate.net/publication/45877717_A_theory_of_turbulence_Part_1Towards_solutions_of_the_Navier-stokes_equations.
- Turkel, E. (1987). Preconditioned Methods for Solving the Incompressible and Low Speed Compressible Equations. *Journal of Computational Physics*, 72, 277-298.
- Vreman, A. W. (2004). An eddy-viscosity subgrid-scale model for turbulent shear flow: Algebraic theory and applications. *Physics of Fluids*, 16(10), 3670-3681.
- Weiss, J. M., and Smith, W. A. (1995). Preconditioning Applied to Variable and Constant

Density Flows. *AIAA Journal*, 33(11), 2050-2057.

Wu, P.-K., Shahnam, M., Kirkendall, K., Carter, C., and Nejad, A. (1999). Expansion and Mixing Processes of Underexpanded Supercritical Fuel Jets Injected into Superheated Conditions. *Journal of Propulsion and Power*, 15(5), 642-649.

Yang, V. (2000). Modeling of supercritical vaporization, mixing, and combustion processes in liquid-fuelled propulsion systems. *Proceedings of the Combustion Institute*, 28, 925-942.

Yoonhan, A., Seong, J. B., et al. (2015). Review of supercritical CO₂ power cycle technology and current status of research and development. *Nuclear Engineering And Technology*, 47, 647-661.

Zong, N., Meng, H., Hsieh, S.-Y., and Yang, Y. (2004). A numerical study of cryogenic fluid injection and mixing under supercritical conditions. *Physics of Fluids*, 16(12), 4248-4261.

A. Model Convergence Data

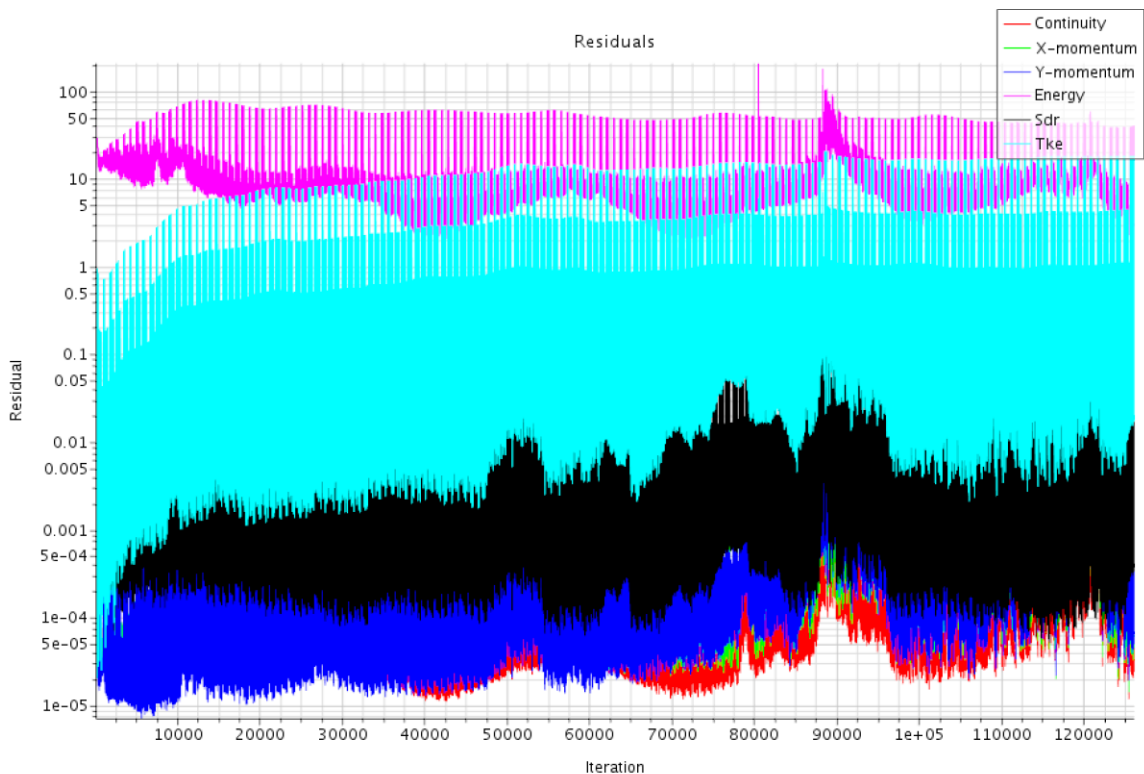


Figure 5.1 Residuals, Unsteady RANS, Supercritical

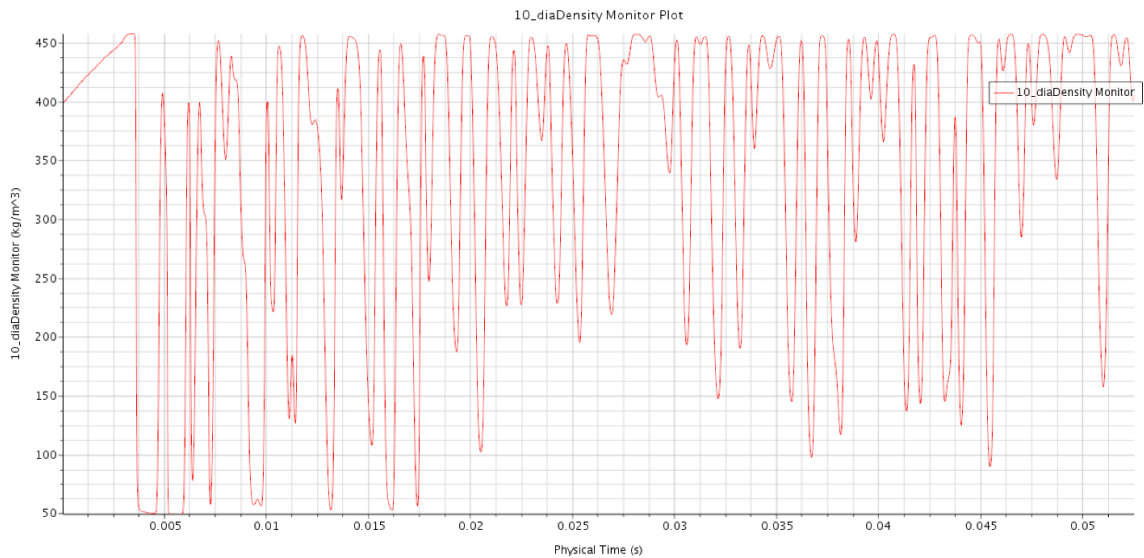


Figure 5.2 Monitor of Density at $x/D = 10$, Unsteady RANS, Supercritical

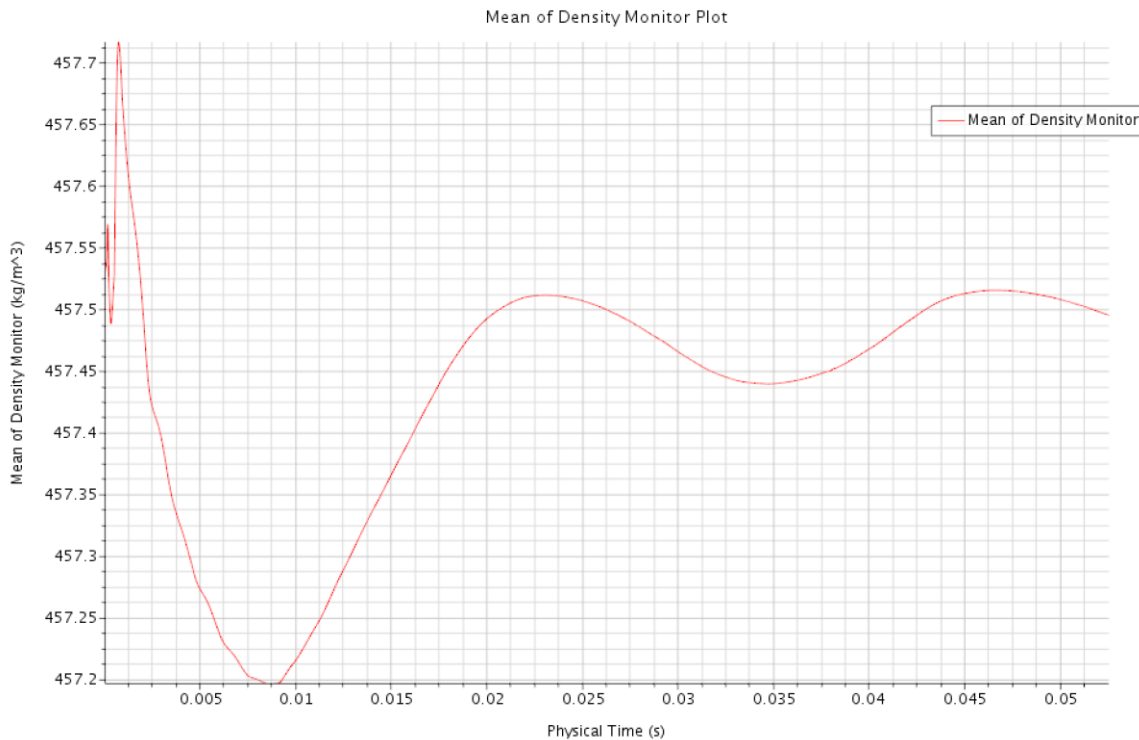


Figure 5.3 Monitor of Surface Average Density, Unsteady RANS, Supercritical

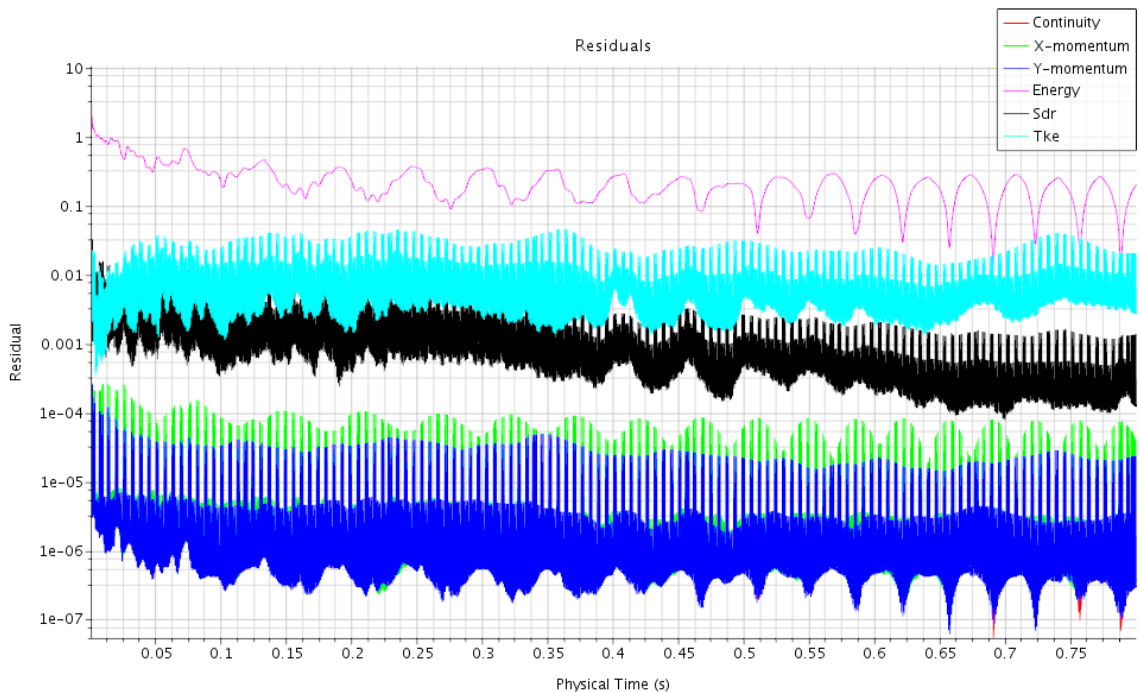


Figure 5.4 Residuals, Unsteady RANS, Subcritical

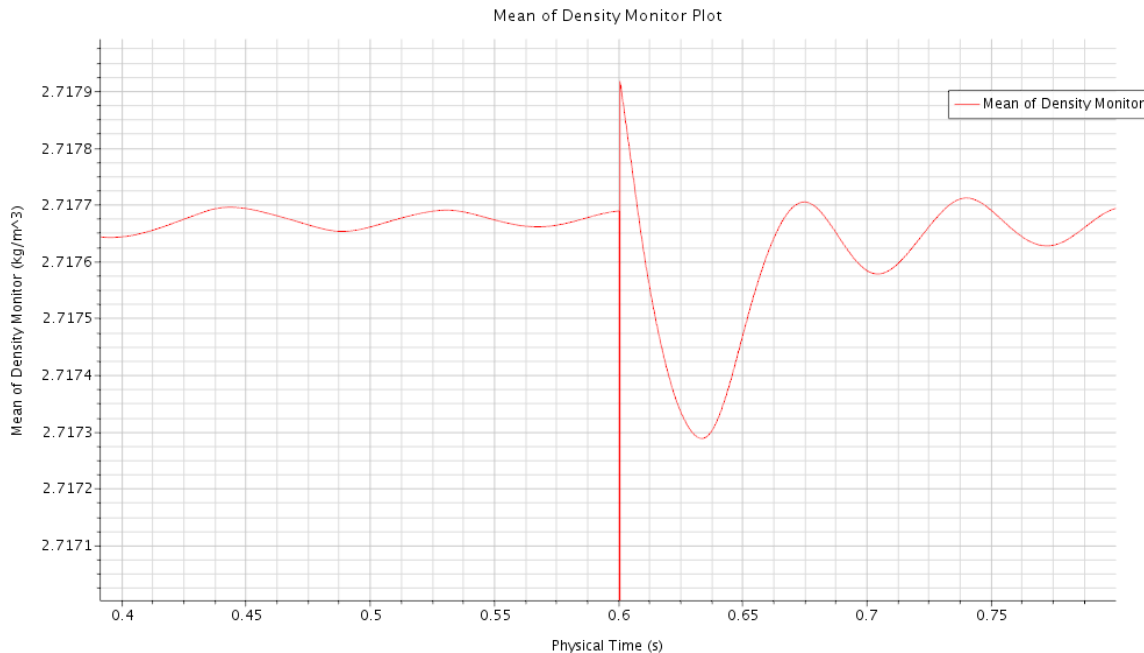


Figure 5.5 Surface Average of Density, Unsteady RANS, Subcritical

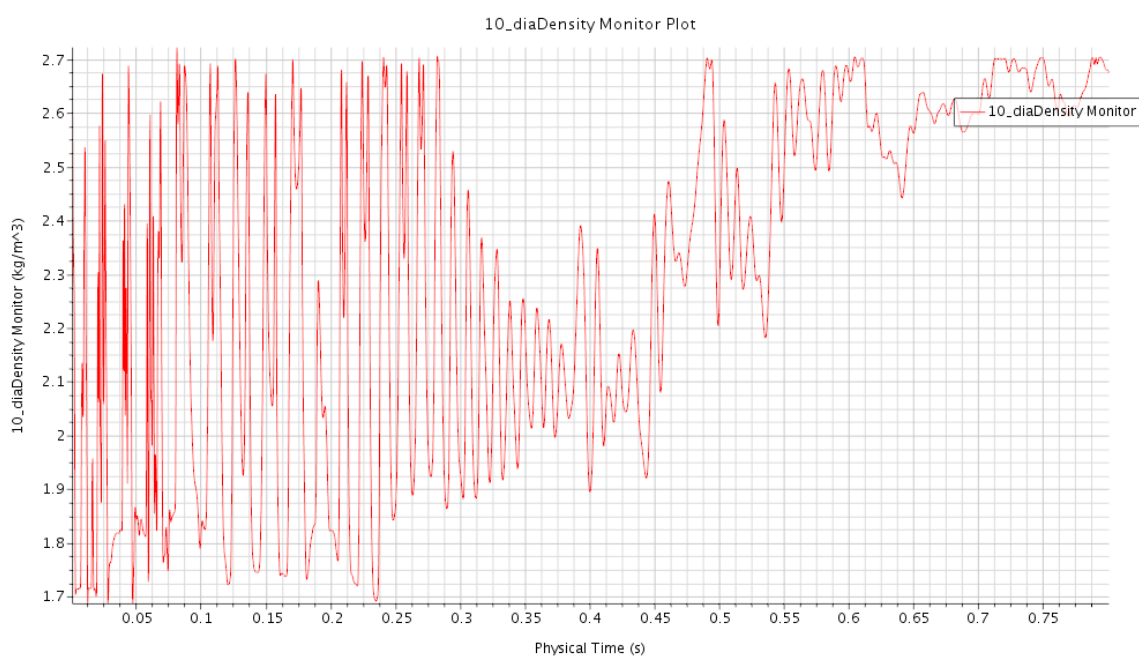


Figure 5.6 Monitor of Density at 10 Jet Diameters, Unsteady RANS, Subcritical

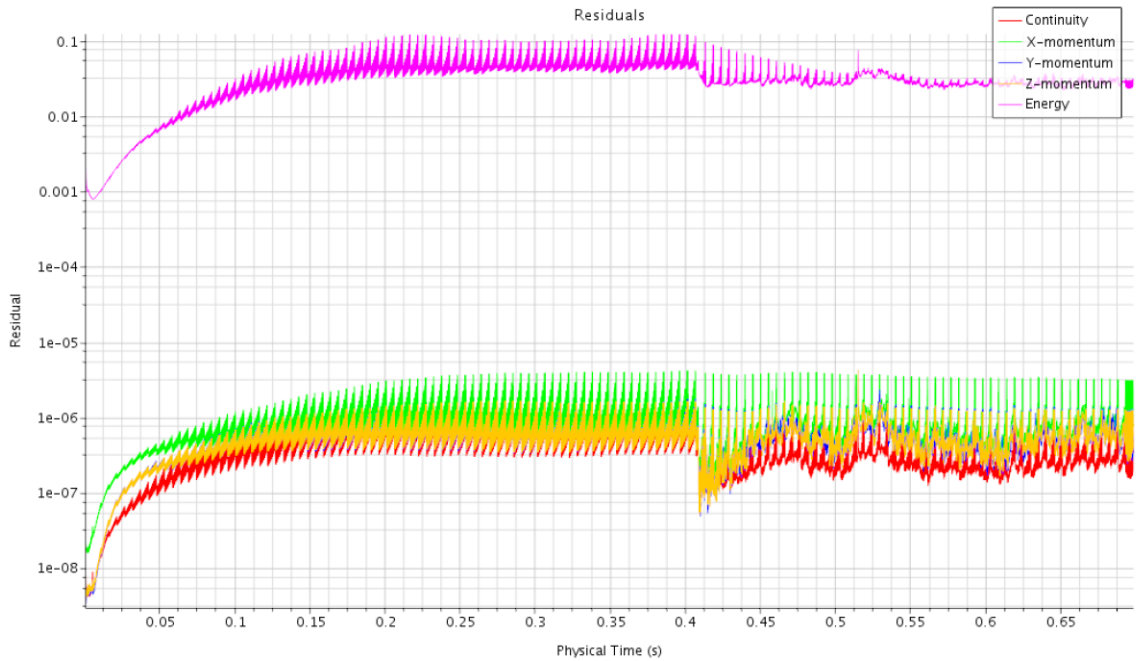


Figure 5.7 Residuals, LES

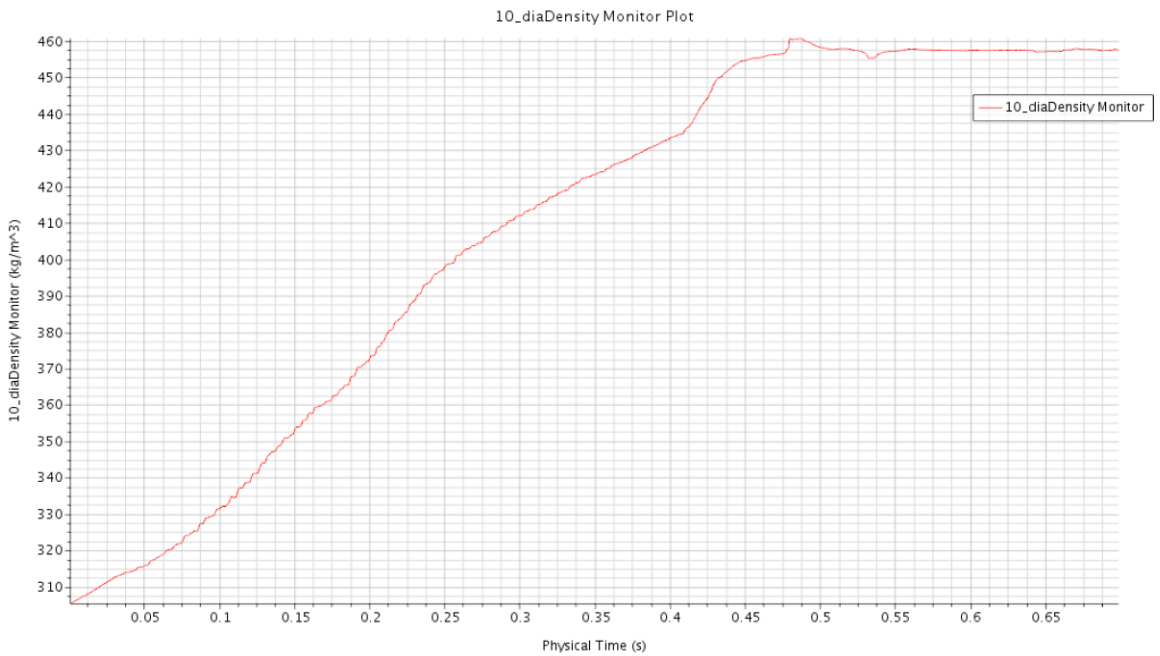


Figure 5.8 Monitor of Density at $x/D = 10$, LES

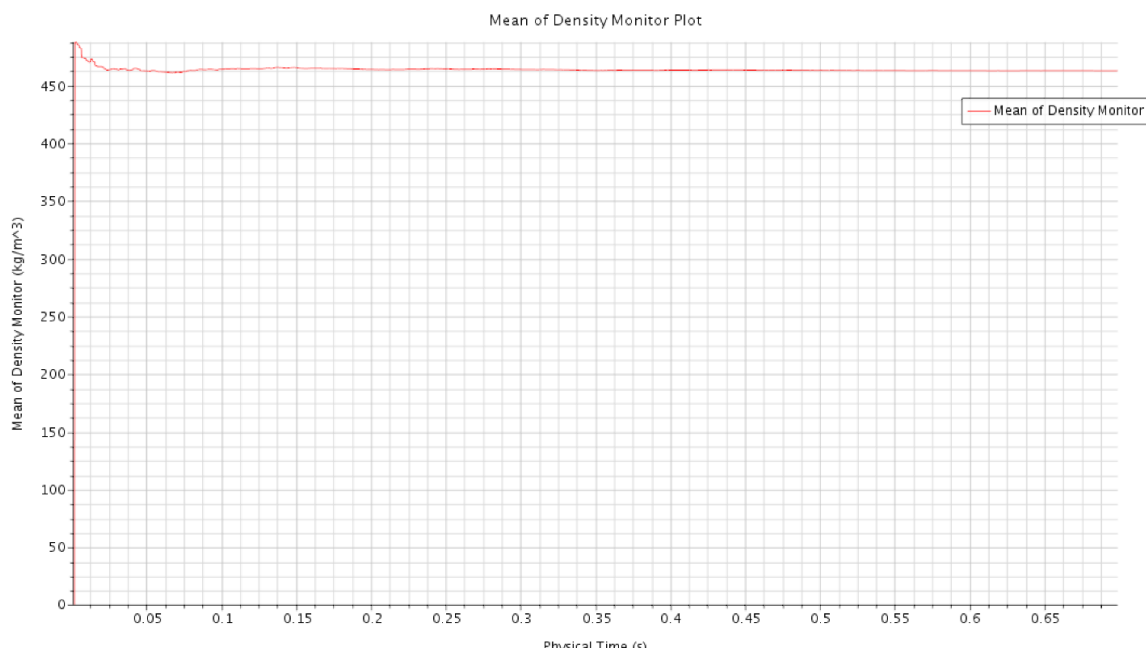


Figure 5.9 Monitor of Surface Average Density, LES